University of Crete
Department of Material Science and Technology

EXPERIMENTAL AND THEORETICAL STUDIES OF LEFT-HANDED METAMATERIALS

By
Tamara Funda Gundogdu

A dissertation submitted to the University of Crete
in partial fulfillment of the requirements for the degree of
Doctor of Philosophy
in Materials Science and Technology

Heraklion, 2009

To my mother, Guler Gundogdu

Table of Contents

List of Figures

Chapter 1

Introduction

Electromagnetic wave phenomena have always attracted a great attention. There are countless applications like imaging, communication, data storage, sensing, and devices like antennas, lenses, optical fibers, lasers, light sources which are based on electromagnetic waves and their interactions with matter. The subject of wave and matter interaction includes many effects like transmission, reflection, diffraction and refraction. The response of isotropic and homogeneous materials to an incident wave changes drastically, depending on two electromagnetic parameters, namely the electrical permittivity (ε) and the magnetic permeability (μ). In natural bulk materials, the values that ε and μ can take are limited. For the majority of the materials, the value of μ is 1 and it can not be negative.

However in 1968 Veselago [1] predicted that the existence of negative ε and μ values do not violate the Maxwell's equations and simultaneously negative ε and μ result in wave propagation. In 1999, nearly three decades after Veselago's work, Sir John Pendry published theoretical studies [2-4] that explain how one could create such a material artificially. The possibility of negative permeability and permittivity lead the way to exciting prospective applications such as a perfect lens with subwavelength resolution, or

miniaturization of EM devices. Soon, scientists and engineers started working on the possible designs to realize Pendry's predictions all over the world [5]. The first composite metamaterial that has the unique property of having both negative ε and μ is demonstrated by Smith et al. in 2000 [6, 7]. Since then, such metamaterials have been called as left-handed materials or negative index materials, and the interest in metamaterial research has grown rapidly [8-15]. After the first demonstrations of left-handed materials in microwave frequencies, scientists focused their efforts on designing new composite metamaterials operating in yet higher frequency regimes [16-25] with the ultimate goal of realizing photonic applications.

In this thesis, first, composite metamaterials and left-handed behaviour in composite metamaterials are investigated in microwave frequencies. Then our investigations are focused on the metamaterials operating in the far infrared frequencies. The outline of this thesis can be summarized as follows;

In Chapter 2, a theoretical background of left-handed metamaterials is presented. Starting with the Maxwell's equations, negative index materials, backward wave propagation, negative refraction at the interface between left-handed and regular media and other basic aspects are described. Artificial building blocks such as the split-ring resonators (SRRs), continuous wires, and slab-pairs and their general response is discussed. Finally, a short historical review of left-handed material research is included.

In Chapter 3, composite metamaterials consisting of SRRs and continuous wires operating at microwave frequencies are presented. At the same time, the term left-handed behaviour and the criteria that determine this behaviour are discussed in detail with specific examples of composite metamaterials operating at microwave frequencies. Moreover, studies regarding a comparison of in-plane and off-plane SRR-wire placement, and electrical excitation of magnetic resonance (EEMR) effect are included. Finally, the effect of SRRs on electric (not magnetic) resonance of the composite structure is investigated and it was found that this effect has significant consequences regarding the design for LH behaviour.

In Chapter 4, numerical studies of left-handed materials based on the split ring resonator (SRR) element are presented. Microwave Studio (MWS) code is used as a simulation tool as well as a retrieval procedure for the calculation of effective ε and μ parameters. The effect of the geometry of the SRR on its negative permeability response is investigated extensively. In addition, a detailed study of the dependence of the LH transmission on various other geometrical and material parameters of the system is examined.

In Chapter 5, the composite metamaterials operating in the far infrared frequency region are investigated. Different designs operating at THz frequencies are presented. First, the SRR and multi-gap SRR designs are introduced. The microfabrication process for the fabrication of those designs and the transmission and reflection measurements performed by using Fourier transform infrared spectroscopy (FTIR) are discussed in detail. Then, the slab pair- continuous wire design is presented and the FTIR measurements of these samples are presented and discussed.

In Chapter 6, we present our studies on switchable SRR structures created by incorporating proper photoconductive material in ordinary SRRs. We study various configurations of the photoconductive material and their effects on the switching properties of the SRRs by simulating the effect of conductivity variation. Three different configurations that are applicable under certain fabrication and/or optical excitation conditions are described and investigated.

Chapter 2

Left-handed Metamaterials

In 1968 Victor Veselago first stated that materials with combined negative permittivity and permeability exhibit negative index of refraction and these materials with negative refractive indices can alter the propagation of electromagnetic waves in counterintuitive and contrasting fashion to that observed and expected in ordinary materials [1]. For almost three decades, the idea remained as a scientifically curious observation until Sir John B. Pendry's pioneering proposals for achieving negative permeability [2-4]. With the advent of engineered materials exhibiting negative permeability, the original idea of Veselago opened up the rapidly grown new field called left-handed metamaterials today.

2.1 Left-handed Materials

The term "left-handed material" (LHM) was first used by Veselago [1] in 1968. In his work, Veselago predicted and discussed a theoretical medium where both permittivity and permeability are negative. In this medium the electric field $\boldsymbol{E}$, the magnetic field $\boldsymbol{H}$, and the wave vector $\boldsymbol{k}$, form a left-handed orthogonal set of vectors (that is why the tern

left-handed), and the real part of the index of refraction will be negative. The term, "negative index material (NIM)" is therefore, used equivalently and interchangeably with LHM.

Below, we describe such a material similar to Veselago's theory.

In order to investigate the electromagnetic (EM) properties of a LHM, we first describe the EM wave behaviour when ε and μ are both negative. For an isotropic medium, the source-free Maxwell's equations and the constitutive relations can be written as:

$$\begin{aligned} \nabla \times \boldsymbol{E} &= -\frac{\partial \boldsymbol{B}}{\partial t} \\ \nabla \times \boldsymbol{H} &= \frac{\partial \boldsymbol{D}}{\partial t} \end{aligned} \tag{2.1}$$

and

$$\begin{aligned} \boldsymbol{B} &= \mu \boldsymbol{H} \\ \boldsymbol{D} &= \varepsilon \boldsymbol{E}. \end{aligned} \tag{2.2}$$

In the case of plane wave solutions where all fields are proportional to $e^{i(\boldsymbol{k}z-\omega t)}$, the Eqns. 2.1 reduce to:

$$\begin{aligned} \boldsymbol{k} \times \boldsymbol{E} &= \omega \mu \boldsymbol{H} \\ \boldsymbol{k} \times \boldsymbol{H} &= -\omega \varepsilon \boldsymbol{E}. \end{aligned} \tag{2.3}$$

It can be observed from Eqns. 2.3 that $\boldsymbol{E}$, $\boldsymbol{H}$ and $\boldsymbol{k}$ form a left-handed orthogonal set of vectors when ε and μ are both negative.

The direction of the energy flow, on the other hand, is given by the Poynting vector:

$$\boldsymbol{S} = \boldsymbol{E} \times \boldsymbol{H}. \tag{2.4}$$

The Poynting vector, when not equal to zero, forms a right-handed set of vectors with $\boldsymbol{E}$ and $\boldsymbol{H}$, independent of the signs of ε and μ. Therefore, the directions of the energy density flow, $\boldsymbol{S}$, and the wave vector, $\boldsymbol{k}$, are opposite in a LHM. In contrast, in a regular right-handed material (RHM), $\boldsymbol{S}$ and $\boldsymbol{k}$ are in the same direction and such a wave is called a "forward wave". Similarly, the EM wave in a LHM, where $\boldsymbol{S}$ and $\boldsymbol{k}$ have opposite

directions is called a “backward wave”. The directions of ***E, H, k*** and ***S*** are shown in Fig. 2.1 for both RHM and LHM.

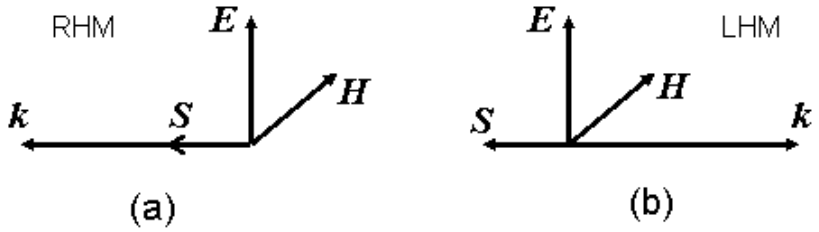

Figure 2.1: (a) RHM, where *E*, *H* and *k* form a right-handed system, and the direction of *k* and *S* is the same. (b) LHM, where *E*, *H* and *k* form a left-handed system, and the directions of *k* and *S* are opposite.

In a lossless, isotropic and homogeneous medium, where ε and μ are real numbers, a wave either propagates or decays depending on the signs of ε and μ. The dispersion relation in such a medium is given by:

$$k^2 = \omega^2 \varepsilon \mu. \tag{2.5}$$

When ε and μ are either both positive or both negative, $k = \omega\sqrt{\varepsilon\mu}$ is real, and the wave propagates; however when one of ε and μ is positive and the other one is negative, $k = i\omega\sqrt{|\varepsilon\mu|}$ is imaginary, and the wave decays exponentially. Wave propagation, in relation to the signs of ε and μ can be illustrated as in Figure 2.2. In the figure, a hypothetical ε - μ coordinate system is depicted as divided into four quadrants. All dielectrics, for example, would fall into the first quadrant in the context of Fig. 2.2, since they have ε and μ both positive. Similarly, substances with only ε negative exist in nature. For example, plasma media, such as ionized gas or free electron gas in metal, which have negative ε up until the plasma frequency belong to the second quadrant. Materials that have negative permeability such as ferromagnets and antiferromagnets belong to the fourth quadrant. Left-handed materials, on the other hand, do not exist naturally. In the last decade, theoretical and experimental work towards the realization of LHMs was concentrated in establishing artificially μ-negative and ε-negative media separately and combining these together to form composite structures that have both ε and μ negative over a certain spectral range. The pioneering designs of Sir John Pendry were first

realized experimentally in the microwave region of EM spectrum and over the years, the demonstrated working region of LHM design was advanced towards the optical frequencies.

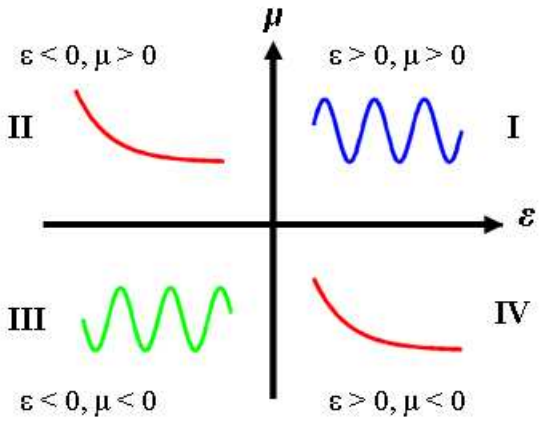

Figure 2.2: Forward EM waves propagate in the first quadrant of the ε - μ coordinate system, whereas backward EM waves propagate in the third quadrant. In the second and fourth quadrants waves decay exponentially.

2.2 Demonstration of Left-handed Materials

As discussed above, LHMs were theoretically proposed almost forty years ago. However, their realization was delayed due to the inexistence of a naturally occurring negative permeability material until only after Sir J.B. Pendry proposed the split-ring resonator (SRR) array design to provide $\mu < 0$ in the vicinity of a magnetic resonance at a frequency ω_m .The SRR element acts like a LC circuit when a magnetic field component is perpendicular to the SRR plane. Due to the resonant circular currents in the rings it exhibits a resonance at $\omega_m = 1/\sqrt{LC}$ which leads to a negative magnetic permeability (μ) response. In the following sections, SRRs and their magnetic response, as well as the

continous wire medium, the companion that completes the negative μ response with the negative ε response for the negative refractive index, will be discussed.

2.2.1 Negative Permittivity ($\varepsilon < 0$)

Negative permittivity materials exist in nature. Plasma is a medium with an equal concentration of positive and negative charges, where at least one type of charge carrier is mobile. All plasma media, including all the metals have negative permittivity below the plasma frequency. The permittivity of a metal can be described by the Drude model [26]:

.

$$\varepsilon(\omega) = 1 - \frac{\omega_p^2}{\omega(\omega + i\omega_c)}, \tag{2.6}$$

where ω_p and ω_c are the plasma and damping frequencies, respectively. The plasma frequency is given by:

$$\omega_p^2 = \frac{ne^2}{\varepsilon_0 m_e}, \tag{2.7}$$

where n and m_e are the number density and effective mass of free electrons, respectively. The significant point about Eqn. 2.6 is that the $\varepsilon(\omega)$ is negative below the plasma frequency, and as a consequence, only evanescent modes (imaginary wave vector) exist and radiation cannot penetrate far into the metal below the plasma frequency [27]. For bulk metals, the ω_p/ω_c ratio is very high ($\omega_p/\omega_c \approx 150$ for Al, and $\omega_p/\omega_c \approx 500$ for Ag) and the plasma frequency is at the ultraviolet (UV) region of the electromagnetic spectrum. Far below the UV, the absolute value of the negative permittivity is very high and metal is inpenetrable because of the large impedance mismatch. Pendry [4] proposed the thin wire array design shown in Fig. 2.3 to overcome this limitation for frequencies as low as the microwave regime. In this design, infinetely long thin metallic wires of radius r are arranged in a periodic lattice with lattice constant a. The expression for the permittivity of the periodic wire array is similar to that for bulk metals, with the significant exception that the plasma frequency which is a function of the two geometric parameters a and r is much smaller compared to that in bulk metals. The reason for the decrease in plasma

frequency is two-fold: Firstly, the effective density of electrons is reduced, and secondly, the effective mass of electrons is increasead as a consequence of the self-inductance of the wires. Taking into account these effects, the plasma frequency of the continuous wire array medium in vacuum is expressed as [4]:

$$\omega_p^2 = \frac{2\pi c_0^2}{a^2 \ln(a/r)}, \tag{2.8}$$

where c_0 is the speed of light in vacuum. It is observed that, by choosing appropriate values for the radius and lattice constant, the plasma frequency can be moved down to microwave range. Note that, one key element of the thin wire medium is that the radius of the wires and lattice constant of the array is much smaller compared to the wavelength of EM radiation corresponding to the frequency ω_p. Hence, an effective permittivity ε_{eff} can be defined such that the structure behaves as a homogeneous dielectric medium with permittivity ε_{eff}. In that aspect, it is important that the wires are thin enough for the chosen frequency of operation.

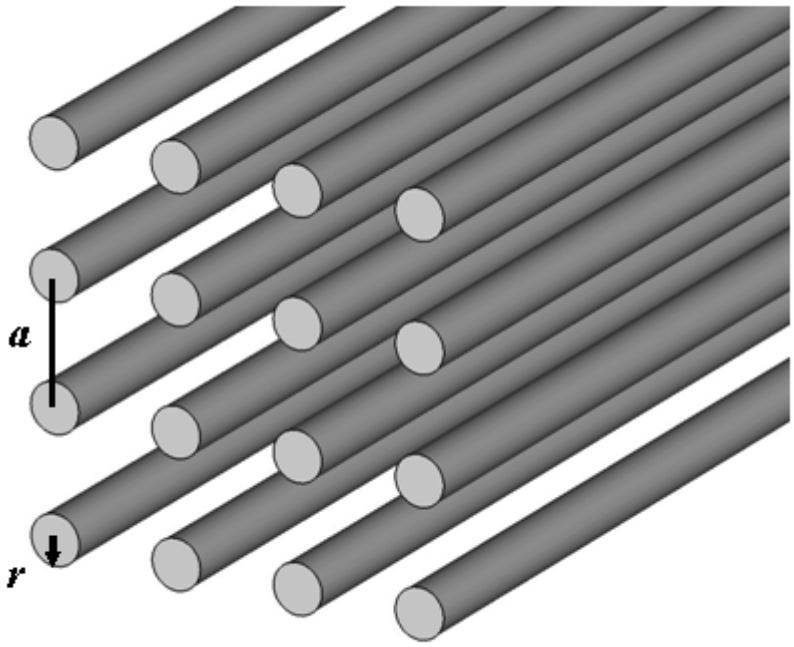

Figure 2.3: The periodic continuous thin wire array constructed for obtaining negative permittivity at lower frequencies. The plasma frequency of the structure is controlled by the two geometrical parameters *a* and *r*, where *a* is the lattice constant and *r* is the radius of the wires.

2.2.2 Negative Permeability ($\mu < 0$)

As discussed previously, both negative permittivity and negative permeability are simultaneously required to obtain a LHM. The continuous wire medium provides the $\varepsilon < 0$ response, however, $\mu < 0$ is still needed. Due to the lack of a magnetic charge in nature, an analogous method to the plasma medium cannot be used. Instead, Sir J.B. Pendry [3] devised an ingenious method of employing an array of metallic ring resonators to enhance the magnetic response of the constructed medium. Figure 2.4 depicts the original resonator element of Pendry, made of two concentric metallic rings with splits.

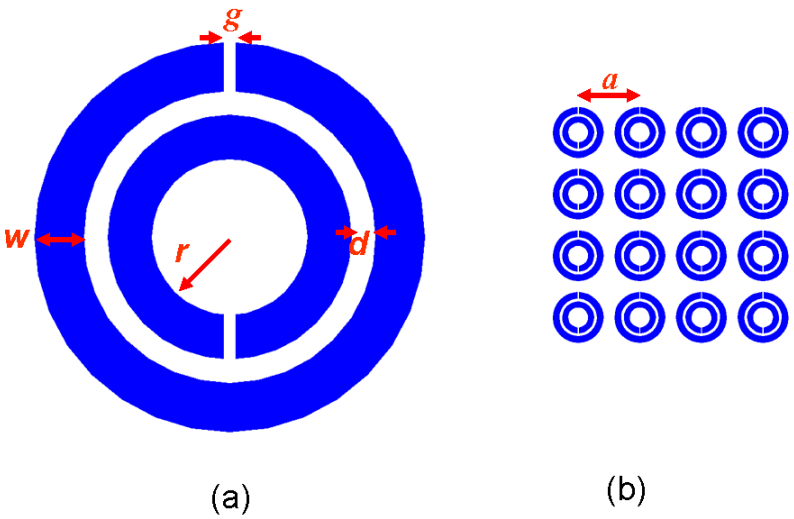

Figure 2.4: (a) Typical SRR element. (b) Array of SRRs. Geometric parameters are: *d*, the separation between rings; *w*, the width of the rings; *g*, the split gap; *r*, the radius of the ring(s), and, *a*, the lattice lattice constant of the array.

The element is named as the split-ring resonator (SRR) after the ring shaped metallic patterns with the splits. The SRR medium can respond resonantly to the magnetic component of EM waves under specific incidence conditions, providing negative permeability within a narrow frequency band immediately after the magnetic resonance. The magnetic resonance is a result of resonant circular currents, excited by the magnetic field of the incident wave, when this field has a magnetic component perpendicular to the plane of the SRR. These circular currents results in the accumulation of charges across the gaps. Therefore each SRR element acts as a series LCR circuit with the inductance of the rings and the capacitance at the ring gaps. The magnetic resonance frequency of such a circuit is given by $\omega_m = 1/\sqrt{LC}$. The reason for the second ring is to generate an additional capacitance between the two rings increasing the total capacitance and reducing the resonance frequency, as the structure becomes more subwavelength in size. Pendry has employed the effective medium theory to calculate the effective permeability of the SRR array resulting in the following equation:

$$\mu_{\text{eff}} = 1 - \frac{F\omega^2}{\omega^2 - \omega_m^2 - i\omega\Gamma_m}, \tag{2.9}$$

where F is the filling factor, and ω_m and Γ_m are the resonance frequency, and the damping factor, respectively. These depend on the geometric parameters of the SRR as follows:

$$\begin{aligned} F &= \pi r^2/a^2, \\ \omega_m &= \frac{3ac_0^2}{\pi \ln(2w/d) r^3}, \\ \Gamma_m &= \frac{2a\sigma}{r\mu_0}, \end{aligned} \tag{2.10}$$

where μ_0 is the permeability in vacuum, *a, d, w, r* are geometric parameters as shown in Fig. 2.4, and σ is the conductivity of the metal. The functional form of the effective permeability in Eqn. 2.9 is plotted in Fig. 2.5. Propagating modes occur below the resonance frequency ω_m, above which a narrow band of negative permeability exists, where no modes can propagate. The frequency,

$$\omega_{mp} = \frac{\omega_m}{\sqrt{1-F}} \tag{2.11}$$

sometimes referred to as the magnetic plasma frequency is particularly noteworthy since the permeability is negative only for the region $\omega_m < \omega < \omega_{mp}$ as shown in Fig. 2.5 (for low loss cases). The real part of the permeability increases from 1 at $\omega = 0$ and makes a peak just below $\omega = \omega_m$ where there is an abrupt change to negative values. It increases from large negative values immediately above ω_m, crossing $\mu = 0$ at $\omega = \omega_{mp}$. At sufficiently high frequencies, the material will stop responding resonantly and permeability will reach unity again. The peak value of permeability, infinite in the case of no loss, is bound by material loss in reality.

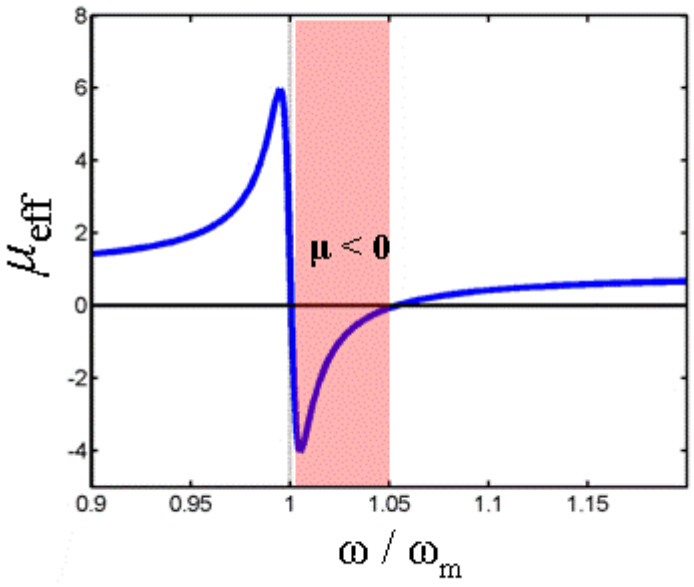

Figure 2.5: Real part of the effective permeability of SRRs, $\mu_{eff,}$ close to the magnetic resonance frequency, ω_m.

It has to be noted that the individual SRR element or a 1D-array of SRRs is anisotropic. The polarization of the incident EM wave plays an important role in the response of the SRR medium. When the magnetic field ***H*** is perpendicular to the plane of the SRR, the magnetically induced resonance is observed. On the other hand, when ***k*** is perpendicular and ***H*** is parallel to the plane of the SRR, then electrically induced (by ***E***) magnetic resonance of the SRR (EEMR effect) can be observed [19, 22, 24, 28, 29].

2.2.3 The Effective Medium and Composed Metamaterial

The original concept of permeability and permittivity were created in order to provide a homogeneous definition of the EM properties of a medium. The macroscopic EM properties of a material are thus definitions of average properties and behaviour of the basic building elements of materials, namely atoms, and electrons while they are

responding to external EM waves. The sizes of these unit building blocks of the natural materials are much smaller than the wavelength of EM waves. Similarly, as long as the basic building blocks of a periodic structure is much smaller than the wavelength of the EM wave in interest, one can consider artificial composite materials (metamaterials) as homogeneous media and define macroscopic properties as an average. To satisfy this constraint, the size of the unit cell, or lattice constant of the periodic structure has to be much smaller compared to the wavelength. Then, the response of the microscopic structures within the unit cell can be considered as an ensemble. However, if this condition is not satisfied, than EM waves would be diffracted and/or refracted by the internal structure of the periodic media and the effective permittivity and permeability concepts cannot be employed.

As discussed above, SRR arrays and wire arrays can provide negative permeability and permittivity, respectively. A material devised of a composition of both of these elements is a promising candidate for a LHM. A composite structure that includes both the periodic thin continuous wires and the SRRs as building blocks is proposed as the first demonstration of the LHMs. When the SRRs and wires do not interfere with each other, such a material preserved both the negative permeability of the SRRs and the negative permittivity of the wires and could yield a negative refractive index if the $\mu < 0$ and $\varepsilon < 0$ bands overlap. The first experimental demonstration of this type of material was accomplished by Smith *et al.* [7] in 2000, where the authors separately measured the transmission of the only-wire medium, only-SRR medium, and the combined composite medium. It was observed that the inclusion of the wires with the SRRs resulted in a pass-band of the structure where previously the stop-band of the only SRRs system was measured. In the last decade, many groups have designed LHMs for operation at various frequency regimes and verified the existence of LH behaviour through experiments [6, 11, 12, 30-38]. One example of a LHM operating around 100 GHz frequency range is shown in Fig. 2.6. In this case, the structure is fabricated using microfabrication techniques since the typical dimensions are on the order of a few μm.

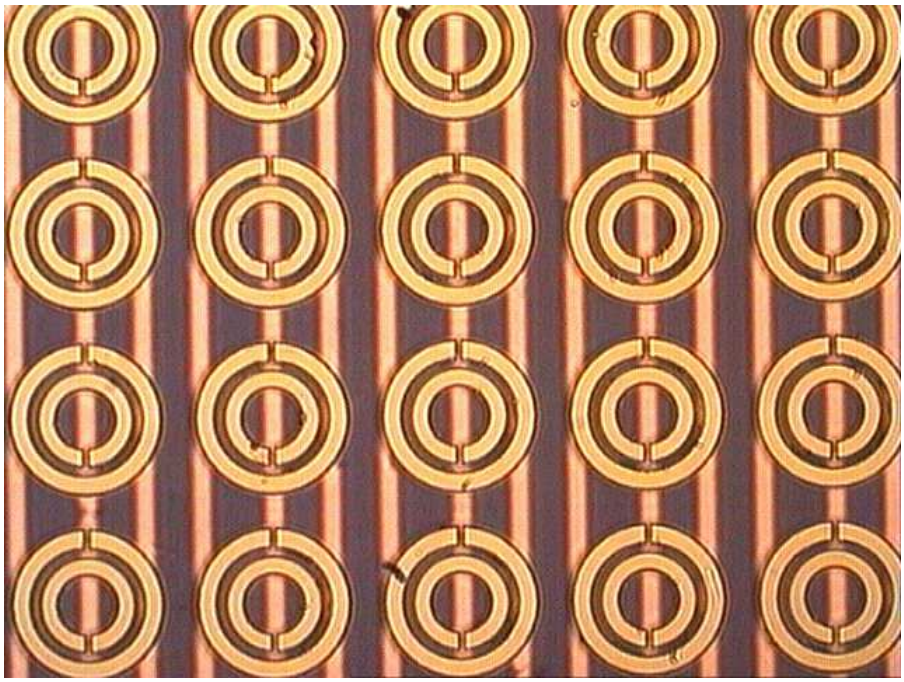

Figure 2.6: Microfabricated SRR and wire LHM [20].

Transmission results obtained from the sample in Fig. 2.6 are shown in Fig. 2.7. It is observed that, in the measurement range, the wire-only medium is not transparent due to the negative permittivity. Similarly, the SRR-only medium has a narrow stop-band (dip in transmission) near 100 GHz, while the composite metamaterial (CMM) of SRRs and wires has a transmission peak in the same frequency regime.

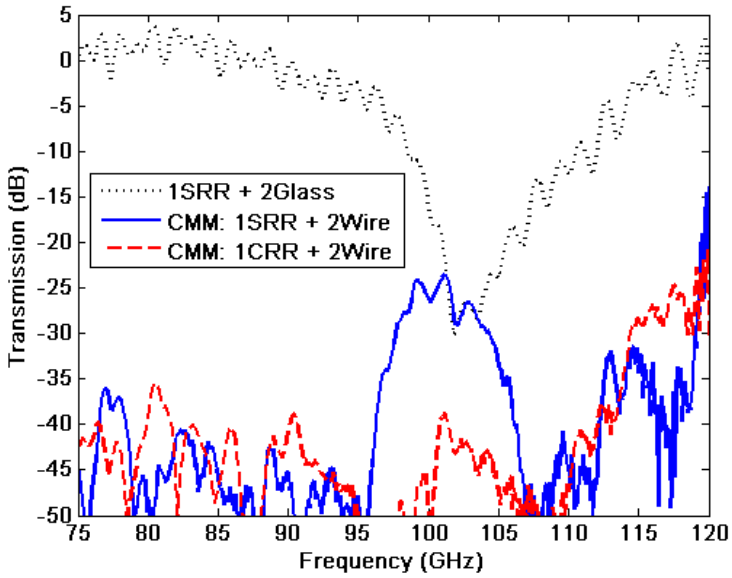

Figure 2.7: Transmission spectra of SRR-only (black dotted), wire-only (red-dashed), and composite metamaterial (CMM) (SRR and wire together) samples [20].

Because LHMs have negative refractive index, an independent way of testing left-handed behaviour is to look for negative angles of refraction. In such experiments, a 2D LHM is composed and the outer boundary of the object is shaped like a prism [39]. It was observed that the LH EM wave behaved consistenly with a negative index of refraction *i.e* it was refracted in the "unconventional side" of the normal direction. Furthermore, the wave was shown to obey the Snell's law with the negative *n* value. This negative angle of refraction phenomenon will be discussed in the following section.

2.3 Negative Refraction

Consider the incidence of an EM wave at the boundary between a RHM and a LHM. Applying the boundary conditions and taking into account the flow of energy across the interface, negative refraction is achieved ie. the wave is refracted at the same side in respect to the normal to the interface as the incident wave. The tangential components of the fields are not changed at transition from the RHM to LHM, however, the normal

components of the fields change their direction since the permittivity and permeability have opposite signs across the interface. [1]. The situation is depicted in Fig. 2.8. It is observed that when a wave is transiting from a RHM to LHM, the normal component $k_{\perp}$ reverses direction. This reversal corresponds to a mirror reflection of the (***E, H, k***) set of vectors in the plane of incidence. This means that the wave refracts at the unconventional opposite side of the normal in contrast to the case when both media are RHM. The paths of the refracted and reflected waves are also shown in Fig. 2.8. The directions of ***S*** and ***k*** vectors are indicated by the black and blue arrows, respectively. The red arrow represents the reflected wave. For comparison purposes, the refraction path in an ordinary medium is also included as the green dashed arrow. The angle of refraction, θ_r, is related to the angle of incidence, θ_i, by Snell's law:

$$\frac{\sin\theta_i}{\sin\theta_r} = \frac{n_2}{n_1} = \frac{-\sqrt{\varepsilon_2\mu_2}}{\sqrt{\varepsilon_1\mu_1}}, \tag{2.12}$$

where $(\varepsilon_1, \mu_1, n_1)$ and $(\varepsilon_2, \mu_2, n_2)$ are the permittivity, permeability, and refractive index of RHM and LHM, respectively. The refractive index, *n*, is defined by the equations:

$$\begin{aligned} n^2 &= \varepsilon\mu, \\ n &= \sqrt{\varepsilon\mu}, \text{ for RHM,} \\ n &= -\sqrt{\varepsilon\mu}, \text{ for LHM,} \end{aligned} \tag{2.13}$$

When taking the square root of n^2 in Eqn. (2.13), the sign of *n* is chosen as to ensure that the square root of either the permittivity or the permeability alone has to have a positive imaginary part as is required for passive media [40].

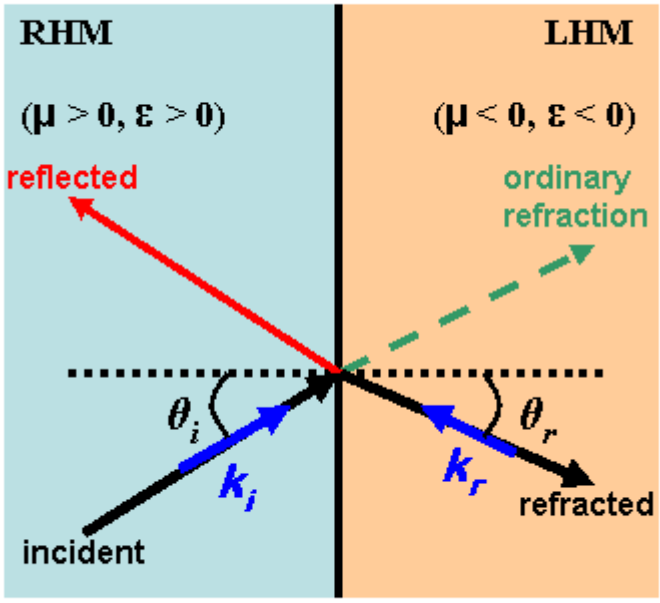

Figure 2.8: Refraction at the boundary between a RHM and a LHM. The directions of *S* and *k* vectors are indicated by the black and blue arrows, respectively. The red arrow represents the reflected wave. The green arrow shows what would be the direction of refraction if the second medium was also RH.

2.4 Phase and Group Velocity

It was mentioned earlier that phase and energy velocities are in opposite directions in LHMs. The phase velocity, $\boldsymbol{v}_p$, and group velocity, $\boldsymbol{v}_g$, are defined in accordance to the same definitions for RHMs:

$$\begin{aligned} \boldsymbol{v}_p &= \frac{\omega}{|k|}\frac{\boldsymbol{k}}{|k|}, \\ \boldsymbol{v}_g &= \nabla_k \omega = \frac{d\omega}{d|k|}\frac{\boldsymbol{k}}{|k|}, \end{aligned} \tag{2.14}$$

where $\frac{\boldsymbol{k}}{|k|}$ is the unit vector along the direction of $\boldsymbol{k}$. The energy velocity, $\boldsymbol{v_e}$, is given by the equation [41]:

$$\boldsymbol{v_e} = \overline{\boldsymbol{S}} \big/ \overline{w}, \tag{2.15}$$

where $\overline{\boldsymbol{S}}$ and $\overline{w}$ are respectively the time average Poynting vector, and the time average power density. It can be shown that the relation between the three velocities, $\boldsymbol{v_p}$, $\boldsymbol{v_g}$, $\boldsymbol{v_e}$ is [41]:

$$v_e = v_g = \frac{v_p}{1 + \frac{\omega}{n}\frac{dn}{d\omega}}, \tag{2.16}$$

and that the energy velocity and group velocity are the same, and are both in opposite direction to the phase velocity in LHMs.

2.5 Dispersion and Dissipation in LHMs

It has to be noted that simultaneously negative permeability and permittivity can be realized only when there is frequency dispersion [42]. To see this, let us consider the energy density for non-dispersive media:

$$W = \frac{1}{2}\varepsilon E^2 + \frac{1}{2}\mu H^2. \tag{2.17}$$

If both ε and μ are negative, and they are non-dispersive, the energy density will be negative. When there is frequency dispersion, *i.e.* $\varepsilon(\omega)$ and $\mu(\omega)$ are both functions of frequency, then Eqn. (2.17) is replaced by:

$$W = \frac{1}{2}E^2\frac{\partial}{\partial\omega}\{\omega\varepsilon(\omega)\} + \frac{1}{2}H^2\frac{\partial}{\partial\omega}\{\omega\mu(\omega)\}. \tag{2.18}$$

The energy density is always positive if,

$$\begin{aligned} &\frac{\partial}{\partial\omega}\{\omega\varepsilon(\omega)\} > 0 \\ &\frac{\partial}{\partial\omega}\{\omega\mu(\omega)\} > 0. \end{aligned} \tag{2.19}$$

This means that $\varepsilon(\omega)$ and $\mu(\omega)$ can simultaneously be negative, as long as the medium is frequency dispersive and Eqns. 2.19 are true.

As discussed above, a LHM is always frequency dispersive. In addition, it has to be dissipative, since all dispersive materials are also dissipative. This can be explained by using the Kramers-Kronig relations [26, 42] connecting the real and imaginary parts of the frequency dispersive permittivity and permeability. Inspection of the Kramers-Kronig relations reveals that the imaginary and real parts of $\varepsilon(\omega)$ and $\mu(\omega)$ coexist in dispersive media, therefore, LHM have to be dissipative.

2.6 LHMs Composed of Short Slab Pairs and Continuous Wires

In the LHM designs that involve SRRs for the realization of negative permeability, the incident EM wave vector has to be parallel to the SRR plane as to ensure that $\boldsymbol{H}$ is perpendicular to the SRRs. This requirement is not a problem in the microwave regime; however, as the frequency of operation increases, and as the unit cell size decreases, it becomes very difficult to satisfy the parallel incidence condition in practical implementations of LHMs (multistack systems of many layers are required to cover the source area). To overcome this limitation, the short slab pair structure was suggested which can give negative permeability response for incidence normal to the plane of the slabs. Combined with continuous wires, the short slab pair structure can lead to left-handed behaviour, in the same way as SRRs and wires systems, but for normal incidence. [17, 43-47]. In Chapter 5 of this thesis, the short slab pairs with continuous wires LHM structure was employed to demonstrate left-handed behavior in the THz frequency regime.

In Fig. 2.9, one unit cell of this structure is shown. In part (a) of the Figure, several unit cells are shown. The periodicities in the x and y directions are noted as a_x and a_y, respectively. The cross section of one layer of the metamaterial is shown in part (b). The thicknesses of the metallic patterns and the dielectric spacer are annotated as t_m and t_d,

respectively. On both sides of the dielectric substrate, the same metallic pattern is placed, therefore the term "*pairs"* is used. This pattern is depicted in Fig. 2.9 (c). The length and width of the short slab pairs are l and w, respectively. The short slab pairs provide the negative permeability of the LHM, and the continuous wires provide the negative permittivity. When the EM wave is perpendicular, and $\boldsymbol{E}$ is parallel to the continuous wires, $\boldsymbol{H}$ induces a magnetic resonance at the short slab pair, similar to that of the SRR structure. The magnetic resonance frequency of the short slab pairs is given by [47]:

$$\omega_m = 2\frac{c_0}{\sqrt{\varepsilon_b}}\frac{1}{l}, \tag{2.20}$$

where ε_b is the permittivity of the dielectric spacer medium. Note that the magnetic resonance frequency is inversely proportional to the length of the short slabs, and independent from the rest of the geometric properties. This interesting property has been verified by experimental studies [46, 48].

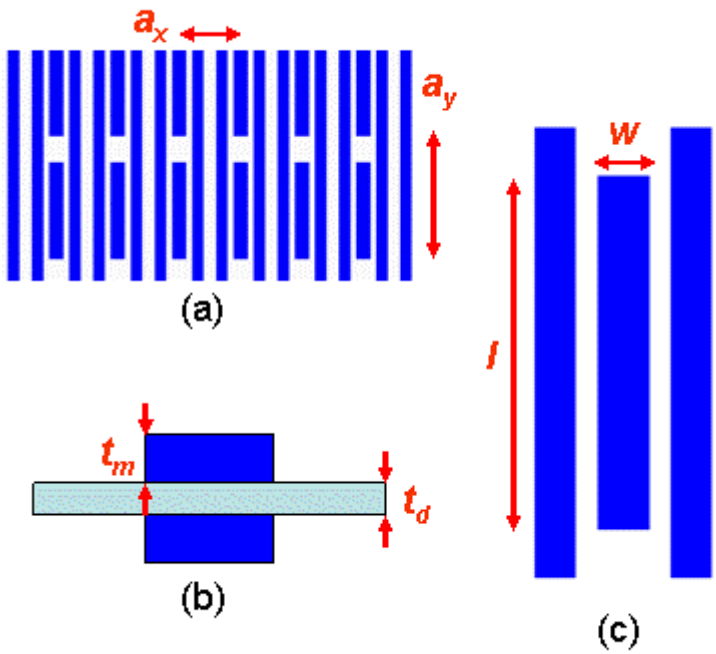

Figure 2.9: The short slab pair and continuous wires LHM. (a) Several unit cells of the structure. (b) Cross section of the structure. (c) One unit cell of the structure. The unit cell size in the x and y directions are a_x and a_y, respectively. The thicknesses of the metallic patterns and the dielectric spacer are t_m and t_d, respectively. The length and width of the short slab pairs are w and l, respectively.

2.7 Retrieval Procedure of the Effective Medium Parameters

In this section, we will present the method used in for calculating the effective medium parameters: the retrieval procedure. The method was first developed by Smith et al to calculate the effective electric permittivity and magnetic permeability from numerical or experimental transmission and reflection values [49]. The retrieval procedure has proven to be essential for metamaterial and left-handed material studies, since it provides us further information about the effective medium parameters and guides us in determining the left-handed behaviour.

First, in order to simplify, we consider our metamaterial as a slab of homogenuous material. When a plane electromagnetic wave is incident on a homogenuous slab, the amplitudes of the scattered waves can be written as:

$$t = \frac{1}{\cos(nk_0L) - \frac{i}{2}(z + 1/z)\sin(nk_0L)}, \tag{2.21}$$

$$r = \frac{-\frac{i}{2}(z - 1/z)\sin(nk_0L)}{\cos(nk_0L) - \frac{i}{2}(z + \frac{1}{z})\sin(nk_0L)}, \tag{2.22}$$

where k_0 is the free space wavenumber, L is the thickness of the slab, z is the characteristic impedance, and n is the index of refraction of the material. The Eqns. (2.21) and (2.22) are solved as:

$$n = \frac{1}{k_0L}\cos^{-1}\left(\frac{1}{2t}(1 - r^2 + t^2)\right) + \frac{2m\pi}{k_0L}, \tag{2.23}$$

$$z = \pm\sqrt{\frac{(1+r)^2 - t^2}{(1-r)^2 - t^2}}, \tag{2.24}$$

which allow us to calculate the effective permittivity and permeability as:

$$\varepsilon = n/z, \quad \mu = nz. \tag{2.25}$$

Although these equations seem simple, there are a few problems in practice. The choice of the sign in Eqn. (2.24), and the branch of the $\cos^{-1}$ function in Eqn. (2.23), are in general determined by further constraints such as considering the behaviour far from resonance. It is required to know the length of the slab exactly, which is complicated for metamaterials. These ambiguities can be resolved by considering multiple slabs with different thicknesses and solving for unique constitutive parameters from the retrieval of these. It has to be noted that, the retrieval procedure has been demonstrated to be feasible and valid by many studies in the field.

2.8 Progress in LHMs

In left-handed materials, negative permeability was realized by SRR arrays, and negative permittivity was realized by continuous wire arrays, separately. In the earliest experimental studies, overlapping in the resonance dip of SRR-only structures, the stopband of the wires-only structures, and a peak in the transmission of a composite structure containing both the wires and SRRs were considered proof of left-handedness. The basic assumption for this was that the SRRs and wires would behave in the same way whether they were measured alone or in the composite medium. However, later, it was shown that this assumption is not true and the plasma frequency in the composite medium is much lower compared to the plasma frequency of the wires alone. [50, 51]. It was shown that for some structures, seemingly left-handed peaks determined by the above described separate observation method, are indeed right handed. This resulted in the general acceptance that transmission measurements of the components alone are not sufficient to claim LH behaviour, and one needs to calculate the effective parameters. Smith et al. proposed a retrieval method [49] to calculate the effective permeability and permittivity of a LHM, by modeling the material as an isotropic homogeneous slab, and using experimental data or numerical calculations for obtaining the reflectance and transmittance of the slab. Although qualitative behavior, such as resonances of LHMs, was predicted accurately by the retrieval method, it was noted that there was significant deviation from theoretical predictions and retrieved effective parameters [49, 52-55]. These effects were attributed to the periodicity of metamaterials [56]. Later, specialized retrieval schemes that take into

account inhomogeneous metamaterials [57], anisotropic metamaterials [58], asymmetric unit cells, and different polarization [28, 59] effects were also devised.

Since the first demonstration of artificial metamaterials, there has been a steady effort to realize LHMs at higher frequencies, all the way to the optical regime. The obvious method of scaling structure sizes from a few millimeters down to tens of nanometers resulted in SRR-systems operating at a few THz [29] to 200 THz [19]. Since it was not possible to construct micrometer and submicron scale multilayer SRR systems that would allow the demonstration of the magnetic resonance for propagation parallel to the SRRs plane, the magnetic resonance was measured at normal to SRR-plane incidence from a single layer, by the so called electrical excitation of magnetic resonance (EEMR) effect [28] in most THz and all optical experiments. At low frequency, up to a few THz, the magnetic resonance frequency scales up linearly as structure size scales down. At higher frequencies, this scaling breaks down, the upscaling of frequency saturates, and the strength of resonance decreases, eventually failing to achieve a negative permeability value. The short slab pairs and continuous wires metamaterial was proposed to push the saturation regime to higher frequencies [17, 43, 45, 47]. In this design normal incidence is employed, and the structure is more appropriate for nanoscale fabrication. The fishnet structure is a variation of the short slab pairs and continuous wires structure, able to give negative ε and μ at optical frequencies [60, 61] . In this structure continuous wires/stripes are employed in the directions of both $\boldsymbol{E}$ and $\boldsymbol{H}$. The former provide negative ε, while the latter provide negative μ. The fishnet design is considered as todays best LHM design in the optical regime.

Although LHM at optical frequencies are realized by these new designs, the increase in losses is the biggest challenge [62]. One way of estimating the loss, is the figure of merit (FOM), defined as the absolute value of the ratio of the real and imaginary parts of the refractive index, ($\mathrm{Re}\{n\}/\mathrm{Im}\{n\}$). The FOM in the existing experimental structures decreases from on the order of 100 for SRRs at microwave frequencies to 0.5 for fishnet structures at optical frequencies[18, 63]. This low FOM limits the uses of LHMs at optical frequencies, in applications such as the perfect lens[64, 65].

Chapter 3

Composite Metamaterials Operating at Microwave Frequencies

3.1 Introduction

As it was mentioned in the previous sections, left-handed materials are composite metamaterials that have the unique physical property of having both the electrical permittivity (ε) and the magnetic permeability (μ) negative. Thus, they are artificial materials having a negative refractive index (n) at a frequency region in which they are designed to operate.

Left-handed materials were first proposed by Veselago in 1968 [1]. In 2000 Smith *et al.* demonstrated the realization of the first left-handed material (LHM) which consisted of an array of SRRs and wires, in alternating layers [7]. Since the original microwave experiment by Smith *et al.* several composite metamaterials (CMMs) were fabricated [31, 35] that exhibited a pass band in which it was assumed that ε and μ are both negative. This assumption was based on transmission measurements of the wires alone, the SRRs alone, and the CMMs. The occurrence of a CMM transmission peak at the stop bands of the SRRs and within the stop band of the wires structures was taken as evidence for LH

behavior. Moreover, there is a significant amount of numerical work in which the transmission and reflection data, losses and effective parameters of the composite metamaterials have been investigated [53, 54, 66-70].

In this chapter the transmission properties of SRRs, continuous wires and CMMs made of SRRs and wires are investigated in the microwave frequency regime. Moreover, the criteria in identifying the left-handed behaviour at a certain frequency region are also discussed. Finally, the transmission properties of the SRRs for different electromagnetic field polarizations and propagation directions are studied in microwave frequencies. It was found unexpectedly that the incident electric field ***E*** couples to the magnetic resonance of the SRR when the EM waves propagate perpendicular to the SRR plane and the SRR has not mirror symmetry with respect to the incident ***E*.** This effect is called the effect of the electric coupling to the magnetic resonance (EEMR). Although this effect is found while investigating the composite metamaterials operating in microwave frequencies, it allowed us to study mainly the μm-scale metamaterials (see Chapter 4). Thus, discovering the EEMR enabled us to investigate composite metamaterials operating in the far infrared and optical frequency regions.

3.2 Determining the LH behaviour

As it was mentioned in the introduction section, in the early studies on LH materials, the occurance of a CMM transmission peak at the stop band of the SRRs and wires structures was taken as an evidence of the LH behaviour. This assumption was true only when it was thought that SRRs only exhibit a resonant magnetic response resulting in a negative effective permeability, μ_{eff}, over a finite frequency range. However, later, it was found that the SRRs, in addition to their resonant magnetic response at ω_m, exhibit a resonant electric response at ω_o which is similar to the electric response of a system of cut wires (wires of finite length along the incident ***E*** direction). In this section we will demonstrate that this electric response together with the electric response of the continuous wires of the CMM, results in a new effective plasma frequency, ω_p', which is considerably lower

than the plasma frequency of the wires, ω_p. Therefore, here we will present new criteria for the identification of the LH behaviour.

In order to investigate the effects mentioned above, several sets of metamaterials consisting of SRRs, closed SRRs (SRRs with no gaps), CMMs and CMMs with closed SRRs were fabricated. The free-space microwave measurements on CMMs (consisting of SRRs and wire structures - either on the same dielectric board or on alternating boards) are performed in order to investigate the transmission properties. The CMMs studied here, consisting of SRRs and continuous wires, were fabricated using a conventional printed circuit board process, with copper patterns on 1,6mm thick FR-4 dielectric substrates. The FR-4 board has a dielectric constant of ~4.8 and a dissipation factor of ~0.017 at 1.5 GHz.

First, CMMs with SRRs and wire structures on the same side of the boards were fabricated. This in-plane CMM structure can be seen in Fig. 3.1. The geometry of the unit cell (u.c.) is shown in the inset of Fig. 3.2. The u.c. dimensions are a_k=5 mm, a_E=3.63 mm, and a_H=5.6 mm and 6.3 mm, and it contains one copper wire per SRR. The width of the copper wire is 0.5 mm while its thickness is 0.03 mm. For the SRRs fabricated within this work the ring width, ring distance, ring separation, and the gaps of the rings are all 0.33 mm. The larger SRR side is 3 mm and the thickness of the metal is 30 μm.

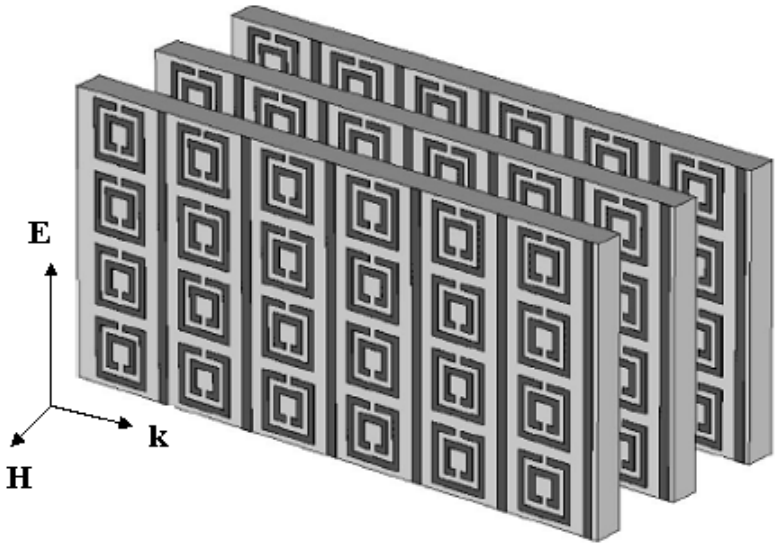

Figure 3.1: Schematic drawing of an in-plane metamaterial composed of SRRs and continuous wires on the same side of the dielectric board.

The periodicity along the ***H*** direction was obtained by stacking the boards. The total system consisted of 25x25x25 u.c. Furthermore, variations of the above CMMs were fabricated, containing closed SRRs (SRRs without the gaps) in the place of SRRs, as well as only SRRs and only wires. As it was mentioned previously, we especially need to measure the transmission spectrum of the CMMs containing closed SRRs in order to prove that the SRRs have an electric response (like a cut wire) along with the magnetic response and thus, this affects the plasma frequency of the system (decreases the plasma frequency).

The transmission of EM waves through in-plane CMMs, SRRs-only and wires-only structures, and finally CMMs containing SRRs with no gaps was measured. The transmission measurements were performed in free space, using a Hewlett-Packard 8722 ES network analyzer and microwave standard-gain horn antennas. For all measurements the wave propagation was parallel to the boards with the **E** polarization parallel to the wires and the continuous sides of the SRRs (see the inset of Fig.3.2).

The measured T spectra of SRRs-only structure (dotted line), wires-only structure (dashed line), and of the in-plane CMM (solid line), for $a_{\mathbf{H}}$=5.6 mm can be seen in Figure 3.2 (a). The SRRs-only structure shows the expected T dip at 8.5–10 GHz, corresponding to the magnetic resonance of the SRR, while the wires-only structure shows a cutoff frequency at 10.5 GHz that corresponds to its plasma frequency, ω_p. The CMM (solid line) shows a T peak between 8.5 and 9.5 GHz, i.e., within the frequency region of the SRRs dip. The occurrence of a CMM transmission peak within the stop bands of the SRR-only and wires-only structures was originally taken as clear evidence for the appearance of LH behavior [6, 31]. The fault with this reasoning is that it ignores the effects of the SRRs on the electric response of the wires. In this study these effects were demonstrated experimentally by closing the gaps of the SRRs. By closing the gaps of the SRRs in the CMM, it was expected that the magnetic resonance of the SRRs to be switched off and thus to really monitor only the electric response of the CMM. The changes in the electric response of the CMM from the closing of the gaps are expected to be weak, since only a small amount of metal is added (in the gaps of the SRRs), while the symmetry is preserved.

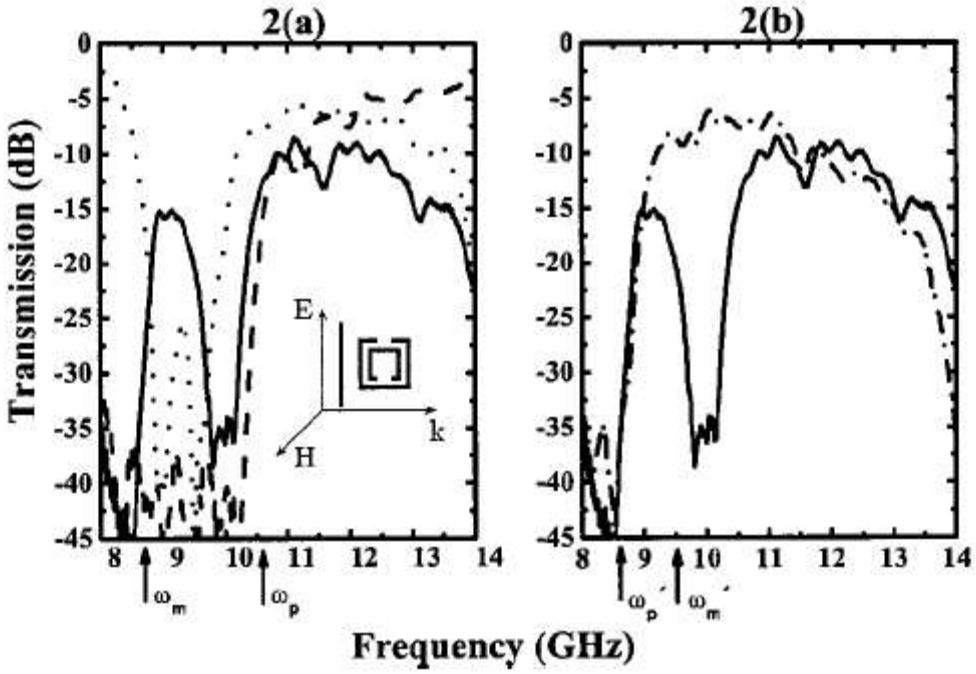

Figure 3.2: (a) Measured transmission spectra for *in-plane* metamaterials composed of SRRs and continuous wires (solid line), SRR-only structures (dotted line), and wires-only structures (dashed line). The latter two identify ω_m and ω_p. The width of the continuous wires is 0.5 mm. The inset shows the unit cell of the *in-plane* CMM (SRRs plus wires) as well as the electric field orientation and polarization; (b) in-plane CMM solid curve redrawn to show that the same threshold is exhibited (at ω_p') as in the nonmagnetic structure consisting of closed-SRRs and wires (dotted-dashed line). Thus the transmission peak in the CMM curve is actually RH and not LH; the dip in the CMM spectrum at ~10GHz corresponds to the SRR stop band, which is shifted due to the presence of the wires[50].

As can be clearly seen from Fig. 3.2 (b), the *T* spectrum for the metamaterial with closed SRRs (dotted-dashed line) is almost the same with that of the ordinary CMM (solid line), with the main difference being the absence of the dip at 10 GHz, which indicates that this dip is due to the SRR magnetic response. Moreover, it is observed that the combination of the wires with the SRRs shifts the effective plasma frequency, ω_p', of the CMM to ~8.5 GHz, which is lower than the plasma frequency of the wires-only array (ω_p~10.5 GHz). Hence, we must conclude that in the CMM $\varepsilon > 0$ for $f > 8.5$ GHz;

consequently, there should be no LH peak for f > 8.5 GHz. Therefore, the peak observed at ~9 GHz ought to be RH. On the other hand, based on the same arguments one should expect a dip and not a peak at ~9 GHz, since in this region $\varepsilon > 0$ and $\mu < 0$ (due to the SRR resonance). To explain this apparent discrepancy the influence of the wires on the magnetic resonance frequency, ω_m, of the SRRs is examined. It is revealed numerically [71] that the currents in the wires tend, on the average, to diminish the magnetic flux on the SRRs and thus to decrease their effective inductance (L_{eff}); the net result is an increase of the magnetic resonance frequency, since it is given by $1/ (L_{eff}\ C_{eff}\ )^{1/2}$ (C_{eff} is the effective capacitance). In our case, this led to a shift of the resonance frequency from ω_m ~ 8.5 GHz to ω_m' ~ 9.5 GHz, explaining the peak at ~ 9 GHz as RH and accounting for the dip in the CMM T spectrum at ~10 GHz (as $\varepsilon > 0$ and $\mu < 0$). To further check this interpretation the wires are placed off-plane and symmetrically with respect to the SRRs (see the inset of Fig. 3.4). In this case the currents in the wires have no net effect on the magnetic flux in the SRRs, and consequently we expect ω_m not to be influenced by the wires. Our microwave measurements for off-plane CMM structures confirmed this expectation.

For obtaining a real LH peak it is necessary ω_p' to be larger than ω_m'. To achieve this, the width of the copper wires is doubled to 1 mm. The T data for the newly developed in-plane CMM are shown in Figs. 3.3(a) and 3.3(b). It is shown that ω_p' is now at ~10.4 GHz [dotted-dashed line in Fig. 3.3(b)]. In this case ω_p' is clearly higher than ω_m' and thus the observed CMM peak [see solid line in Figs. 3.3(a) and 3.3(b)], centered at ~ 9.5 GHz, is really LH.

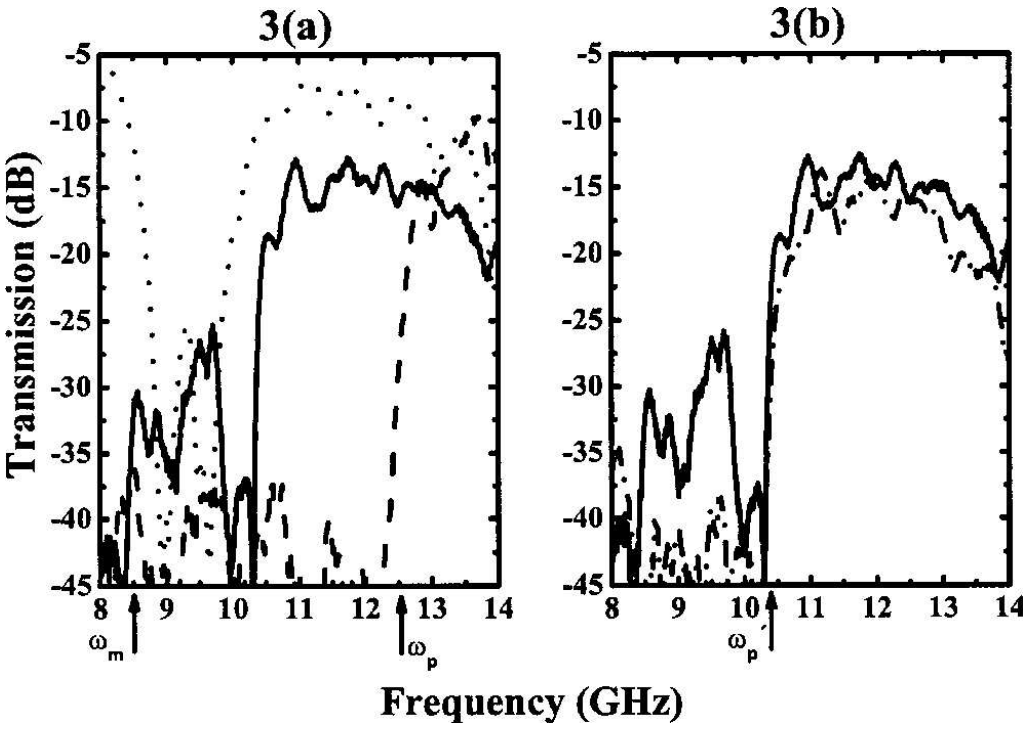

Figure 3.3: (a) Measured transmission spectra for *in-plane* CMMs (solid line), SRRs-only structures (dotted line) and wires-only structures (dashed line). The width of the continuous wires has been doubled to 1 mm; (b) the coincidence of the CMM solid curve with the closed SRRs plus wires (dotted-dashed) curve at ~10GHz determines the effective plasma frequency, ω_p', which is now well above the CMM transmission peak at ~9GHz identified as left-handed.

Finally, the transmittance of the LH peak is aimed to be improved by considering off-plane CMMs (theoretical results indicate higher transmittance for off-plane than for in-plane cases)[51]. In this case, the wires are printed on the back side of the boards opposite to the gaps of the SRRs. The unit cell for this case is shown in the inset of Fig. 3.4; its dimensions are a_k =5 mm, a_E =3.63 mm, and a_H=5.6 mm, 3.1 mm, and 2.6 mm. The total system consists again of 25x25x25 unit cells.

The *T* spectrum for the off-plane CMM with a_H =3.1 mm is shown in Figure 3.4. A well-defined peak can be clearly observed at ~ 9.5 GHz. The closing of the gaps of the

SRRs demonstrates that ω_p' is at ~ 10.5 GHz. Since the SRRs-only T dip is at 8.5–10 GHz, it is apparent that the observed peak is LH.

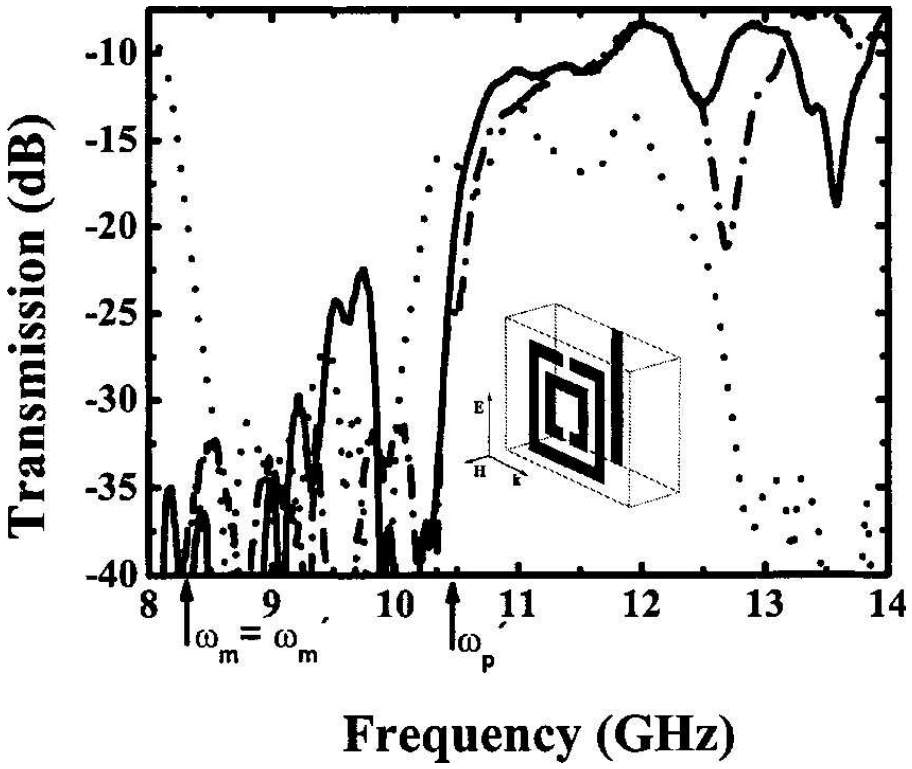

Figure 3.4: Measured transmission spectra for *off-plane* CMMs composed of SRR and continuous wires (solid line), SRRs-only structures (dotted line) and structures consisting of closed SRRs and wires (dotted-dashed line). The width of the continuous wires is 1 mm. The inset shows the unit cell of the *off-plane* CMM (SRRs plus wires) as well as the incident field orientation and polarization. The frequencies $\omega_m = \omega_m'$ and ω_p' are well separated and the CMM peak at ~9.5GHz is clearly LH.

As a conclusion, in this study, it is shown experimentally that the effective plasma frequency, ω_p', of the CMM composed of SRRs and continuous wires is lower than the wires-only plasma frequency, ω_p. It is also demonstrated how to obtain experimentally an accurate value for ω_p'. Furthermore, it is shown that the in-plane wires, as opposed to the off plane configuration, push the magnetic resonance frequency, ω_m, to a slightly higher value, ω_m'. Hence a peak in the EM wave transmission through a CMM is LH only if $\omega_m' < \omega_p'$ and if it lies between ω_m' and ω_p'. It must be noted that in contrast, the condition ω_m

$< \omega_p$, which is widely used as a criterion for LH behavior, does not guarantee that an observed peak is LH, since the mutual interactions of wires and SRRs decrease the positive difference $\omega_p - \omega_m$ and possibly eliminate it altogether. To demonstrate these effects microwave transmission measurements are presented where $\omega_m < \omega_p$ but $\omega_m' > \omega_p'$ and hence the observed peak was RH, as well as measurements where $\omega_m' < \omega_p'$ and the observed peak was LH.

3.3 Effect of Electric Coupling to the Magnetic Resonance (EEMR)

In this study, the results for the transmission coefficient of a lattice of SRRs alone for different orientations of the SRR with respect to the external electric field, **E**, and the direction of propagation are investigated both numerically and experimentally. Incidence is always normal to some face of the cubic unit cell of this metamaterial, which implies four distinct orientations as it can be seen in Figure 3.5. It was considered an obvious fact that an incident EM wave excites the magnetic resonance of the SRR only through its magnetic field; hence one could conclude that this magnetic resonance appears only if the external magnetic field **H** is perpendicular to the SRR plane, which in turn implies a direction of propagation parallel to the SRR [Figs. 3.5(a) and 3.5(b)]. If **H** is parallel to the SRR [Figs. 3.5(c) and 3.5(d)] no coupling to the magnetic resonance was expected. In this study it is shown that, this is not always the case. If the direction of propagation is perpendicular to the SRR plane and the incident **E** is parallel to the gap-bearing sides of the SRR [Fig. 3.5(d)], an electric coupling of the incident EM wave to the magnetic resonance of the SRR occurs.

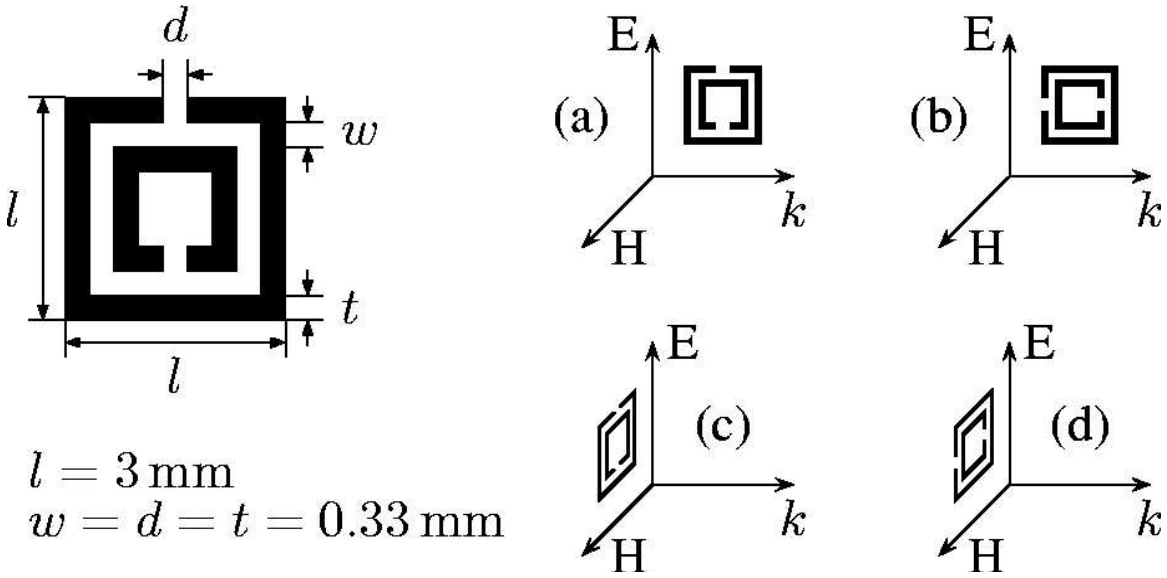

Figure 3.5: Left–hand side: SRR geometry studied. Right–hand side: The four studied orientations of the SRR with respect to the triad k, E, H of the incident EM field. The two additional orientations, where the SRR are on the H-k plane, produce no electric or magnetic response.

This means that the electric field excites the resonant oscillation of the circular current inside the SRR, influencing either the behavior of ε(ω) only [as in Fig. 3.5(d)] or ε(ω) and μ(ω) [as in Fig. 3.5(b)]. Experiments as well as numerical results reveal that for propagation perpendicular to the SRR plane, a dip in the transmission spectrum close to the magnetic resonance ω_m of the SRR appears whenever the mirror symmetry of the SRR with respect to the direction of the electric field is broken by the gaps of its rings [Fig. 3.5(d)]. It should be noted that the possibility of such electric coupling to the magnetic resonance does also affect the conventional orientations [Figs. 3.5(a), and 3.5(b)], that have the direction of propagation along the SRR plane. A simple analytic model is given that provides an explanation for the phenomenon[28].

In order to study this phenomenon experimentally a CMM consisting of SRRs was fabricated using a conventional printed circuit board process as it was mentioned in the previous section (see section 3.2). The design and dimensions of the SRRcan be seen in figure 3.5. Then the total structure was constructed by stacking together the SRR structures in a periodic arrangement. The unit cell contains one SRR and has the

dimensions 5 mm (parallel to the cut sides), 3.63 mm (parallel to the continuous sides), and 5.6 mm (perpendicular to the SRR plane). The transmission measurements were performed as it was explained in the previous section (see section 3.2).

The four nontrivial orientations of the SRR, which are shown in Figure 3.5, are studied. Figure 3.6 presents the measured transmission spectra, *T*, of the metamaterial. The continuous line (line *a*) corresponds to the conventional case shown in Fig. 3.5 (a), with **H** perpendicular to the SRR plane and **E** parallel to the symmetry axis of the SRR. Notice that *T* exhibits a stop band at 8.5–10.0 GHz, due to the magnetic resonance. The dashed line (line *b*) shows *T* for the orientation of Fig. 3.5 (b); here **E** is no longer parallel to the symmetry axis of the SRR and thus there is no longer a mirror symmetry of the combined system of SRR plus EM field. It should be noted that now *T* exhibits a much wider stop band at 8–10.5 GHz, starting at lower frequency. Very interesting results are obtained by comparing *T* for the two cases shown in Figs. 3.5 (c) and 3.5 (d), for which there is no coupling to the magnetic field since **H** is parallel to the SRR plane. For the case of Fig. 3.5 (c), where **E** is parallel to the symmetry axis of the SRR, no structure is observed around the magnetic resonance frequency (line *c* in Fig. 3.6), as expected. However in the case of Fig. 3.5 (d), where the SRR exhibits no mirror symmetry with respect to the incident electric field, a strong stop band in *T* around ω_m is observed (line *d*), similar to that of the conventional case [Fig. 3.5 (a)]. This strongly suggests that the magnetic resonance can be excited by the electric field provided that there is no mirror symmetry.

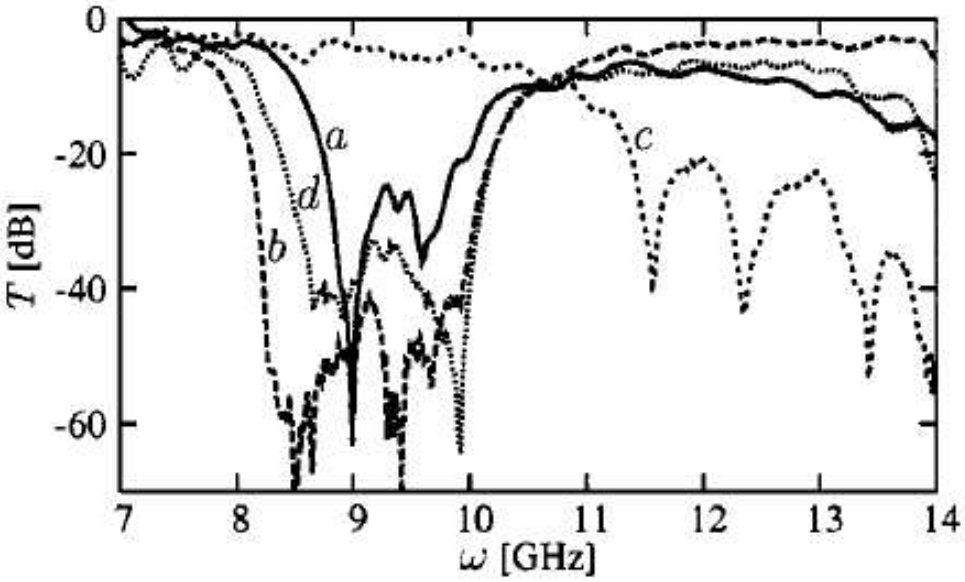

Figure 3.6: Measured transmission spectra of a lattice of SRRs for the four different orientations shown in Fig. 3.5 (a), (b), (c) and (d).

These observations are in good agreement with the numerical results, presented in Fig. 3.7. For the propagation perpendicular to the SRR we observe a stop band only if **E** is parallel to the cut-bearing sides of the SRR and ‘‘sees’’ its asymmetry (line *d*); otherwise we have transparency (line *c*).

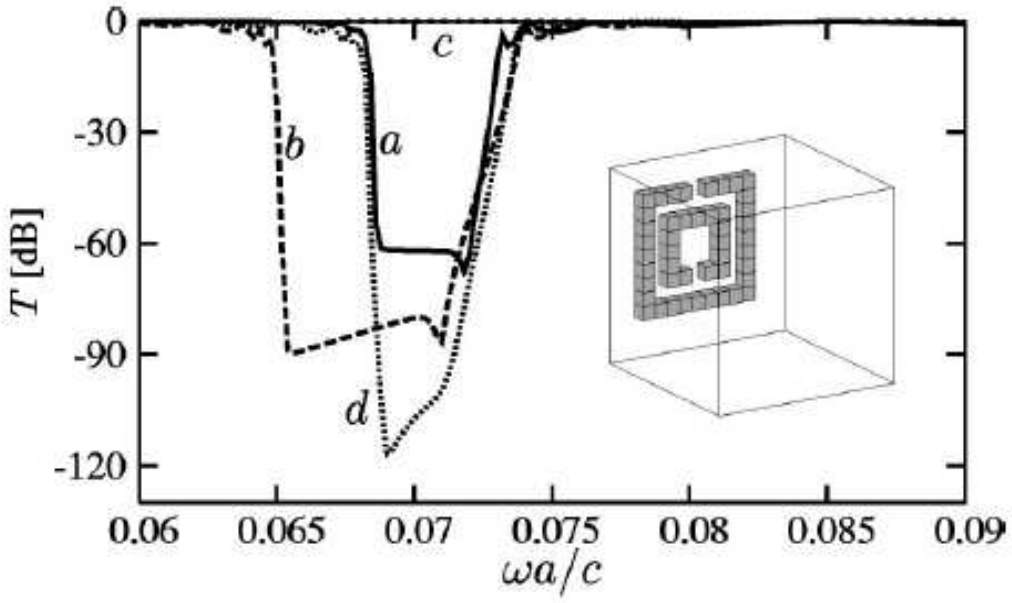

Figure 3.7: Calculated transmission spectra of a lattice of SRRs for the four different orientations shown in Fig. 3.5 (a), (b), (c) and (d). The curve *c* practically coincides with the axis. The discretization of one particular SRR is shown in the inset.

This excitation of magnetic resonance by the incident electric field can be explained as follows (for simplicity we consider a single ring SRR in the following discussion) : As shown in Fig. 3.8, the SRR ring will experience different spatial distributions of the induced polarization, depending on the relative orientation of **E** with the SRR gap. If **E** is parallel to the no gap sides of the SRR its polarization will be symmetric and the polarization current is only flowing up and down the sides of the SRR, as shown in Fig. 3.8 (a). If the SRR is turned by 90° as shown in Fig. 3.8 (b), the broken symmetry leads to a different configuration of surface charges on both sides of the SRR, connected with a compensating current flowing between the sides. This current contributes to the circulating current inside the SRR and hence couples to the magnetic resonance. We directly observed both types of currents in the FDTD simulations; as an example, the component of the current parallel to the external electric field is shown in Fig. 3.8. The retrieval procedure for ε and μ indicates that the electric coupling leads to a resonant electric response (i.e. resonance in ε) near ω_m. Also the experimentally observed

broadening of the conventional SRR dip for the turned SRR was found numerically as well (line *b* in Fig. 3.7). The reason is the *additional* electric coupling which adds an electric resonant response [in ε(μ)] directly below the resonant magnetic response. Closing the gaps of the SRR we observed both in the experiment and in the simulations that the dips disappeared.

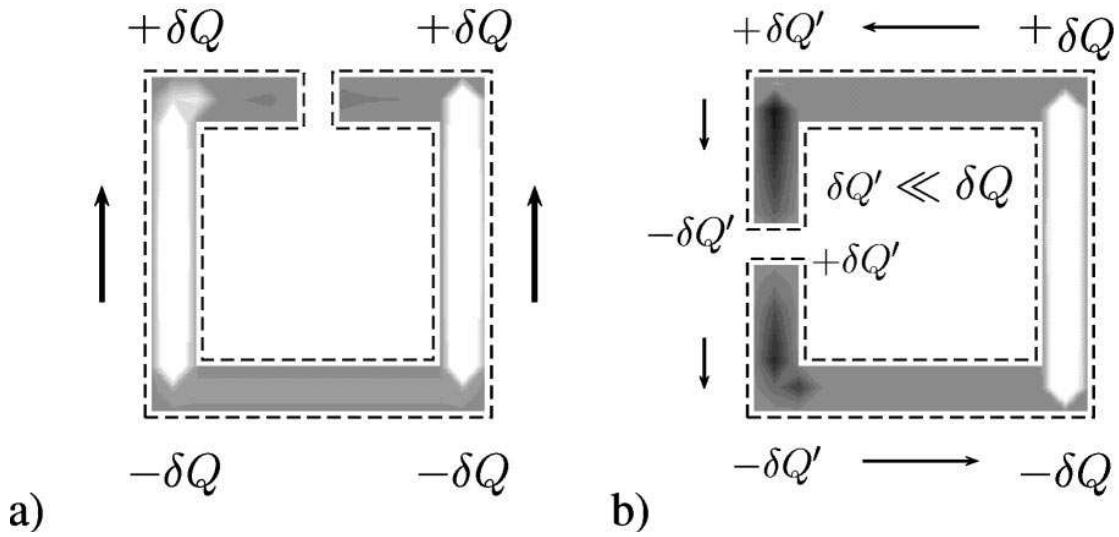

Figure 3.8: Simple drawing for the polarization in two different orientations of a single ring SRR. The external electric field points upward. Only in case of broken symmetry (b) a circular current will appear which excites the magnetic resonance of the SRR. The interior of the ring shows FDTD data for the current component $J_{\parallel}E$ at a fixed time for normal incidence [Figs. 3.5(c) and 3.5(d)] as a gray scale plot.

In summary, the propagation of EM waves for different orientation of the SRR has been studied experimentally and theoretically. It was found that the incident electric field couples to the magnetic resonance of the SRR, provided its direction is such as to break the mirror symmetry of the SRR. This unexpected electric coupling to the magnetic resonance of the SRR is of fundamental importance for the design of LHMs in higher dimensions. Besides, EEMR effect allows us to investigate metamaterials operating at the higher frequency region. A detailed discussion on this subject will be presented in Chapter 5.

Chapter 4

Numerical Studies of Left-handed Materials

4.1 Introduction

In this chapter we will present a systematic numerical study of the transmission properties of LHMs and SRRs. The Microwave Studio (MWS) code was used as well as a retrieval procedure for the calculation of effective ε and μ parameters.

The Microwave Studio (MWS) code is suitable for the description of a real system, because a large number of mesh-cells may be required for certain metamaterial geometries [which makes the calculation intractable for other methods like Transfer matrix method (TMM),]. Thus, we use the finite integration technique employed through Microwave Studio commercial software for transmission calculations together with a retrieval procedure [49], which extracts the effective electric permittivity, ε, and magnetic permeability, μ, by inverting the reflection and transmission results, considering our metamaterial as a homogeneous effective medium.

In the first part we will present a detailed parametric study of the SRR. The dependence of the magnetic resonance frequency, ωm, and of the electric resonance frequency, ω_o, on the SRR size for a single-ring SRR in the propagation direction is presented and a comparison between circular and rectangular SRRs is given as well. Besides, a comparison between the resonance frequencies of single-ring SRRs and that of double-ring SRRs is given. Then the dependence of ω_m on the width and depth of the rings, on their separation, on the ring gap and on the background material is discussed, as well as the influence on the SRR transmission of the SRR orientation relative to the incident electric field and the issue of the electric coupling to the magnetic resonance. Moreover, we present a detailed study of the dependence of the LH transmission on the dielectric constant of the substrate, on the distance between the wires and the SRRs, on the thickness of the unit cell and on the orientation of the SRRs relative to the wires (considering combined metamaterials of rectangular double-ring SRRs and wires).

We also studied the effective plasma frequency of the combined system of wires and closed SRRs. Finally symmetric SRRs are studied. Since they do not couple with the incident electric field, they can be used in 2D and 3D isotropic metamaterial designs which have a great importance for future studies.

4.2 Parametric studies of SRRs

4.2.1 Single Ring SRRs

In the beginning of the studies related with the SRR structure, it was thought that it is necessary to have a double-ring SRR in order to obtain a magnetic resonance which possesses a region with $\mu < 0$. But later it was found that a single ring with a cut (a single-ring SRR) behaves also as a magnetic resonator.

First the single ring SRR studies are presented. As a start, the effect of the shape of the SRR is investigated. In Figure 4.1(a), the transmission as a function of frequency for a single-ring SRR is plotted, both for a circular and a square SRR. They both have the same linear dimension and metal and unit cell characteristics. It can be noted that both the

circular and the square single-ring SRRs give a dip in the transmission coefficient (the first dip in Figure 4.1(a)) which is associated with a negative μ regime (see panel (b)). It was found that there is no qualitative difference between those two structures. However, for circular and square single-ring SRRs with the same linear dimension, metal characteristics and gaps, the circular SRR shows, in general, higher values of ω_m and ω_o. As it will be discussed in section 4.2.2, this is due to the smaller area and the smaller 'side length'. Nevertheless, the ω_m and ω_o dependence on the system parameters is the same in both cases. Therefore, due to the simplicity of the corresponding calculation, square SRRs were used in our studies.In this single ring resonator the inductance is provided by its circular or square metallic loop, while the capacitance is given by the gap (cut) of the ring. The second dip in the transmission of Figure 4.1(a), at $\omega = \omega_o$ (≈70 GHz for the tetragonal ring) corresponds to the electric cut-wire-like response of the SRR [51], i.e. to a resonance in its electrical permittivity, ε.

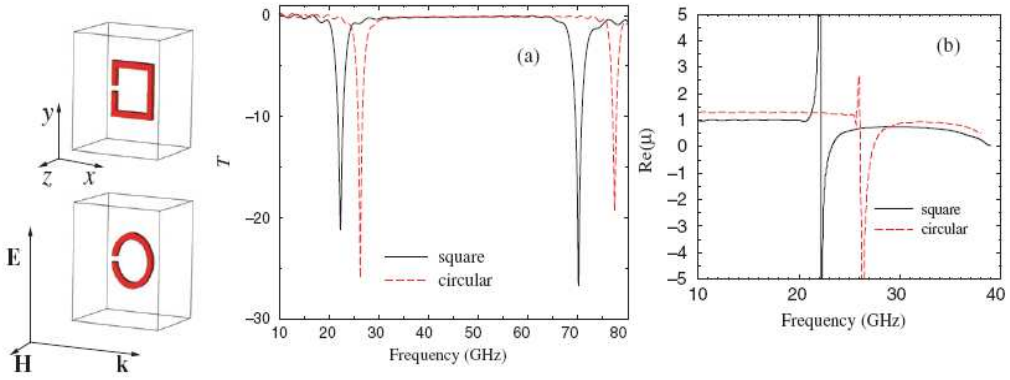

Figure 4.1: (a) Transmission (T, in dB) versus frequency for one single-ring square (solid curve) and a circular (dashed curve) SRR. The corresponding designs are shown on the left side of the panel. For the square SRR the ring width, depth and the gap all are 0.2 mm, and the linear SRR size is 1.8 mm. The SRR is placed in air, in a computational cell with dimensions 3.8 × 3.8 × 3.2 mm^3, along x, y and z directions, respectively. The boundary conditions are $E_{\parallel} = 0$ at $y = 0$ and 3.8mm, and $H_{\parallel} = 0$ at $z = 0$ and 3.2mm (at the boundaries of the computational cell). The circular SRR has outer diameter 1.8 mm and the computational cell and the materials characteristics are like those for the square one. The external field propagation direction and polarization are shown together with the SRR designs. (b) Magnetic permeability, $\mu(\omega)$, as a function of frequency for the single-ring square (solid curve) and circular (dashed curve) SRR, at frequencies around the magnetic resonance frequency.

4.2.2 Controlling ω_m and ω_o for one single-ring SRR

In the LHMs studies, one of our goal is to shift the magnetic resonance frequency, ω_m, below the cut-off frequency (ω_p'), i.e. in the $\varepsilon < 0$ regime of the electric response of the combined system of SRRs and wires. The cut-off frequency ω_p' depends strongly on the electric cut-wire response of the SRR. So considering the fact that there is a requirement of $\omega_m < \omega_p'$, it is very important to be able to control both the magnetic and the electric SRR resonance frequencies, ω_m and ω_o respectively. In order to control these resonance frequencies, a better understanding of the dependence of the ω_m and ω_o on the various

SRR parameters is needed. So their dependence on the SRR size and more specifically on the SRR area and side length (see Figure 4.2) is investigated as a first step.

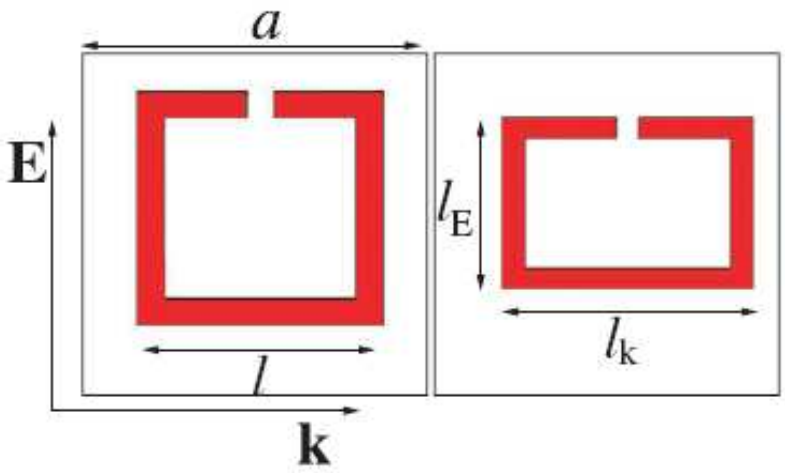

Figure 4.2: Two single-ring SRRs, a square one and an orthogonal one, are shown, together with the external electric field, E, polarization and propagation direction and the lattice constant, a, of the square unit cell. For the orthogonal SRR (with identical lattice, electric field polarization and propagation direction) the lengths, l_k and l_E, of the two sides are also shown.

The ω_m and ω_o dependence on the SRR area for a square SRR is shown in Figure 4.3(a). Here, ω_m and ω_o are plotted as a function of a/l, where l is the side length of the SRR (see Figure 4.2) and a is the size of the unit cell or the lattice constant at the SRR plane (see again Figure 4.2). It can be seen from Figure 4.3(a) that for a single-ring square SRR $\omega_m \sim 1/l$, thus, ω_m^2 is inversely proportional to l^2, which is the SRR area. This is in agreement with the well accepted formula $\omega_m^2 \sim 1/LC$. It should be noted that the self inductance, L, in this formula is approximately proportional to the area of the SRR loop. The electric resonance, ω_o, also increases as a/l increases. However, its dependence is weaker than that of ω_m. The different dependences of ω_m and ω_o on a/l allows us to control the relative position of ω_m and ω_o This is something that can be proved to be of great power in the study of left-handed materials.

Other than the studies mentioned above, this time, the side of the SRR (l_k in Figure 4.2) which is perpendicular to the incident electric field direction is varied keeping l_E constant. Then ω_m and ω_o are calculated to investigate the effect of this change. The effect of this change, i.e. the dependence of ω_m and ω_o on a/l_k is shown in Figure 4.3(b). It can be seen from Figures 4.3(a) and (b) that ω_o, for a single ring SRR, depends only on its side parallel to the electric field, following the approximate relation $\omega_o \sim a/\sqrt{l_E}$, with a being the corresponding lattice constant. This is the reason that ω_o is constant in Figure 4.3(b), while $\omega_o \sim a/\sqrt{l}$ in Figure 4.3(a).

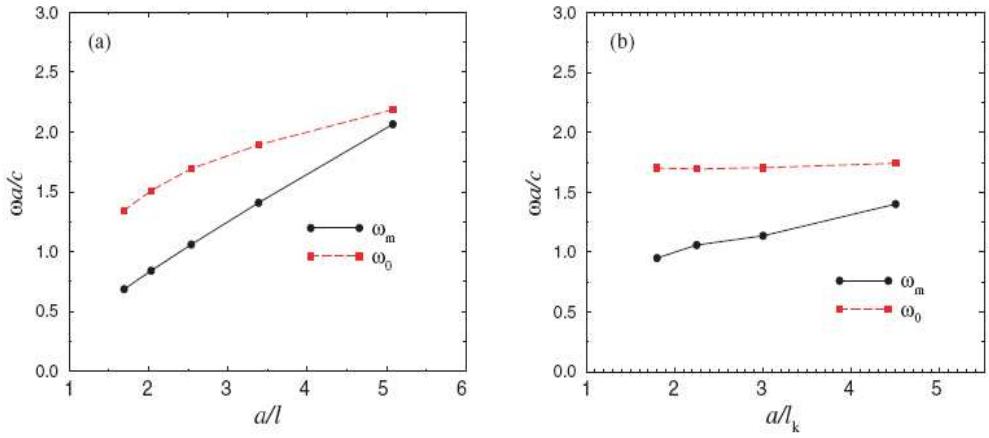

Figure 4.3: (a) ω_m and ω_o (in units of c/a, where c is the vacuum light velocity and a is the lattice constant of the square unit cell) versus a/l for a square single-ring SRR like the one shown in the left panel of figure 4.2. l is the SRR side length. (b) ω_m and ω_o (in units of c/a) versus a/l_k for an orthogonal single-ring SRR (see figure 4.2, right panel). l_k is the length of the SRR side which is perpendicular to the incident electric field, E.

4.2.3 Single versus double ring SRRs

In composite metamaterial studies, double ring SRRs have been used widely so far. But it is a well known fact that a single ring also acts as a magnetic resonator, providing a negative μ regime. So in this section, single and double ring SRRs will be compared and the benefits from the addition of a second ring will be investigated. The model presented in Figure 4.4 will be used in our investigations.

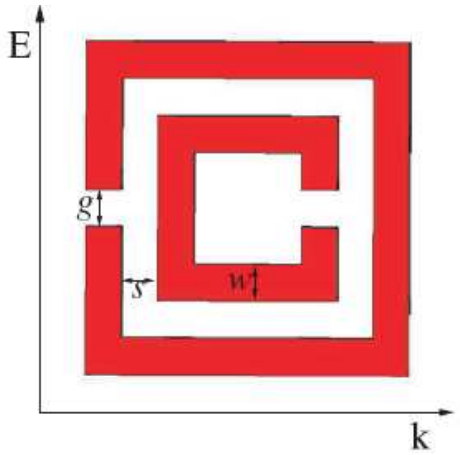

Figure 4.4: Our model double-ring SRR. $g = s = w = 0.2$ mm; metal depth = 0.2 mm. The SRR side is 1.8 mm. The computational cell and the boundary conditions used in the calculations are the same as those described under Figure 4.1.

The transmission through the double ring SRR of Figure 4.4 is presented in Figure 4.5(a). The transmission through only its outer or its inner ring SRR is presented in Figure 4.5(b). The electromagnetic field propagation direction and polarization are as shown in Figure 4.4. The transmission has been calculated using MWS and considering only one SRR in the propagation direction. From Figures 4.5(a) and (b), it can be seen that the lower magnetic resonance frequency of the double ring (see the first dip in Figure 4.5(a)) is essentially that of the outer ring, but with a relatively small downwards shift. Detailed studies of the field and current distribution showed that in the double ring case the currents at the first resonance move in the same direction in both rings. As a result of this, there are opposite charges at the facing sides of the outer and inner ring. So it can be said that a capacitor is formed between the rings and this capacitance is added to that given by the gap of the outer ring, which leads to a decrease in the resonance frequency with respect to that of just the outer ring.

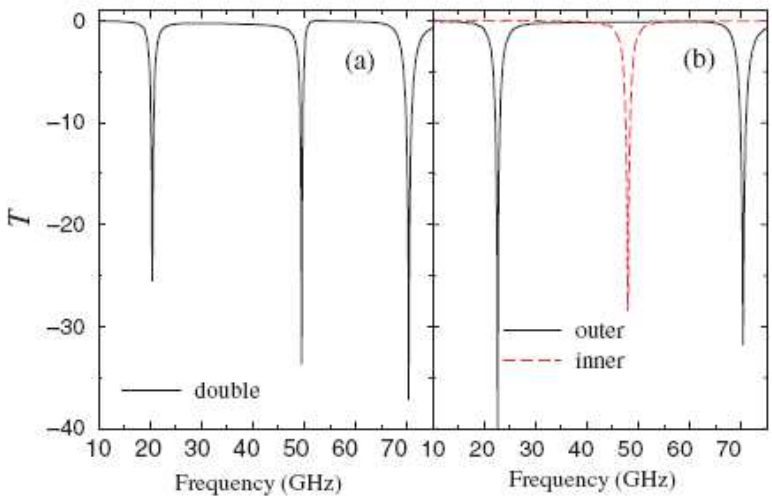

Figure 4.5: Transmission (T, in dB) versus frequency (in GHz) for the double-ring SRR shown in figure 4.4(a), and for its isolated outer and inner ring SRRs (b). The background material is air.

The second dip of the double-ring case corresponds essentially to the magnetic resonance of the inner ring, with a small upwards shift (there, the currents in the two rings of the SRR move in opposite directions). The strength of this resonance is sometimes very small, showing that the magnetic response of the inner ring is screened by the presence of the outer one. This happens mainly in the cases where the electric field is parallel to the continuous sides of the SRR.

Another important characteristic of the double ring is that it contains in its spectrum also the electric responses of its two component rings; see, e.g., the third dip of Figure 4.5(a), which corresponds to the electric cut-wire response of the outer ring (of its longer side).

One advantage of the double-ring SRR, compared with its outer single-ring resonator, as can be seen from Figure 4.5, is that the magnetic resonance of the double ring occurs at a relatively lower frequency; thus there is a higher probability for the magnetic response to lie in the $\varepsilon < 0$ regime of the combined system of SRRs and wires. Another advantage of the double-ring SRR appears when we put the rings in a periodic

arrangement: the array of double-ring SRRs possesses a stronger magnetic resonance, which might lead to a more robust LH peak for the combined system of SRRs and wires.

4.2.4 The dependence of ω_m on the system parameters for a double ring SRR

In order to understand the behaviour of the magnetic resonance frequency ω_m of a double ring, its dependence on various system parameters is investigated. In this section we present the dependence of ω_m on the dielectric constant of the board, on the width, separation and depth of the rings, as well as on the gaps (cuts) of the rings. The SRR presented in Figure 4.4.is used as a model system for this study.

4.2.4.1 The influence of the board dielectric constant

The transmission (T) as a function of frequency for the resonator described in Figure 4.4 is shown in Figure 4.6(a). This resonator is embedded inside a background (board) material with dielectric constant ε_b= 12.3 (corresponding to GaAs). The T for ε_b = 1 is shown in Figure 4.5(a). If we compare Figure 4.6(a) with Figure 4.5(a), it can be seen that as a result of the increase of the dielectric constant of the background there are reductions of both the electric and the magnetic resonance frequencies of the SRR. Detailed quantitative analysis showed that the dependence of ω_m on ε_b is of the form $\omega_m^2 \sim 1/\varepsilon_b$.

The interesting point here is that ω_m depends not on the average ε_b in the unit cell but on the local values of ε_b nearby the SRR, and especially close to the gaps of the rings (although we are in the low frequency regime, where average values should be adequate for representing any spatially modulated dielectric properties of the board). This is demonstrated in figure 4.6(b). Here, the T is demonstrated for the case where the background material consists of a thin GaAs slab and the rest is air (the GaAs slab covers only 6.25% of the unit cell—its thickness is 0.2 mm). In figure 4.6(b), the solid curve shows the T when the SRR is printed on the GaAs slab and the dashed curve shows the one when the SRR is moved 0.2 mm away from this slab. Neither of the two cases can be deduced from figure 4.5(a) using the relation $\omega_m^2 \sim 1/\varepsilon_b$, with ε_b an average value. The

same amount of dielectric in the unit cell affects the transmission differently depending on its position. This can be explained by taking into account the strong inhomogeneity and the local spatial character of the field in the system, especially at the resonance frequencies. At the magnetic resonance, the electric field has its maximum mainly at the SRR outer ring gap and in the region between the rings, while along the direction perpendicular to the SRR plane it is not very much extended (see figure 4.7). Taking into account this form of the field as well as the strong influence of the dielectric constant on the capacitance, it is not difficult to understand the different influences of the dielectric at the different positions of the unit cell. It should be noted that on changing the dielectric constant of the total background material the *T* spectrum is moved to different frequencies but its form remains unchanged, i.e. all the characteristic frequencies depend in the same way on the background dielectric constant. But this is not valid if the background material is not homogeneous.

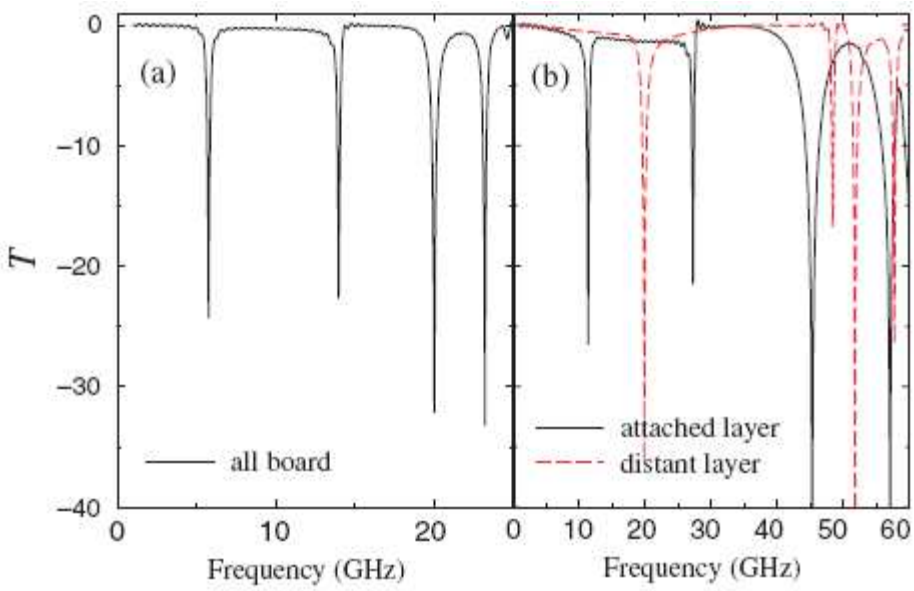

Figure 4.6: (a) Transmission (T), in dB, as a function of frequency for the resonator of figure 4.4. The background material has a dielectric constant ε_b = 12.3. (b) T versus frequency for the resonator of figure 4.4, but the background material is composed of air plus a slab of dielectric, of ε = 12.3 and dimensions 3.8 × 3.8 × 0.2 mm^3 (3.8×3.8 is the size at the SRR plane). The solid curve shows the T if the SRR is attached on the dielectric slab and the dashed curve shows the T if the SRR is 0.2 mm away from the slab.

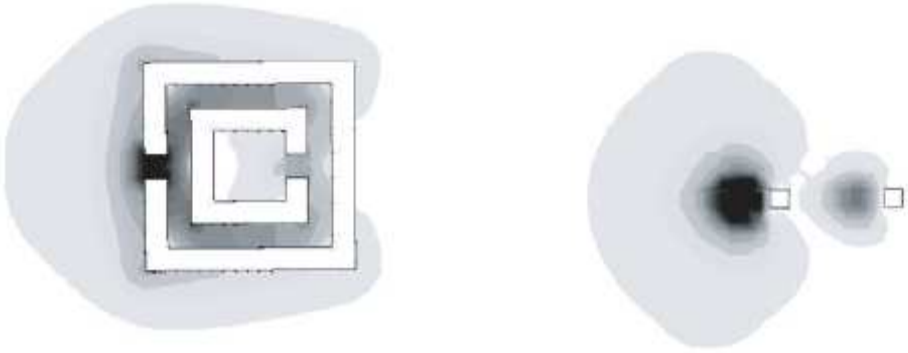

Figure 4.7: The electric field intensity (E^2) for the SRR of figure 4.4, at the magnetic resonance frequency. The left panel shows the field at the SRR plane and the right panel the field at a plane perpendicular to that of the SRR, which passes through the SRR gaps.

4.2.4.1 The influence of the width, separation and thickness of the rings

The capacitance between the rings depends on the ring separation and it is a component of the total capacitance of the SRR. So it can be expected that the magnetic resonance frequency depends also on the ring separation, s.

This dependence is shown in Figure 4.8(a): reduction of s results in a decrease of the magnetic resonance frequency (see the shift of the first T dip in Figure 4.8(a)). This is expected, as reduction of s is equivalent to increase of the inter-ring capacitance (note that $\omega_m \sim 1/\sqrt{LC}$ and for a parallel plane capacitor with separation of plates s, $C \sim 1/s$). From Figure 4.8(a) it can be seen that a 50% reduction of s results in an almost 13% downshift in ω_m.

Figure 4.8(b) shows how the transmission is affected by the ring width (w), as well as the combined influence of the change of both the width and separation of the rings. Ring width affects the inductance, L, of the loops: smaller width means larger inductance and thus smaller ω_m. Figure 4.8(b) indicates that a 50% reduction of w results in an almost 15% downshift of ω_m.

Changing both the ring separation and their width, the shift in ω_m of the first resonance is approximately the sum of the two shifts coming from the separate changes of w and s.

Here, it should be noted that in all the cases of Figure 4.8 where downshift of ω_m takes place, this shift is accompanied by a reduction of the strength of the resonance. Thus, although the desired condition for ω_m is to be as low as possible, special attention must be paid that the lowering of ω_m is not associated with a weakening of the magnetic response of the SRR.

Regarding the influence of the depth of the rings on the magnetic resonance frequency, it seems that this is insignificant provided that the depth of the rings is a few times larger than the skin depth of the metal at the frequency regime of interest.

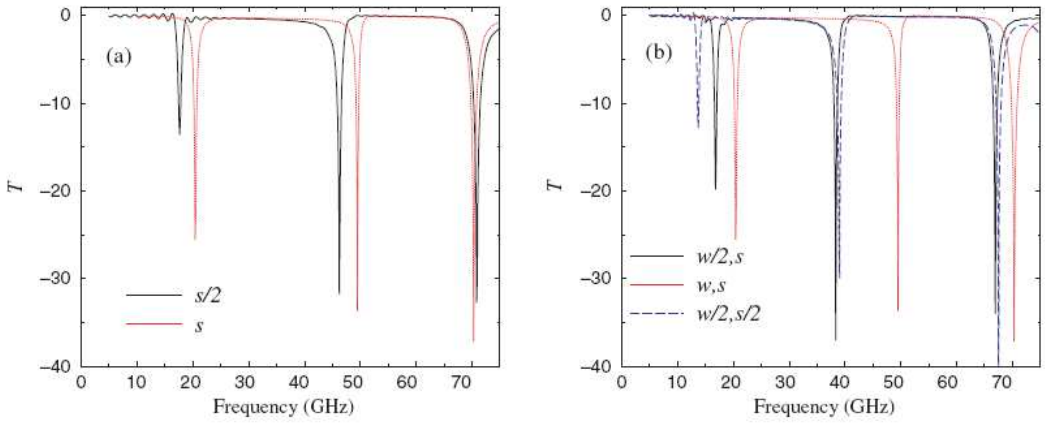

Figure 4.8: (a) Transmission (T), in dB, versus frequency for the SRR of Figure 4.4 (dotted curve), where s = 0.2 mm, and for a SRR arising from that of Figure 4.4 by reducing s to 0.1 mm (increasing the inner ring size). The background material is air. (b) The dotted curve is the same transmission as in (a) (s = 0.2 mm, w = 0.2 mm), the solid curve shows the T for ring width w = 0.1 mm and separation s = 0.2 mm and the dashed curve the T for $s = w$ = 0.1 mm.

4.2.4.3 The influence of the gaps (cuts) of the rings

The influence of the size (g) of the gaps of the rings is illustrated in figure 4.9. On reducing the gap size, ω_m is reduced. The influence of the gap size in ω_m seems, though, to be smaller than the influence of the ring separation.

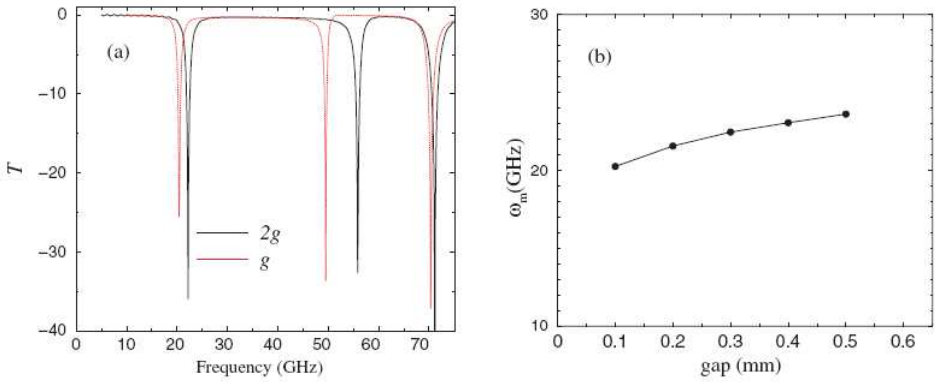

Figure 4.9: (a) Transmission coefficient (T), in dB, versus frequency for the SRR of Figure 4.4 (dotted curve; SRR gap size g = 0.2 mm) and for the same type of SRR but with gap size g = 0.4 mm (solid curve). (b) The dependence of the magnetic resonance frequency, ω_m, on the size of the SRR gaps is shown. The background material is everywhere air.

4.3 SRR orientation relative to the electromagnetic field: second electric coupling

In one-dimensional (1D) LH materials there are two possibilities for the SRR orientation: either the one shown in Figure 4.4, i.e. the electric field, **E**, parallel to the SRR sides bearing the cuts, or its 90◦ rotated case, i.e. **E** perpendicular to these sides. These two geometries are those marked (B) and (A) in the left panel of Figure 4.10.

The transmission for these two geometries as a function of frequency is shown in the right panel of Figure 4.10. What can be seen there is that the lower magnetic resonance frequencies of the SRR are almost the same in the two orientations. What is changed is

the frequency of the electric cut-wire response (see the third dip of each curve-at ~58GHz and ~70GHz), which is higher for the geometry (B).

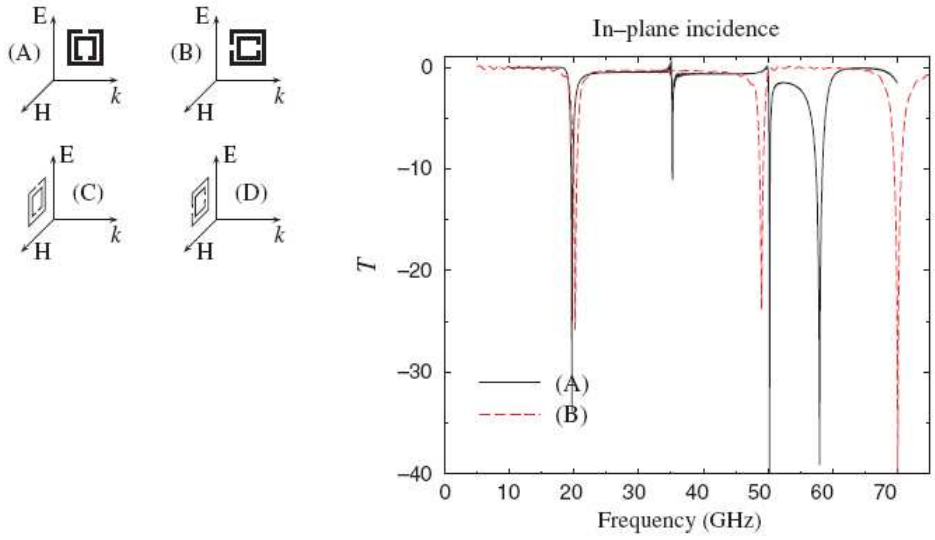

Figure 4.10: Left panel: the four possible orientations of the SRR relative to the electromagnetic (EM) field propagation direction and polarization. Right panel: transmission coefficient (T , in dB) versus frequency for an SRR with the parameters those of figure 4.4, oriented with respect to the EM field as in configuration (A) (solid curve) and as in (B) (dashed curve). (A) and (B) are shown in the left panel.

Examining periodic systems of SRRs, where due to the interactions among the SRRs the transmission dips become broader, it was found that the T dip corresponding to the magnetic resonance frequency is broader and deeper for the geometry (B). This broader dip, though, was not associated with a broader LH peak when the SRRs are combined with wires. The LH peak for the case (B) was rather narrower and weaker. This was a puzzling result in the beginning. The issue was resolved during the studies related with two-dimensional (2D) and three dimensional (3D) materials, where for the orientation of the SRR relative to the EM field two additional possibilities are involved, those marked (C) and (D) in Figure 4.10. These two orientations should be magnetically inactive, as the incident magnetic field is in the plane of the SRR, and thus unable to excite resonant circulating currents around the SRR rings.

Surprisingly, studying the orientation (D), we found [28] a dip at the magnetic response frequency of the SRR (see Figure 4.11). Similar results were obtained also by Gay-Balmaz *et al* [72]. This dip is again due to resonant currents circulating around SRR rings. There a question appeared. How are these circulating currents excited, since it cannot be through the external magnetic field? First it was found that they are excited through the external electric field. The possibility of coupling with the electric field is given by the asymmetry of the SRR with respect to this electric field (see Chapter 3, section 3.3).

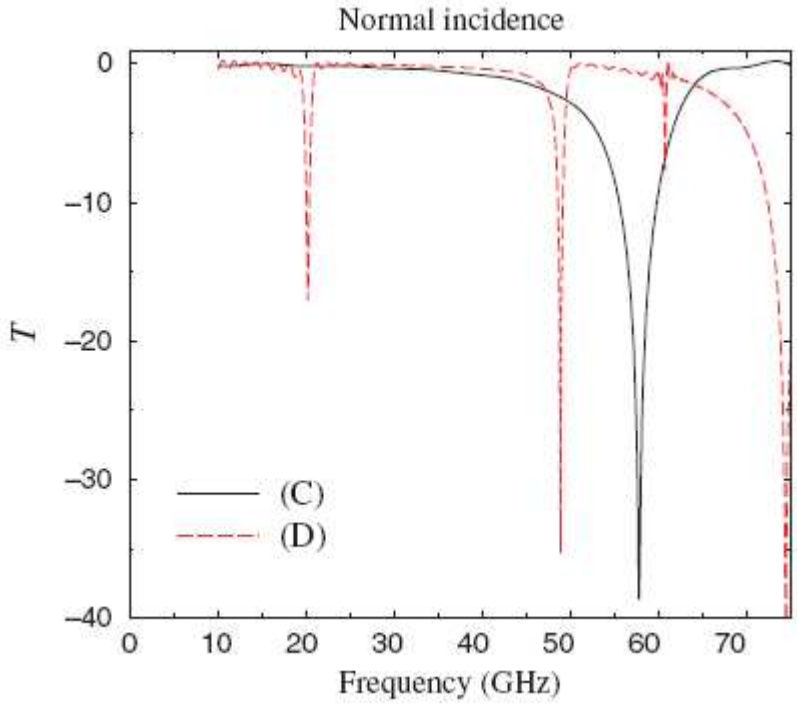

Figure 4.11: Left panel: transmission coefficient (T , in dB) versus frequency for an SRR with the parameters those of Figure 4.4, oriented with respect to the EM field as in configurations (C) (solid curve) and (D) (dashed curve)

As shown in Figure 4.11, for the configuration in Figure 4.10 (D), the asymmetry of the SRR with respect to the external **E** leads to a charge distribution asymmetry, which is compensated through a circular current. Thus, not only the magnetic field but also the electric field of the incoming wave can couple to the resonance of the circulating currents in the SRR. As it was also mentioned in Chapter 3(section 3.3), the most important effect

of this coupling, which will be called here second electric coupling (to be distinguished from the electric coupling through the cut-wire-like resonance, at ω_o), is an electric resonant response (a resonance in ε) around the SRR magnetic response frequency, ω_m. Detailed studies showed that this electric response, which comes from the non-zero average electric polarization of the (asymmetric) SRR, occurs in fact at a frequency slightly shifted from ω_m (slightly above ω_m in most of the cases studied). A possible result of this resonant ε is the addition of a right-handed transmission peak close to ω_m when the SRRs are combined with wires, which peak may diminish or even destroy the LH behaviour.

It should also be noted that the asymmetry as a result of which we have the second electric coupling is present also in the configuration (B) of Figure 4.10. This might be the reason for the broader—than that of (A)—magnetic dip in the periodic SRR system, which is not associated with a broader LH peak of the combined system of SRRs and wires. The problem of the asymmetry-mediated electric coupling will be present in all higher dimensional LHMs apart from some special cases which only work for a particular orientation or a constrained direction of propagation. The most secure solution of the problem is the invention and employment of more symmetric SRR designs which will be presented in the following sections.

4.4 Parametric studies of LH materials

In this section, the results of a parametric study of LH materials will be presented. This study was done using model systems with parameters close to those of LH structures which can be or have been constructed experimentally.

Throughout this study the influence of several parameters on the LH regime (on the LH transmission window and the maximum transmitted power) is investigated. Those parameters are as follows:

(i) the board dielectric constant, ε_b;

(ii) the position of the wires relative to the SRRs;

(iii) the thickness of the unit cell; and

(iv) the loss parameter of the boards, ε_b''.

The aim of this study is to give the optimum parameters for obtaining a true broad LH transmission band with large transmitted power. This study plays an important role and will be very useful for designing the next generation of LHM experiments.

The structures studied in this study are made up of a tetragonal, double-ring SRRs and continuous wires, patterned on thin dielectric boards which are separated by air.

4.4.1 The influence of the board dielectric constant

Studies concerning the dependence of the LH peak on the dielectric constant of the board, ε_b, showed that ε_b influences only the position of the LH peak, leaving its height and width almost unaffected (for lossless boards). The dependence of the LH peak position on ε_b follows the dependence of the magnetic resonance. As it is discussed in the Section 4.2.5, on increasing ε_b the LH peak is moved to lower frequencies, with the peak frequency inversely proportional to the square root of ε_b.

4.4.2 The influence of the position of the wires relative to the SRRs.

For examining the influence of the relative SRR wires position, the wires parallel to the imaginary line connecting the cuts of the SRR rings are considered. The configurations shown in Figure 4.12(a) are examined.

It was found that the optimum position of the wires is that of configuration (B) of Figure 4.12(a), i.e. the wires attached at the back of the dielectric boards, just behind the cuts of the rings. Although it is easier to fabricate configuration (A) experimentally [6], it gives a narrower and somehow lower LH peak (see figure 4.12(b)). Thus, configuration (B) is optimum for the LH transmission.

Investigating the effect of moving the wire paralel to itself along the **H** direction for the configuration (B), it was found that for cubic unit cells the distance of the wire from the resonator plane does not influence the LH peak very much.

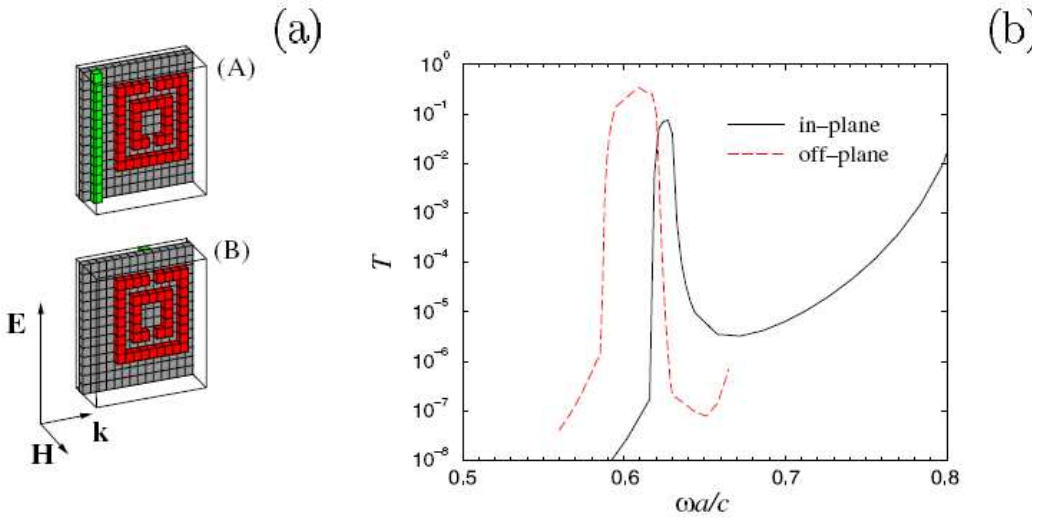

Figure 4.12: (b) Transmission coefficient (*T*, in dB) versus dimensionless frequency for the structures shown in the left panel, (a). The solid curve shows the *T* for configuration (A), i.e. wires next to the SRRs, and the dashed curve that for configuration (B), i.e. wires at the back of the board. The board is a thin dielectric layer (thickness = *a*/14) of dielectric constant ε_b = 12.3. The rest of the background material is air. The unit cell is a cube, with lattice constant *a*; the SRR has outer side length 9*a*/14 and its other characteristic lengths are *a*/14. The wire has a cross-section at the H–k plane of *(a*/14*)* × *(a*/14*)*.

4.4.3 The influence of the unit cell thickness (the lattice constant along the direction perpendicular to the SRR plane)

In Figure 4.13, the evolution of the LH transmission peak of Figure 4.12(b), configuration (B), is presented, as one changes the unit cell thickness, *a*H (i.e. the distance of two successive SRR + wire planes along the **H** direction -see Figure 4.12(a)). It can be

noticed that as the successive SRR + wire planes come closer, the LH peak becomes much broader. The reason is the broadening of the negative μ regime due to the increasing amplitude of the magnetic resonance of the approaching SRRs, i.e. due to the stronger interaction among the SRR magnetic resonances. Moreover, as a result of the reduction of the unit cell size in the continuous wire lattice, there is an increase of the cut-off (plasma) frequency, ω_p, of the wires and thus an increase of the cut-off frequency, ω_p', of the combined SRRs + wires system. Thus the LH peaks become more clearly resolved and separated from the neighbouring right-handed *T* shoulders.

4.4.4 The influence of the loss parameter (conductivity or ε''_b) of the dielectric boards

The ε_b'' (imaginary part of the dielectric constant) of the boards was proved to be one of the most critical parameters [54, 66, 70] for the left-handed transmission. An example of its influence is shown in Figure 4.14. It can be seen that even small ε_b'' values can lead to a very large *T* reduction. This parameter is critical even if the dielectric boards are very thin, since, especially for high index boards, there is a high concentration of field inside the boards.

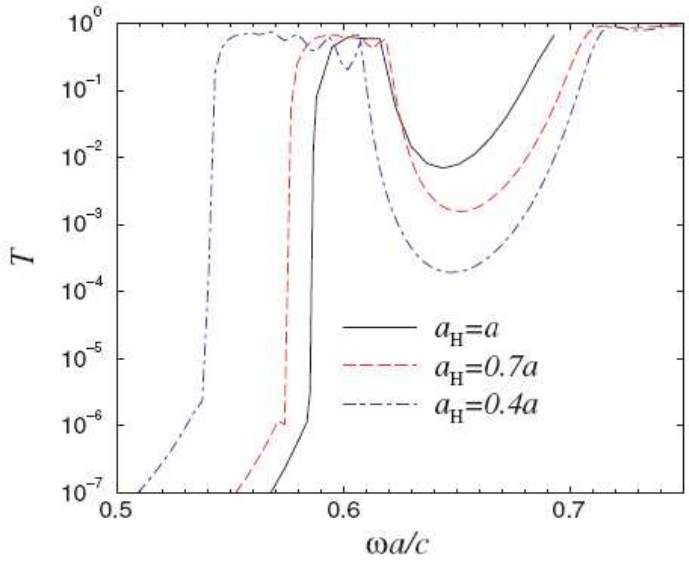

Figure 4.13: Transmission coefficient (T) versus dimensionless frequency for the geometry (B) of Figure 4.12, for three different unit cell sizes, a_H, in the direction perpendicular to the SRR plane. The other parameters are those mentioned in Figure 4.12. $a = a_E = a_k$ is the lattice constant (unit cell size) in the plane of the SRR.

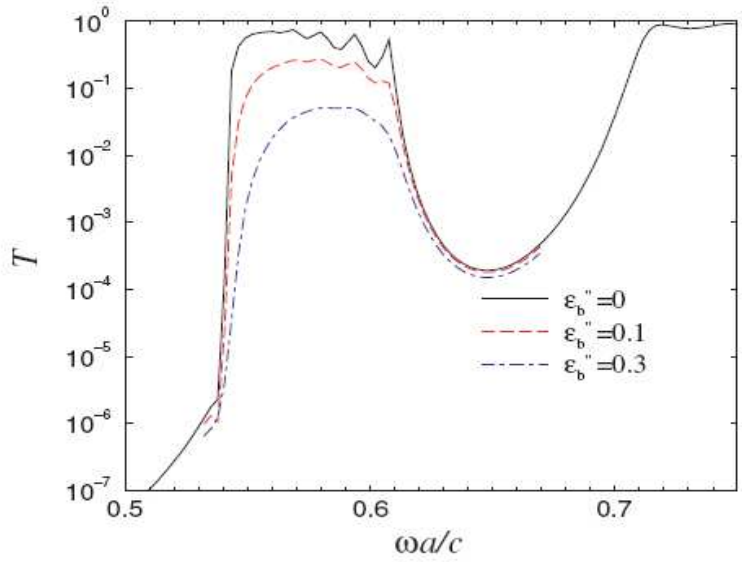

Figure 4.14: The evolution of the transmission coefficient (T) of Figure 4.13, dotted–dashed curve, as one adds to the dielectric constant of the board an imaginary part, ε_b''. The horizontal axis is a dimensionless frequency, normalized with the unit cell size at the SRR plane, a, and with the vacuum light velocity, c.

4.5. The combined metamaterial electric cut-off frequency, ω_p'

It was recently recognized [51] that the electric response of the LHMs is not due only to the electric response of the metallic wires; it is also strongly affected by the electric response of the SRRs. The SRRs respond electrically like a system of cut wires, exhibiting a resonance at a frequency ω_o. (This response can be demonstrated by closing the SRRs, destroying thus their magnetic response.)

As a result of the presence of the SRRs, the electric cutoff frequency, ω_p', of the combined system of wires and SRRs (or closed SRRs) is always lower [30, 50] than the cut-off (plasma) frequency of the continuous wires alone (ω_p). The role of the SRRs in the formation of the electric response of the combined system of SRRs and wires is illustrated in Figure 4.15.

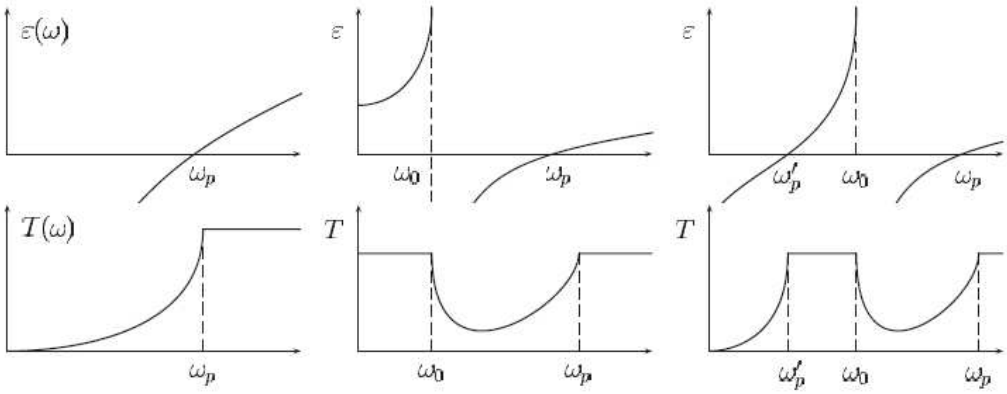

Figure 4.15: An illustration of the electric response to an incident EM field of a system of continuous wires (left panels), of cut wires (or SRRs or closed SRRs) (middle panels) and of the metamaterials of wires plus cut wires or SRRs (right panels). Both the electrical permittivity ε(top panels) and the resulting transmission coefficient T (bottom panels) as a function of frequency are shown, and the characteristic frequencies, ω_p, ω_o and ω_p', of these systems are marked. It is shown that the combination of a system of continuous wires with a system of cut wires (or SRRs) results in a spectrum with remarkable differences compared to that for the system of continuous wires only.

The dependence of the cut-off frequency ω_p' on (i) the depth and width of the continuous wires, (ii) the thickness and width of the SRR rings will be discussed in the following sections.

4.5.1 The influence of the thickness and width of the continuous wires

It is clear from the previous discussion (and from Figure 4.15) that ω_p' can be increased through increase of ω_p of the continuous wires, although it would remain lower than ω_o. Our studies showed that ω_p of the wires increases as the width of the metallic wires increases. Calculations of the transmission coefficient through the combined system of closed SRRs and wires showed that ω_p' also increases as the width of the metallic wires increases, but the increase depends also on the relative position and distance of ω_p and ω_o.

The thickness of the wires has an effect similar to that of the width on ω_p: increasing the thickness leads to increase of both ω_p and ω_p'

4.5.2 The influence of the thickness and width of the SRR rings

Detailed transmission studies showed that the width of the SRR rings has almost no effect on ω_p'. The same is true also for the metal thickness of the SRR. This is of great importance as the thickness and width of the SRRs have considerable effects on ω_m. Thus, since ω_m is controlled only by the SRRs while ω_p' is controlled also by the wires, the electric and magnetic responses of the LHMs can be controlled independently.

4.6. Symmetric SRR structures

The general problem with the rings of only one gap (cut) in the SRR designs considered so far is the inherent asymmetry of the resulting SRRs. As discussed in Section 4.3, this will lead to the occurrence of the electric coupling to and response from the magnetic resonances (EEMR) [28] .This is an unwanted feature for fabricating higher dimensional systems. Marques *et al* considered bianisotropy in SRR structures and developed an analytical model for evaluating the magnitude of cross-polarization effects [59].

To avoid this EEMR, more symmetric SRRs should be used. The idea in the design of more symmetric SRRs is to keep the inductance provided by the loop of the SRR ring but to distribute the capacitance of the single gap to two or four gaps, symmetrically around the ring, as shown in Figure 4.16. This will lift the asymmetry of the SRR plane and therefore eliminate EEMR.

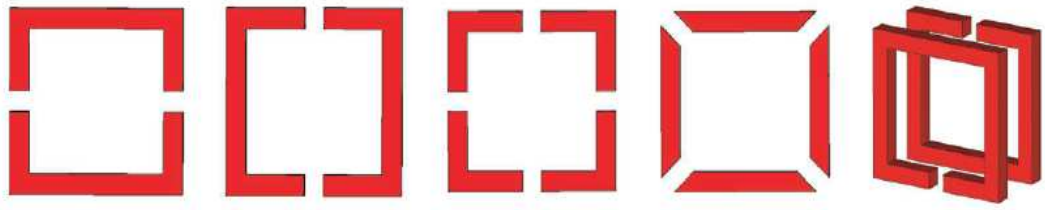

Figure 4.16: Five SRR designs, more symmetric than the conventional and most commonly used SRR presented in Figure 4.4. The advantage of these symmetrized SRRs is the avoidance of the electric excitation of the magnetic resonance, described in Chapter 3. The disadvantage is the higher magnetic resonance frequency, due to the many gaps (cuts).

The problem arising in this kind of design is the difficulty of maintaining the capacitance of the single-gap ring, as the gaps act like capacitors in series, leading to a considerable lowering of the total capacitance and thus to an increase of ω_m. (The magnetic frequency for a ring with n gaps equal in size goes as ω^2_m (n gaps) ~ $n\ \omega^2_m$ (1gap).) This is a disadvantage of the design as it decreases the probability of ω_m lying below the cut-off frequency of the electric response of the system.

One solution to the problem could be a decrease in the size of the gaps, although this, in many cases, is limited by technology. Another solution could be a modification in the designs, with the capacitance of the gaps being increased. Such modifications for two of the structures of Figure 4.16 are shown in Figure 4.17. The result from such a modification is usually a lowering of ω_m but not always an improvement in the transmission picture, as the strength of the magnetic resonance and the width of the $\mu < 0$ regime are affected as well.

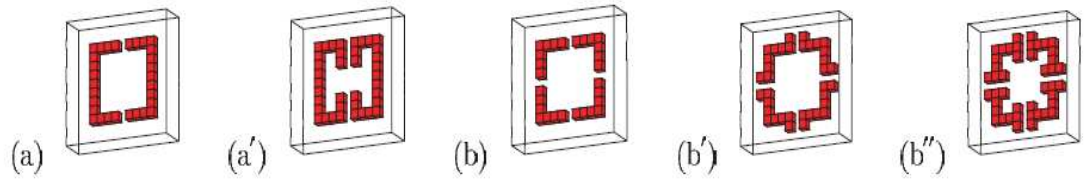

Figure 4.17: Modifications, (a') and (b'), (b''), of two of the SRR designs presented in Figure 4.16. These modifications result in lower magnetic resonance frequency compared with their original SRRs, (a) and (b).

Four of the most promising SRR designs which emerged from our studies on more symmetric SRRs are shown in Figure 4.18.

As a conclusion, the magnetic and the electric response of single-ring and double-ring SRRs, both circular and rectangular are investigated. The dependence of the magnetic resonance frequency, ω_m, and of the electric resonance frequency, ω_o, of the SRR on the length, width and thickness of the metallic sides for different kinds (circular or square, single- or double-ring) of SRRs was examined. It was found that both ω_m and ω_o for circular and rectangular SRRs are qualitatively the same and therefore most of our studies were done for rectangular SRRs because of the simplicity of the corresponding transmission calculations.

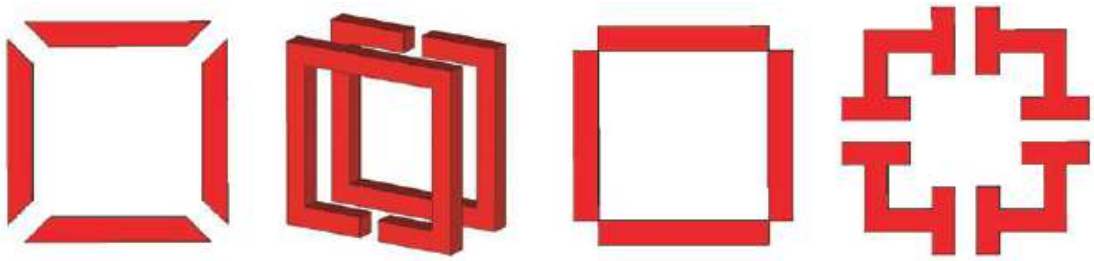

Figure 4.18: Four of the most promising ‘symmetric’ SRR designs.

The transmission characteristics of LH structures composed of square SRRs and wires were also studied. The dependence of the LH transmission peak on the real (ε_b) and imaginary (ε_b'') parts of the dielectric constant of the dielectric boards was examined. ε_b'' was proved to be one of the most critical parameters for the LH transmission, as even a small change of it can lead to a very large reduction of the LH transmission peak.

Among the possible configurations of SRRs and wires that were examined, the best for producing the most robust LH transmission peak was found to be the one that has square SRRs on one side of the dielectric board and wires on the other side of the board, just behind the cuts of the rings of the SRRs. The dependence of the LH transmission peak on the unit cell thickness and on the distance between the SRRs and the wires for this configuration were also examined.

Moreover, the role of the SRR orientation relative to the incident EM field and the resulting issue of the electric coupling to the magnetic resonance (the coupling of the external electric field to the resonance of the currents circulating around SRRs) were investigated. This coupling, which represents an unwanted feature as it is associated with a resonance in the electric response of the system, is a result of lack of symmetry and will always be present in 2D and 3D LH structures composed of non-symmetric SRRs. In the attempts to avoid this coupling highly symmetric SRR structures and their behaviour in 2D and 3D LH media were examined. Some optimum designs, which may constitute components of promising 2D and 3D LH structures were identified.

Chapter 5

Composite Metamaterials operating in the THz Frequency Regime

5.1 Introduction

We have already discussed the unique physical properties of the left-handed materials and how to build a LH material in our previous chapters. Since the first experimental demonstration of LHMs by Smith et al. [7], there has been a great effort to push upwards the frequency range at which negative μ and/or LH behavior occur, from the GHz range to the infrared and optical regime. As discussed in Chapter 2, the natural course of the development of the LHM field has been from the microwave towards the THz and optical frequencies [19, 21-23, 29, 73]. Similarly, we also have begun our studies on large scale structures designed for the microwave regime in order to quickly develop a better understanding of the physics and LH behaviour of metamaterials. Subsequently, we have shifted our designs to smaller geometries that work at the THz frequency regime.

In this chapter, first we will present the structures which are designed to operate in the THz frequency regime. Starting with the split ring resonators, mutli-gap split ring resonators and cut and continuous wire pair designs will be introduced. Then, the

transmission and reflection simulations of the designed structures will be shown accompanied by their retrieval results. After a brief summary of the fabrication process, we will present the experimental results which are in good agreement with the simulations and the retrieval.

5.2 The Fabrication, Simulation and the Experiments of Designed structures

At the THz and the optical frequencies the freedom to manipulate the geometry of the structures is quite limited. So, although we investigated the magnetic resonance of split ring resonators (SRRs) which operates at THz frequencies as a start, we studied the cut and continuous wire slab pairs to simplify the fabrication and characterization of negative μ and/or LH metamaterials.

5.2.1 Split-ring resonators operating at THz frequencies

We had discussed the transmission and reflection properties of the SRRs as well as their magnetic resonance in the previous chapters. It was mentioned that besides the magnetic field normal to the SRR plane, an electric field parallel to the gap-bearing sides of the SRR [see the orientations of Figs. 5.1(b) and 5.1(d)] can couple to the SRR [72]. This excites the oscillating resonant current around it and causes the electric excitation of the magnetic resonance (EEMR) effect.

The EEMR effect provides new opportunities for characterization of the SRR since it seems to allow excitation of the magnetic resonance for propagation even normal to the SRR plane. Numerical calculations of the effective permittivity and permeability of a metamaterial consisting of SRRs structured on a nanometric scale had been presented [74]. They showed that metallic resonators could provide a means to obtain a negative effective permeability at up to telecommunications wavelengths. Moreover, Yen *et al.*

showed [29] that SRRs could indeed exhibit a magnetic response at terahertz frequencies. They performed ellipsometry measurements at 30° for one SRR layer and observed a resonant peak, centered at 1.25 THz, in the ratio of reflectances of the two possible magnetic field polarizations, which they attributed to the magnetic response of the constituent SRRs. Linden *et al. [24]* demonstrated experimentally a magnetic resonance response of a SRRs system at 100 THz.

All the systems mentioned above were composed of only one layer of SRRs. We managed to fabricate, for what is to our knowledge the first time, a micrometer-scale metamaterial consisting of five layers of single-ring SRRs (a photograph is shown in Fig. 5.1) which operates around 6 THz.

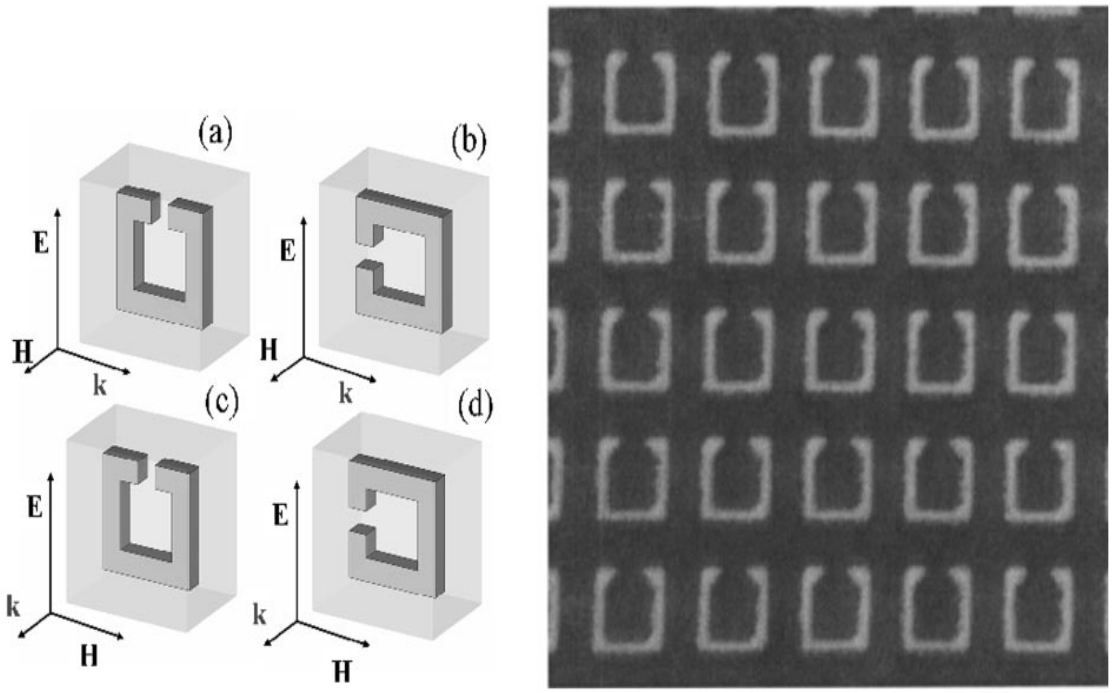

Figure 5.1: Left, Single unit cell of the SRR geometry studied, in all possible EM field propagation directions and polarizations [(a)–(d)]. Right: top view photograph of the SRR metamaterial fabricated by a microlithography process.

The SRR metallic structures are fabricated in a layer-by-layer fashion, alternating layers of polyimide and silver. We used a standard spin-on polyimide (DuPont Pyralin SP

series PI-2525) with a dielectric constant of 2.5. The sequence of layers starts by spinning and curing a 5-μm-thick layer of polyimide on a Si substrate. A 1-μm-thick silver film is deposited on top and patterned by use of standard lift-off techniques. Another layer of polyimide is spun on over the metallic SRR and cured. The thickness of this polyimide layer is 5 μm. Another metal layer is deposited and patterned, with this second layer of SRRs aligned directly over the first. The sequencing of layers continues with another thick polyimide layer followed by a third metallic SRR pattern and so on. The layer-to-layer alignment was done with a Karl Suss MA6 aligner and UV photolithography. The alignment accuracy is of the order of 0.5 μm. After the fabrication, the polyimide-encapsulated metallic SRR structure is removed from the Si substrate.

Because the polyimide has two absorption bands centred about 15 and 30 μm, we chose the dimensions of the periodic SRRs to have a resonance frequency near 6 THz (wavelength of 50 μm), safely below the absorption bands. The unit cell of the structure has dimensions of 7 μm x 7 μm in the SRR plane and 5 μm in the perpendicular direction; the SRR side length is 5 μm, and the other characteristic lengths (ring width, ring depth, gap) are all 1 μm. The total metamaterial has an area of 25 mm x 25 mm. A photograph of the metamaterial is presented on the right-hand side of Fig. 5.1.

The transmission measurements were taken with a Bruker IFS 66 v/S Fourier-transform infrared spectrometer (with a collimated beam) and a polarizer at a frequency range of 3–10 THz. The results are presented in Fig. 5.2. One can readily observe that for polarization (d), with the electric field parallel to the gap-bearing SRR sides, the transmission spectrum shows a gap at approximately 5–8 THz [curve (d) of Fig. 5.2], which we claim to be due to the EEMR effect. This interpretation is further supported by the absence of this gap for the other polarization [curve (c)], where the SRR is symmetric relative to the incident **E**. In orientation (c) we observe only a cutoff frequency at 8 THz, corresponding to the electric cutwire SRR response [for orientation (d) this response is observed in slightly higher frequencies].

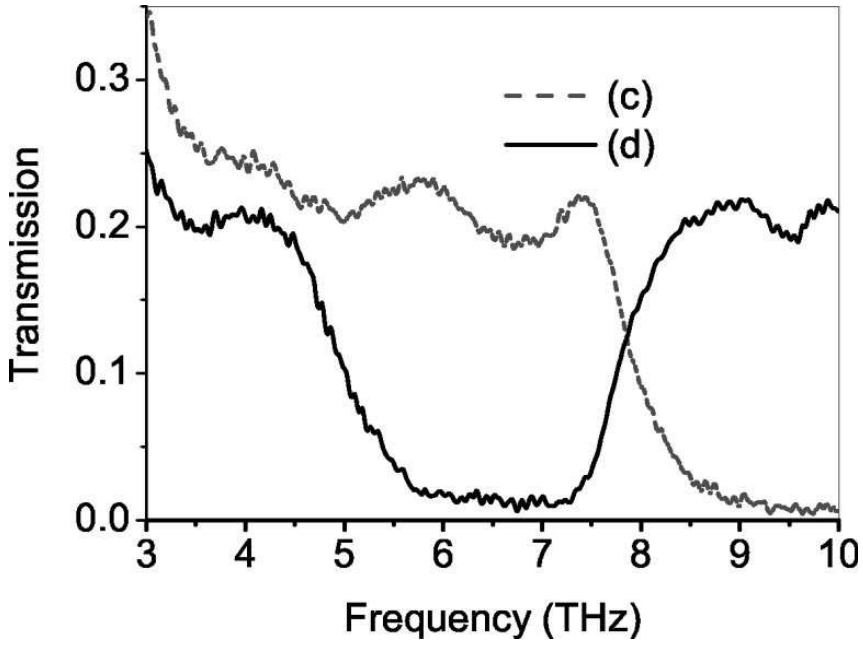

Figure 5.2: Measured transmission spectra for the configurations shown in Figs. 5.1(c) and 5.1(d).

To conclusively verify the origin of the gap at ~ 6 THz and thus the existence of EEMR in this regime, we studied this system theoretically as well. First we reproduced the experimental data by use of transmission and reflection calculations, and then we inverted these data to obtain the effective parameters ε and μ of the metamaterial.

In Fig. 5.3 we show the calculated transmission for the cases presented in Fig. 5.2 as well as for the orientation in Fig. 5.1(a). The transmission was calculated with the finite integration technique (employed through Microwave Studio commercial software) and treating the metal as a dispersive medium following the Drude dispersion model [($\varepsilon = 1-\omega_{pm}^2/(\omega^2+i\omega\gamma)$, with $\omega_{pm}=13.66\times10^{15}$ rad/s and $\gamma=2.73\times10^{13}$ s^{-1}) (Ref. 14)]. For the polyimide background we used dielectric constant ε=2.5 and loss parameter tanδ=0.03. Comparing Fig. 5.3 with Fig. 5.2(a), one can see that the agreement between theory and experiment is very good, adding credibility to our interpretation. Moreover, we obtained theoretically a transmission dip around 6 THz for the orientation in Fig. 5.1(a), where the excitation of the resonance at ω_m is purely magnetic, thus verifying the existence of a magnetic resonance associated with a negative μ at ~6THz. Closing the SRRs for the

configuration of Fig. 5.1(a), thus destroying the oscillating current behavior at ω_m, [50, 51] the dip at ~6 THz disappears, as expected.

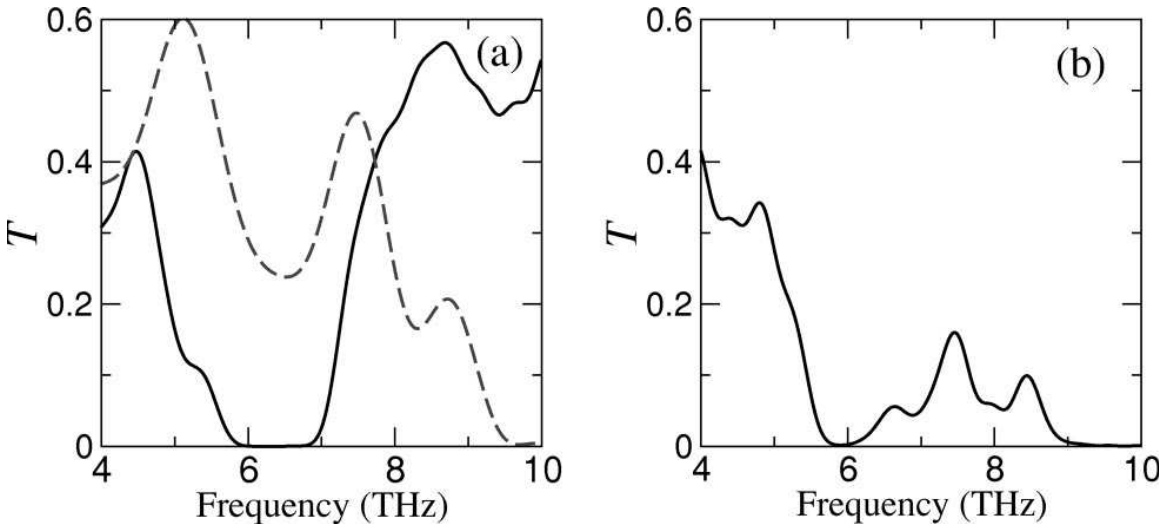

Figure 5.3: (a) Calculated transmission versus frequency for the configurations shown in Figs. 5.1(c) (dashed curve) and 5.1(d) (solid curve). (b) Calculated transmission for the configuration in Fig. 5.1(a).

To offer further and definite proof of the existence of negative magnetic response in our metamaterial around 6 THz, we employed a retrieval procedure [49] to extract the effective ε and μ from the theoretical reflection–transmission results, considering our metamaterial as a homogeneous effective medium. Since, for a propagation direction perpendicular to the SRR plane, the magnetic resonance results to resonance of only the permittivity $\varepsilon(\omega)$, we inverted the scattering data also for the orientation of Fig. 5.1(a), where the magnetic resonance of the SRR appears in $\mu(\omega)$. The inversion results concern only one unit cell of the metamaterial along propagation direction and are shown in Fig. 5.4. Figure 5.4(a) shows effective ε (real part) for the orientations of Figs. 5.1(c) and 5.1(d) [notice the negative ε around 6 THz for Fig. 5.1(d)], while Fig. 5.4(b) shows μ (real part) for the orientations in Figs. 5.1(c) and 5.1(d), as well as Fig. 5.1(a); clearly, the solid curve in Fig. 5.4(a) and the thick dashed–dotted line in Fig. 5.4(b) exhibit the same strong resonance at the same frequency, providing one more verification of the EEMR effect.

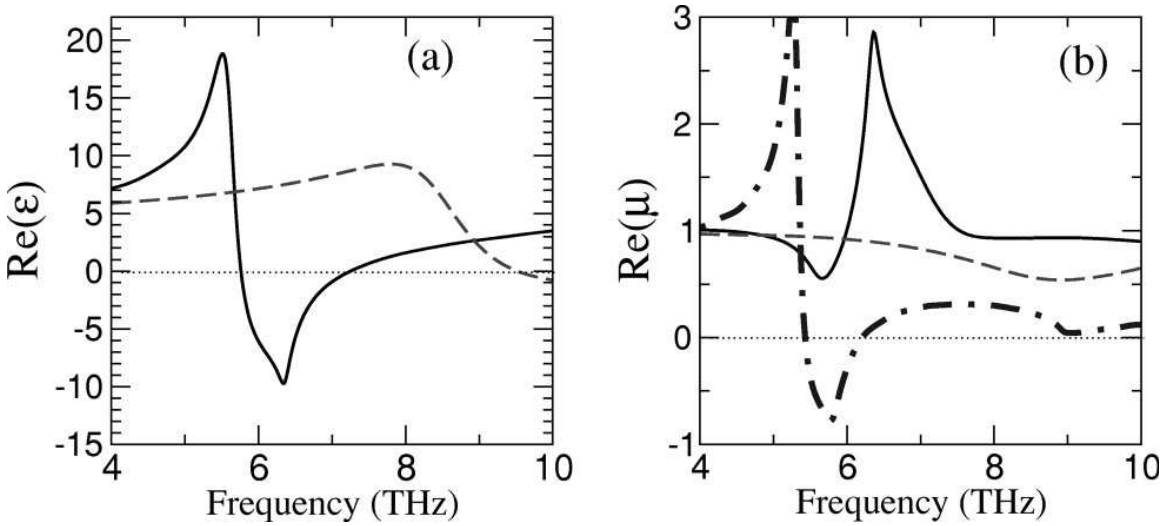

Figure 5.4: (a) Real part of the effective permittivity of the SRR metamaterial shown in Fig. 5.1, for propagation direction and EM field polarization those of Fig. 5.1(d) (solid curve) and Fig. 5.1(c) (dashed curve). (b) Real part of the effective permeability of the SRR metamaterial for the orientations of Fig. 5.1(d) (solid curve), Fig. 5.1(c) (dashed curve), and Fig. 5.1(a) (dashed–dotted curve).

After demonstrating a magnetic resonance response at 6 THz through the EEMR effect, additional measurements were performed to excite the magnetic SRR resonance directly and show that our SRR metamaterial behaves as a negative μ material. In order to achieve that, an external magnetic field perpendicular to the SRR plane should be introduced. In principle, one way to achieve this is by employing a propagation vector **k** parallel to this plane; this is practically impossible for very thin structures. A possible solution to the problem is to employ oblique incidence, producing a **k** component at the SRR plane, $\mathbf{k}_{\parallel}$. For oblique incidence one can achieve an **H** component perpendicular to the SRR plane, $\boldsymbol{H}_{\perp}$. $\boldsymbol{H}_{\perp}$ induces a circular current flow inside the SRRs, which in turn produces just above the resonance frequency a large magnetic dipole moment antiparallel to $\boldsymbol{H}_{\perp}$, leading thus to a negative μ.

The oblique incidence transmission/reflection measurements have been taken using the same setup as in the normak incidence case. Starting from normal incidence ($\boldsymbol{H}_{\perp}$ =0, corresponding to φ=90°, where φ is the angle between the propagation vector **k** and the

SRR plane) in configurations (a) and (b) of Fig. 5.5 and changing φ, we produce a gradually increasing $\boldsymbol{H}_{\perp}$ and we observe the evolution of the transmission and reflection spectra resulting from the interaction of SRRs with $\boldsymbol{H}_{\perp}$.

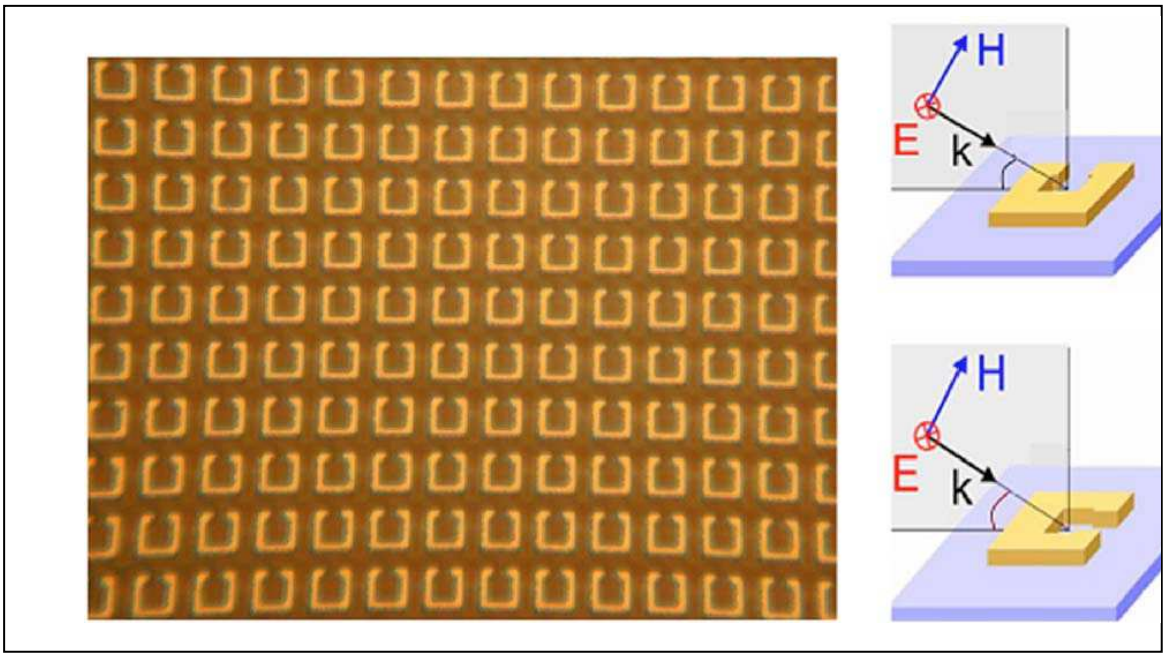

Figure 5.5: (Color online) (Left) Photo of the structure studied. (Right) SRR and external magnetic field configurations studied; (a) electric field (E) parallel to the SRR sides with no gap and (b) E parallel to the SRR sides with the gap.

In Fig. 5.6(a) we present the reflection spectra of the SRR metamaterial at oblique (φ =77°, 70°, 60°, 50°) incidence, for configuration (a) of Fig. 5.5 (**E** parallel to the no-gap sides of the SRRs). At the minimum obliqueness case (φ =77°), the reflection (*R*) spectrum shows a weak peak at around 6 THz [dashed curve in Fig. 5.6(a)], which for growing obliqueness (decreasing φ) strengthens and broadens (~5.5–7.5 THz). For configuration (a), coupling of the incident **E** to the magnetic resonance of the SRRs (EEMR) cannot occur, since SRRs are symmetric with respect to **E** [28]

Thus, the changes in the *R* spectra with decreasing φ are exclusively due to the interaction of the SRRs with the increasing $\boldsymbol{H}_{\perp}$. $\boldsymbol{H}_{\perp}$ results in the excitation of circular currents in the SRRs and thus to the excitation of the magnetic SRR resonance. Thus, the peak in the *R* spectra at ~5.5–7.5 THz, for oblique incidence, can only be a result of negative μ in that frequency regime.

The transmission (T) spectrum for the same SRR metamaterial and the same measurement procedure is depicted in Fig. 5.6(b). The dashed curve refers to normal incidence ($\varphi = 90°$). The oscillations observed in the T spectrum are due to the polyimide multilayer structure. However, at oblique incidence ($\varphi = 80°, 60°$) $\boldsymbol{H}_{\perp}$ excites the magnetic resonance. This is manifested also in the T spectrum with the evolution of a dip at 5.5–7 THz for $\varphi = 80°$, which broadens and deepens at $\varphi = 60°$. However, this T dip is not as pronounced as the respective R peak of Fig. 5.6(a), most probably due to multiple scattering effects at the interfaces between the adjacent Ag/polyimide layers as well as due to absorption. In the inset of Fig. 5.6(b) we show the calculated T spectrum for $\varphi = 0°$ (**k** is parallel and **H** is perpendicular to the SRR plane).

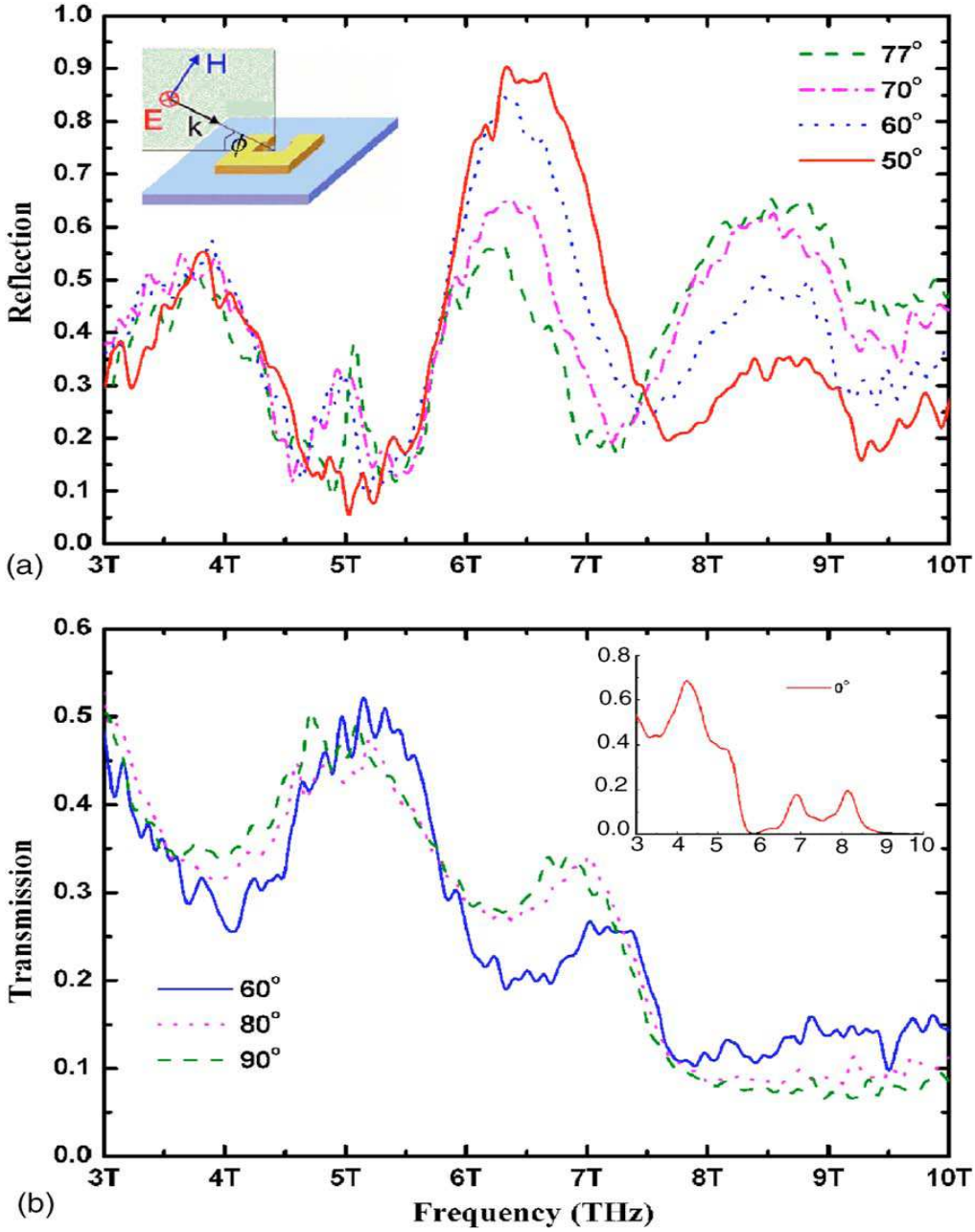

Figure 5.6: (Color online) (a) Measured reflection spectra at oblique incidence for our five layer SRR system for configuration (a) of Fig. 5.1 (shown also in the inset). One can observe the evolution of a reflection peak as the angle φ changes (φ is the angle between k and the SRR plane). (b) Measured transmission spectra as φ changes for configuration (a) of Fig. 5.1. In the inset of (b) the calculated transmission spectrum for φ =0° is also presented.

In Fig. 5.7(a) the reflection spectra of the SRR metamaterial are presented for configuration (b) of Fig. 5.5 (**E** parallel to the gap-bearing side of the SRRs). In the case of minimum obliqueness (φ =77°) the *R* spectrum shows a well-defined peak [dashed curve in Fig. 5.7(a)], which is attributed to the EEMR effect, present in all cases. For stronger oblique incidence (φ =70°, 60°, 50°) the peak in *R* remains almost unchanged in shape and amplitude, despite the emergence of $\boldsymbol{H}_{\perp}$. One would expect the *R* peak to broaden and strengthen for increasing oblique incidence due to the addition of the $\boldsymbol{H}_{\perp}$ excitation of the magnetic resonance [$\boldsymbol{H}_{\perp}$ produces a resonance structure in $\mu(\omega)$, in addition to the resonance structure in ε (ω) produced by **E** (for configuration (b)]. However, theoretical calculations of the effective ε and μ parameters extracted from the corresponding theoretical reflection-transmission results (considering the SRR metamaterial as a homogeneous effective medium) show that the resonance in ε is much stronger and wider than that in μ and thus dominates the reflection and transmission spectra. This large strength ratio of the two resonances explains the fact that the *R* peak observed in our measurements due to the EEMR effect remains almost unaffected by increasing oblique incidence. Our conclusions are further supported by the corresponding oblique incidence transmission measurements [see Fig. 5.7(b)], which show no altering of the well-studied *T* dip, attributed to the EEMR effect, as one goes from normal to oblique incidence. The dip does not change with decreasing φ, which implies that the resonance in ε masks the occurring resonance in μ. In other words, in configuration (b) the electric field is the dominant driving force of the resonance.

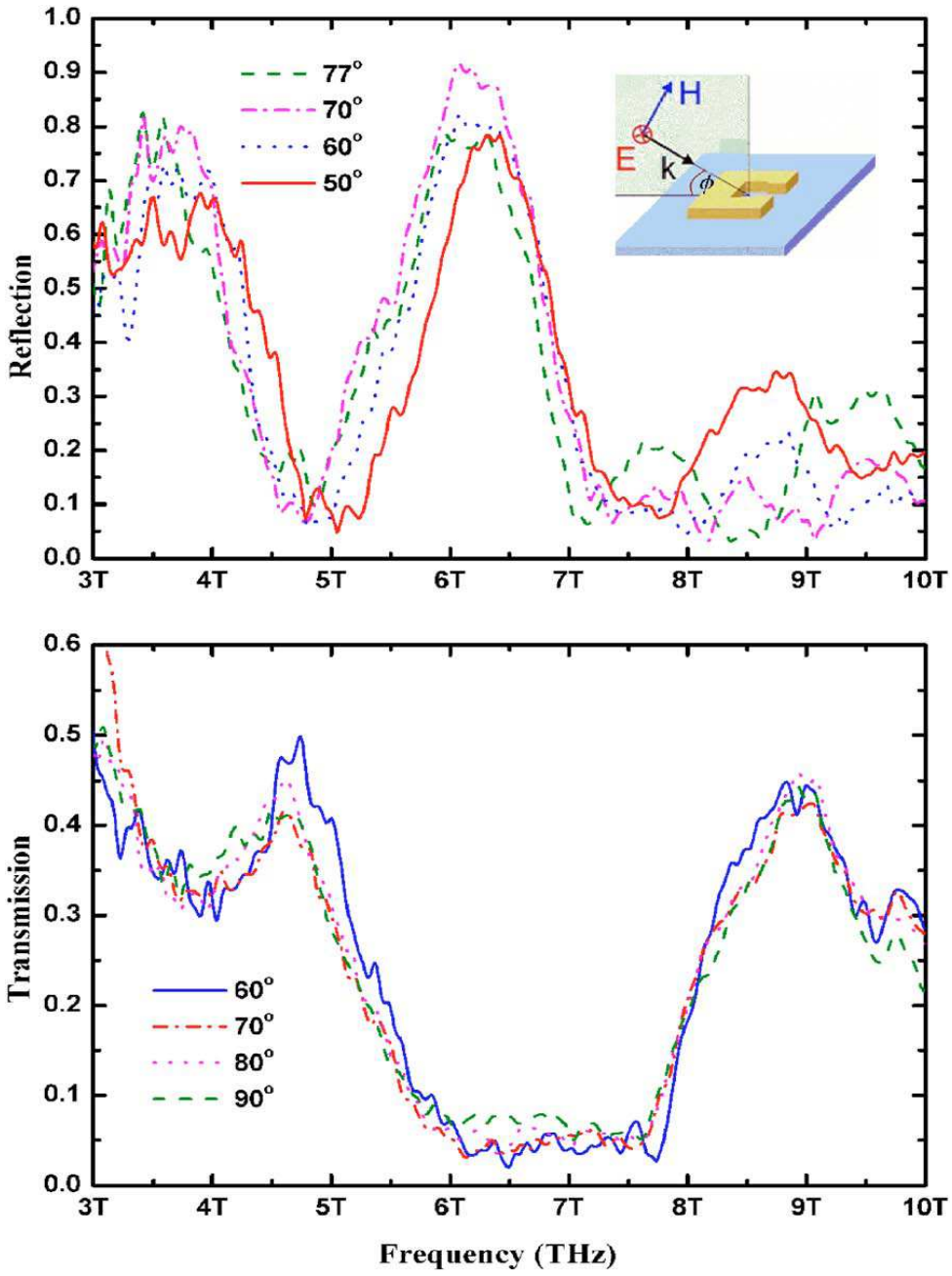

Figure 5.7: (Color online) (a) Measured reflection at oblique incidence for configuration (b) of Fig. 5.1 (shown also in the inset). The angle mentioned in the legends is the angle φ between k and the SRR plane. (b) Measured transmission spectra for configuration (b) of Fig. 5.1 as φ changes.

In conclusion, a mechanically flexible periodic structure consisting of alternating dielectric and SRR metallic layers was microfabricated. By direct transmission measurements under normal incidence, supported by theoretical results, we have demonstrated a magnetic resonance response at ~ 6 THz through the EEMR effect. The magnetic resonance response of our SRR system was demonstrated further and more directly using oblique incidence transmission and reflection measurements. There, the resonance is manifested by the emergence of a reflection peak and a corresponding transmission dip as the obliqueness of incidence increases in the symmetric configuration (a) (**E** parallel to the no-gap sides of the SRR); for this configuration and for oblique incidence, a component of **H** perpendicular to the SRR plane emerges, which is the only cause of the excitation of the magnetic resonance; hence, the latter appears as a resonance in $\mu(\omega)$. For the configuration with **E** parallel to the gap-bearing side of the SRRs, the same resonance is excited mostly by the electric field, resulting to an electric response of the system, i.e., a resonance in the permittivity $\varepsilon(\omega)$, while the magnetic field component for oblique incidence plays a minor role in exciting the SRR resonance. Thus, our results provide further evidence for the existence and the importance of the EEMR effect and prove definitely the existence of magnetic response with negative magnetic permeability in our SRR system in the ~6 THz regime.

5.2.2 Multi-gap split ring resonators

In this study we have fabricated and characterized multigap SRR metamaterials showing a magnetic response at THz frequencies (up to 14 THz). The fabrication method has already been explained in the previous section (5.2.1). Our SRR metamaterials are composed of single-ring silver SRRs, fabricated in polyimide. The SRRs size is 5×5 μm^2 while the u.c. dimensions are 7×7×5 μm^3. All the other characteristic lengths (ring-width, ring-depth, and gap) are of 1 μm. The mask permits fabrication of a multi-stacked structure with a polyimide layer between successive layers of SRRs. Also the mask has an area covered with SRRs of 25×25 mm^2 designed to permit easy handling of the sample and good interaction between probing beam and the sample. SRR structures with two (2) gaps (symmetric and asymmetric) and three (3) gaps were fabricated through a standard photolithography technique. They consist of two (2) metallic layers (silver) of SRRs embedded in three (3) layers of polyimide (see Fig. 5.8). The existence of multiple gaps allows achieving higher magnetic resonance frequencies in the same unit cell configurations and scale; therefore avoiding additional fabrication and characterization difficulties.

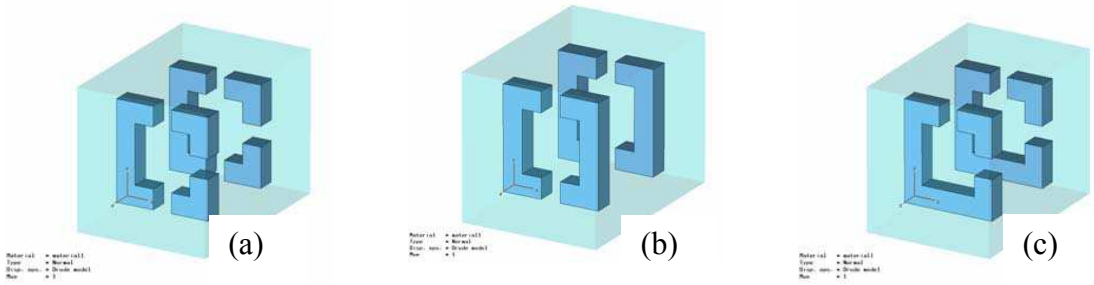

Figure 5.8: A single unit cell of all the SRR geometries studied (a): 3-gap SRR, (b): 2-gap asymmetric SRR, (c): 2-gap symmetric SRR.

The transmission measurements of our structures were taken as it is explained in the previous section. But this time our frequency range is extended (2-21 THz) and all the measurements were taken for the case where the EM wave propagation is perpendicular to the SRR plane.

For the 3-gap case the transmission measurements are shown in Fig.5.9, for various external **E** polarizations. It can be seen that going from the 0º polarization (where the SRRs are symmetric with respect to **E**) to the 90º polarization, there is a clear evolution of a transmission dip, which is a clear indication of the presence of a magnetic resonance in this regime, excited by the external electric field through the EEMR effect.

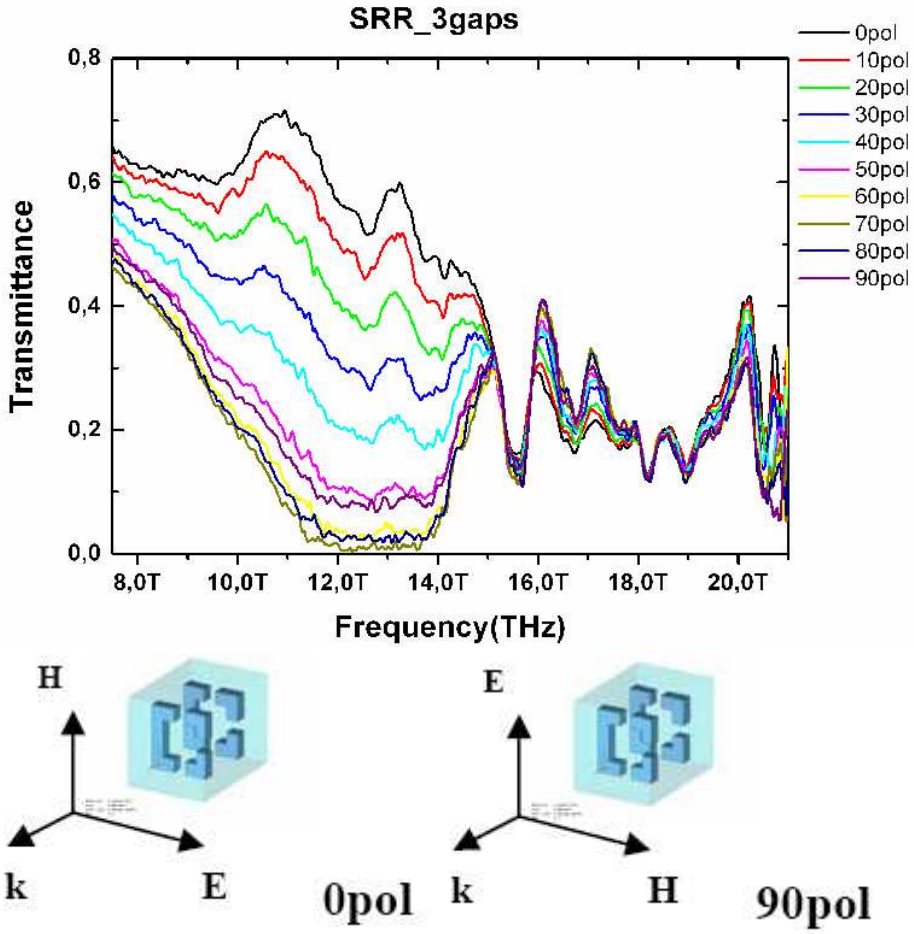

Figure 5.9: Measured transmittance spectra for three-gap SRR structures with $5\times5\mu m^2$ size (two layers, see Fig. 5.8a). In all cases the propagation of the EM waves is perpendicular to the SRRs plane. The solid black curve shows *T* for a polarization with E parallel to the sides of the SRRs with the two gaps, while the solid olive curve shows *T* for E parallel to the sides with one gap (as shown in the right panels). All the intermediate polarizations are also presented for comparison reasons. The dip at ~13 THz which appears going from 0º to 90º polarization is a clear indication of a magnetic resonance in that regime.

A major problem for the operation of multidimensional LH structures is the occurrence of the Electric Excitation of the Magnetic Resonance (EEMR effect) for certain polarizations of the external **E**-field with respect to the SRR geometry. To solve this problem it is required to fabricate symmetric SRR structures, like multigap SRRs. We

have thus tested two-gap symmetric SRR structures in the THz frequency regime (Fig. 5.8c), and compared their transmittance characteristics with the asymmetric ones of two-gaps (Fig. 5.8b) and three-gaps (Fig. 5.8a).

For the 2-gap asymmetric SRR case the calculated transmission spectra are presented in Fig. 5.10, and the transmittance measurements are shown in Fig. 5.11 for various external **E** polarizations. It can be noted that for both **E** polarizations there is no mirror symmetry of the SRR with respect to **E** and thus a dip in the *T* spectrum appears at ~9 THz (observed both in the simulations as well as in the measurements), which is a clear indication that a magnetic resonance occurs at this frequency.

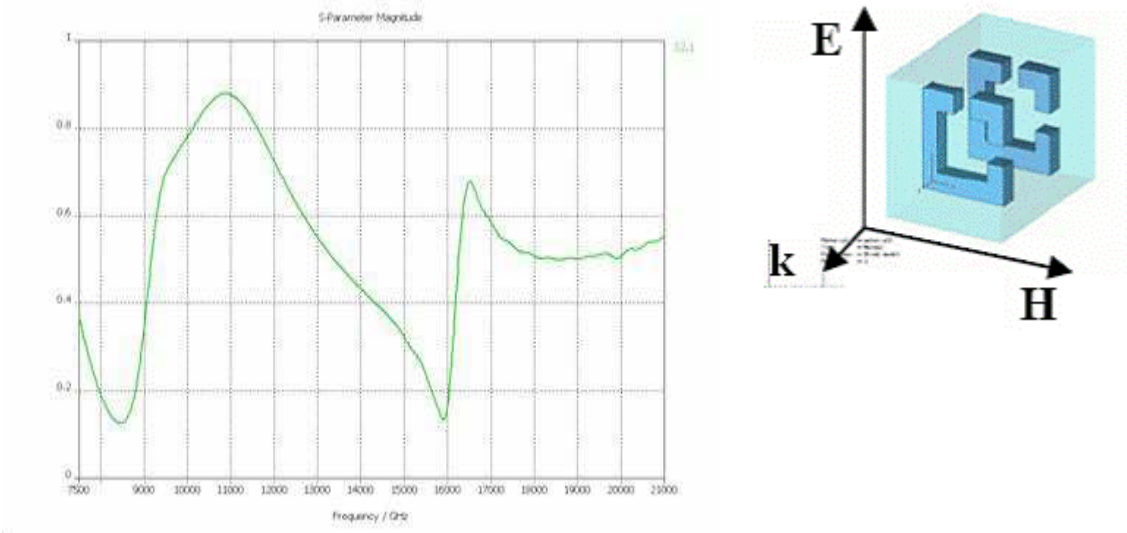

Figure 5.10: SRR structure with two gaps (asymmetric, Fig.5.8b): Calculated transmission vs. frequency for the configuration shown in the inset. The dip at around 9 THz shows the location of the magnetic resonance.

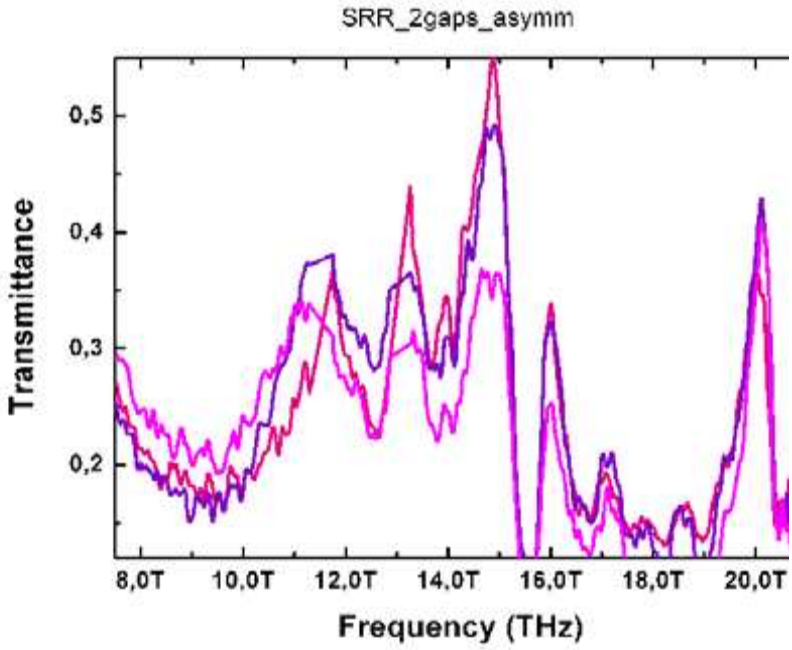

Figure 5.11: Measured transmittance spectra for two-gap SRR asymmetric structures with 5×5 μm^2 size (two layers, see Fig. 5.8c). In all cases the propagation of the EM waves is perpendicular to the SRRs plane. The solid red and magenta curves show *T* for both polarizations of E, i.e. parallel to the sides of the SRRs with one gap at each time.

For the 2-gap symmetric SRR case the measured transmission spectra are presented in Fig. 5.12, and the transmittance measurements are shown in Fig. 5.13 for various external **E** polarizations. It can be seen that for both **E** field polarizations there is mirror symmetry with respect to the SRR geometry, and there is no dip in the *T* spectrum in the low frequency regime. It can be thus concluded that for this symmetric case there is no electric excitation of the magnetic resonance. As it was already discussed in Chapter 4, this is an advantage when one wants to build multi dimensional metamaterials. Symmetric SRRs are needed in designing 2D and /or 3D structures.

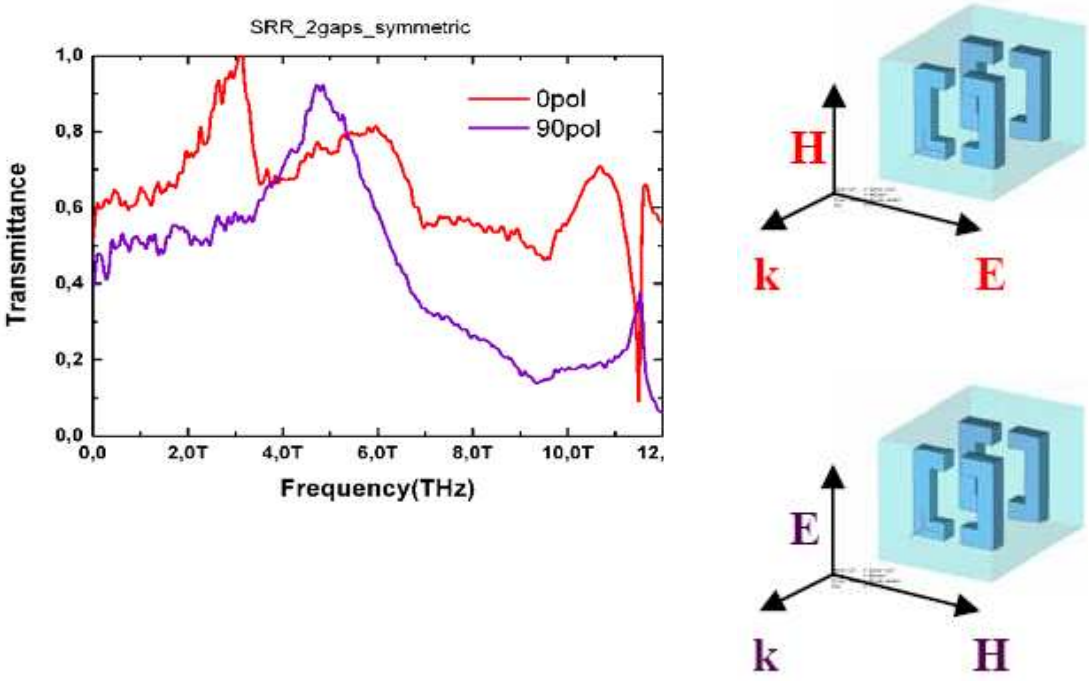

Figure 5.12: Measured transmittance spectra for two gap SRR symmetric structures with 5×5 μm^2 size (two layers, see Fig. 5.8 (b)). In all cases the propagation of the EM waves is perpendicular to the SRRs plane. The solid purple curve shows *T* for a polarization with E parallel to the sides of the SRRs with no gaps, while the solid red curve shows *T* for a polarization with E parallel to the sides of the SRRs with the gaps.

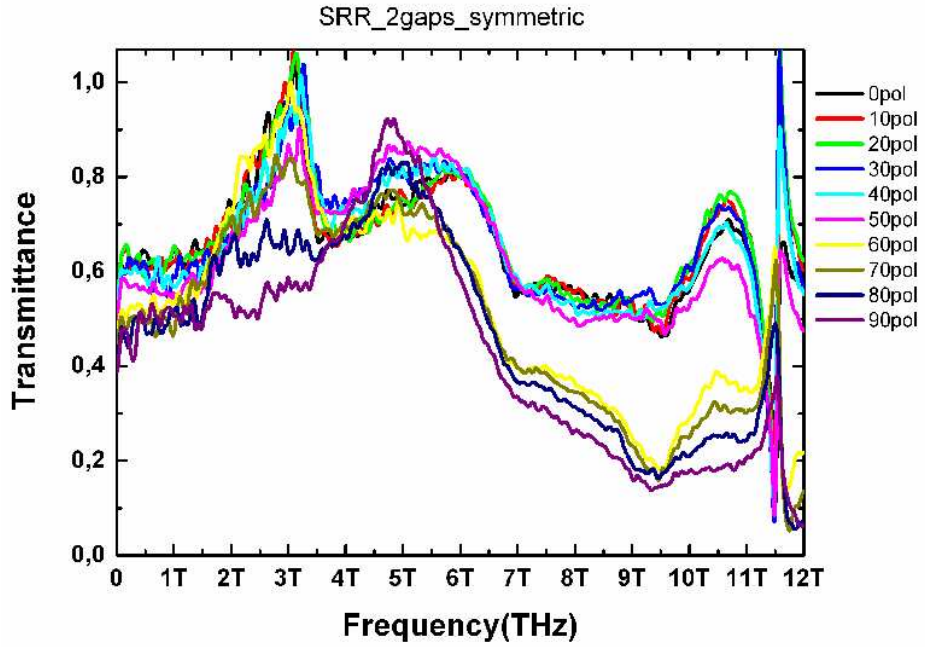

Figure 5.13: Measured transmittance spectra for two-gap SRR symmetric structures with 5×5 μm^2 size (two layers, see Fig. 5.8 (b)). The solid purple curve shows *T* for a polarization with E parallel to the sides of the SRRs with no gaps, while the solid black curve shows *T* for a polarization with E parallel to the sides of the SRRs with the gaps. All the intermediate polarizations are also presented for comparison reasons.

From the THz measurements performed on the multigap SRR metamaterials and the corresponding Microwave Studio simulations we can conclude that the presence of two symmetric gaps in the SRR leads to the elimination of the electric excitation of the magnetic resonance (the so-called EEMR effect) due to the mirror symmetry in the SRR, while the EEMR effect is present in the asymmetric structures for perpendicular propagation and the electric field parallel to the gap-bearing sides of the SRRs. Moreover, as it was expected, by increasing the number of the gaps in the SRRs the magnetic resonance frequency moves upwards. For example, in the three-gap structure the gap in *T*, which is related to the magnetic resonance of the SRRs, occurs at ~13 THz while for the one-gap SRR structures (reported previously) the resonance was observed at ~6 THz.

5.2.3 Short slab-pair and continuous wire metamaterials

To simplify the fabrication and characterization of negative μ and/or LH metamaterials, new improved and simplified designs have been introduced, involving pairs of short-slabs as magnetic resonators. According to theoretical and experimental studies, the parallel short-slab pairs structure allows replacing the SRR as magnetic resonator [17] but also could possibly give simultaneously negative ε, and negative μ, therefore negative n [45, 47]. Since the existence of simultaneously negative ε and μ in short-slab pair structures can occur only under extreme conditions [46], a modification of the structure, consisting of continuous wires in addition to the slab pairs, has been proposed, and the occurrence of negative index, n, in the microwave regime has been demonstrated unambiguously, both theoretically and experimentally [44, 46, 48, 75]. The short-slab pairs arrangement (with or without continuous wires) has obvious advantages compared to the conventional SRR plus wires design: It is simpler in fabrication and, moreover, LH behavior can be achieved for incidence normal to the short-slab pairs plane, thus enabling the observation of negative index behavior with only a few, if not only one, short-slab pairs layer. The latter

feature could facilitate the realization and characterization of high-frequency LH metamaterials.

In this study, we have designed, fabricated, characterized and analyzed a μm-scale structure consisting of short-slab pairs and continuous wires (see Fig. 5.14) targeting the observation of LH behavior in the far infrared frequency regime. Our short-slab pairs metamaterial is composed of Ag/Ti slab pairs, that are embedded in a dielectric matrix, while two continuous wires are added on either side of each pair, as shown in Fig. 5.14, to ascertain a wide negative ε region. For EM waves incident normally to the short-slab pairs structure and the electric field polarized parallel to the continuous wires (see Fig. 5.14), the short-slab pairs will exhibit a magnetic resonance, providing a negative μ region, and the continuous wires will lead to negative ε, thus providing the possibility to achieve LH behavior. The elements of the pairs are separated by a dielectric spacer of small thickness, t_s. The unit cell (u.c.) of the system is presented in Fig. 5.14(a) (3D view) and Fig. 5.14(b) (cross section). The dimensions are α_E = 20μm, α_H = 16μm, α_k= 1.9μm where α are the respective lattice constants in the directions of **E**, **H** and **k** of the normal incident electromagnetic wave. The slab length is l = 16.5μm, its width is w = 8μm, the thickness of the dielectric spacer between the elements of the pairs is t_s= 0.7μm, the continuous wire width is w' = 2μm and finally the continuous wire to short-slab distance (from metal edge to metal edge) is d=1 μm. The metamaterials have been fabricated on silicon wafers in a layer-by-layer method, alternating layers of dielectric and silver to get one or three u.c. A spin-on polyimide (DuPont Pyralin SP series PI-2525) with a dielectric constant of 2.5 has been used as matrix material, while silicon has been applied as the high-index dielectric spacer between the pair elements. The layer-to-layer alignment has been done using a Karl Süss MA6 aligner and UV photolithography. The alignment accuracy is of the order of 0.5 μm. After the fabrication, the polyimide-encapsulated metallic structures have been removed from the silicon substrates. The total area of each structure is 25×25 mm^2.

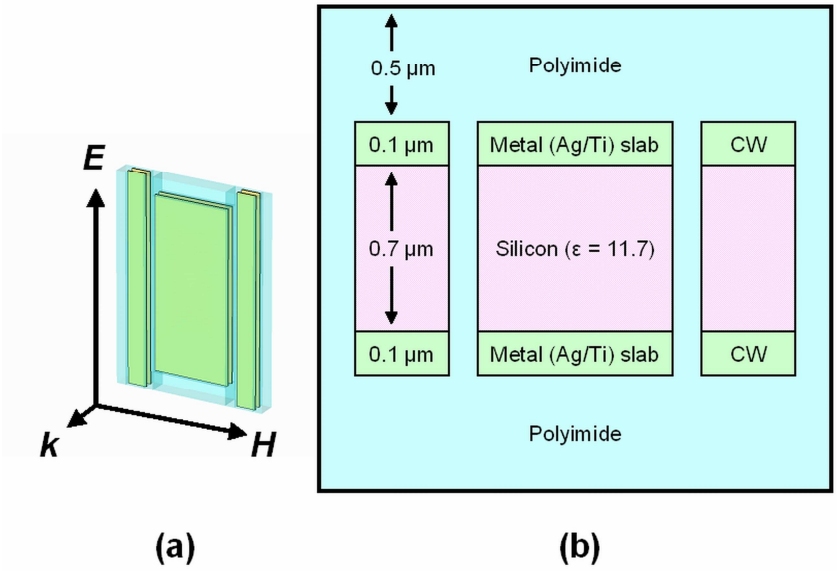

Figure 5.14: (a) A single unit cell of the slab-pair metamaterial under study, (b) k-H cross section of the slab-pair metamaterial, passing through the middle of the u.c. along E direction (metal thickness 0.1 μm, polyimide 0.5 μm, Silicon 0.7 μm). The Figure scaling in the two different dimensions is dissimilar. CW denotes the continuous wires.

The transmission measurements have been taken using a Bruker IFS 66v/S FT-IR spectrometer (with a collimated beam) and a polarizer, at the frequency range of 1.5-10 THz, at normal incidence whereas the reflection measurements were taken at almost normal incidence (77°). The transmission and reflection simulations have been performed using the Microwave Studio commercial software, and considering one and three u.c. along the propagation direction and periodic boundary conditions along the lateral directions. The metal has been treated as a dispersive medium following the Drude dispersion model ($\varepsilon = 1-\omega_{pm}^2/(\omega^2+i\omega\gamma)$, with $\omega_{pm}=13.66\times10^{15}$ rad/s and $\gamma=2.73\times10^{13}$ s^{-1}). For polyimide and silicon the dielectric constants that have been used are $\varepsilon_p=2.5$ and

ε_{Si}=11.9 respectively, while the corresponding loss parameters are $\tan\delta_p$=0.03 and $\tan\delta_{Si}$=0.04.

In Fig. 5.15 (a) the reflection (*R*) spectrum of a slab-pair metamaterial consisting of one unit cell (u.c.) along propagation direction is presented, at almost normal incidence (77°), and ***E*** parallel to the continuous wires. Two dips can be clearly observed, a broad one, which is located at ~3.5-5.5 THz, and a narrower one, at ~2.4-3.2 THz. In Fig. 5.15(b), the transmission (*T*) spectrum of the same slab-pair metamaterial is depicted for normal incidence (***E*** parallel to the continuous wires) (See Fig. 5.14(a)). At a first glance, one can observe a broad peak centered at ~4.4 THz. It can be noticed though that this broad peak contains a small shoulder, at ~2.9 THz, which is close to the position of the narrow *R*-dip observed in Fig. 5.15(a). This *T*-shoulder and the associated *R*-dip are due to the LH behavior of the system in the frequency region 2.4-3 THz, as it is further confirmed from corresponding numerical study.

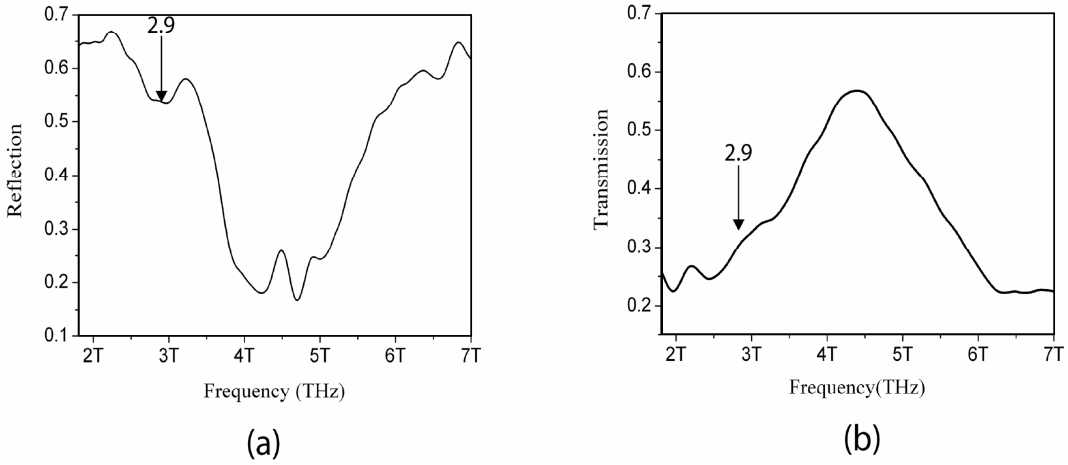

Figure 5.15: (a) Measured reflection spectra for our slab-pairs metamaterial, for one u.c, at close to normal incidence (77°) as defined in Fig.5.1, (b) corresponding measured transmission spectra.

Numerical reflection and transmission results for our system (one u.c. along propagation direction) at normal incidence are shown in Fig. 5.16. It can be seen that T (dashed line) shows a small peak, while R (solid line) exhibits a corresponding dip, centered at ~2.7 THz. These spectral features are in very good agreement with the experimental results presented in Fig. 5.15, thus providing evidence for the occurrence of LH behavior at ~2.7 THz. To unambiguously confirm that the transmission peak and the reflection dip at ~2.7 THz (observed both experimentally and numerically in our structures) are due to negative effective refractive index behavior, we have calculated the effective ε, μ and n versus frequency from the numerical transmission and reflection data, via the standard retrieval procedure [49, 76]; the extracted ε, μ and n are shown in Figs. 5.17(a), 5.17(b) and 5.17(c) respectively. The graphs show that the real part of the permittivity is negative up to almost ~4.5 THz, while the real part of the permeability is negative over a narrow frequency band ranging from ~2.6-3 THz. This in turn results in negative n at the frequency region of ~2.6-3 THz as is confirmed in Fig. 5.17(c). (The slightly broader negative n regime compared to that of negative μ comes from the fact that negative n can also be achieved for a negative ε combined to positive μ but with large Im(μ) values. This negative ε-high Im(μ) regime corresponds to very high losses (see the large Im(n) in Fig. 5.17(c)) and is not considered here as negative index propagation regime. It is thus clear that all the obtained results, namely measured and calculated T and R, as well as the effective parameters ε, μ and n, point to the occurrence of a negative refractive index propagation regime at ~2.6-3 THz for our one u.c. short-slab pair/continuous wires metamaterial.

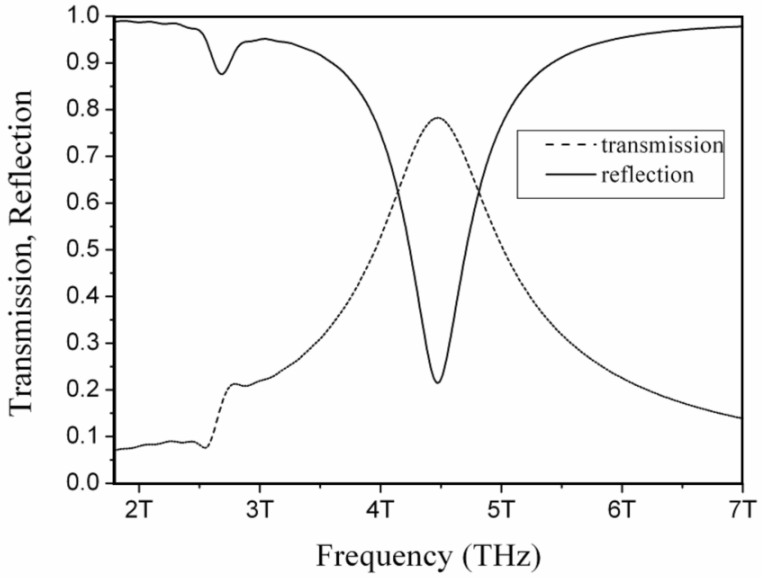

Figure 5.16: Calculated transmission (dashed line) and reflection (solid line) vs. frequency for one u.c. of our slab-pair metamaterial.

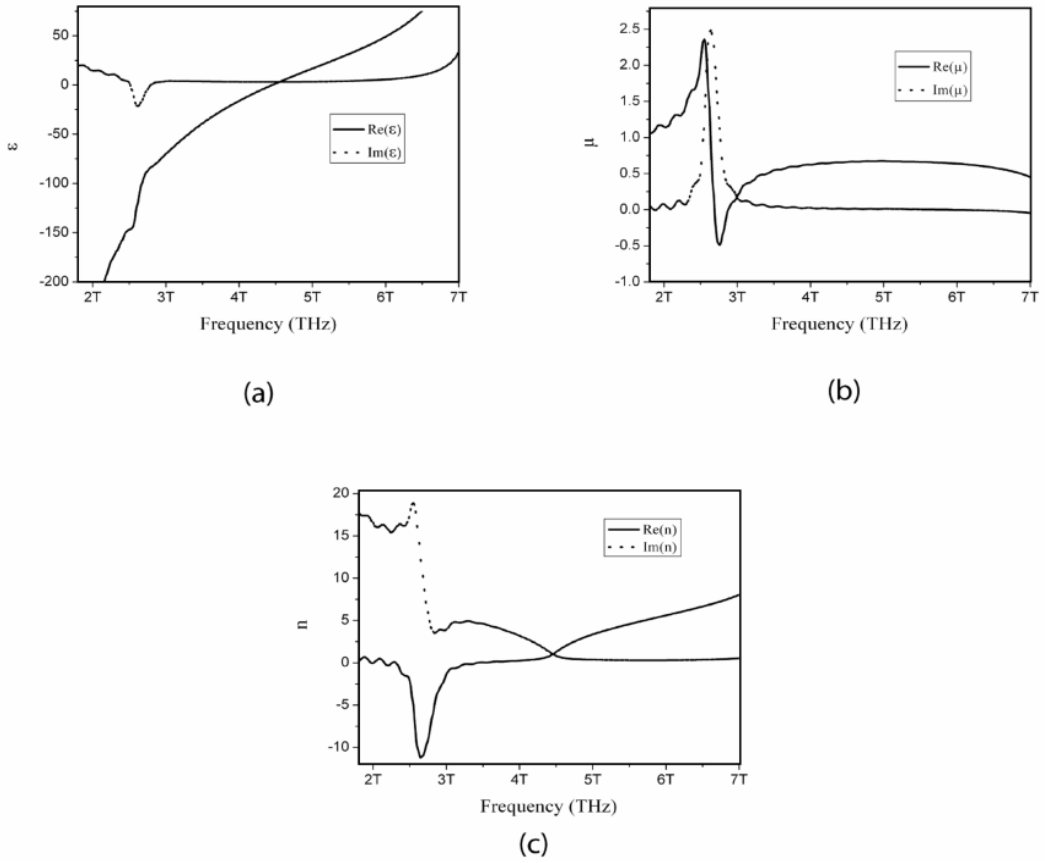

Figure 5.17: Real (solid line) and imaginary (dashed line) parts of the effective permittivity [panel (a)], permeability [panel (b)] and refractive index [panel (c)] calculated from the transmission and reflection data shown in Fig. 5.16.

To add further proof to our arguments and examine further the behavior of our metamaterial, i.e., quality and robustness of LH behavior, we have conducted the same measurements and calculations for three layers of the metamaterial, i.e. three u.c. along propagation direction. The corresponding data are presented in Figs. 5.18-5.19. In particular, the *T*- and *R*-spectra measured are illustrated in Fig. 5.18, showing the occurrence of a *T*-peak and a corresponding *R*-dip centered at ~2.3 THz. It is in this frequency region that we claim the occurrence of negative *n*, i.e. left-handed, behavior. (The slight difference between the one u.c. and three u.c. results are possibly due to the non-uniformity in the thickness of the layers of the samples and the interaction between adjacent layers along propagation direction. We suspect that the existence of an electric resonance nearby may play a role, given the fact that the relative excitation strengths of the two resonance depend on the incident angle and other aspects of the experiment). The numerical *T* and *R* results are presented in Fig. 5.19 and are in quite good agreement with the experiments. According to the corresponding calculations, the double peak structure that appears between 3.5-5.5 THz can be attributed to Fabry-Perot oscillations.

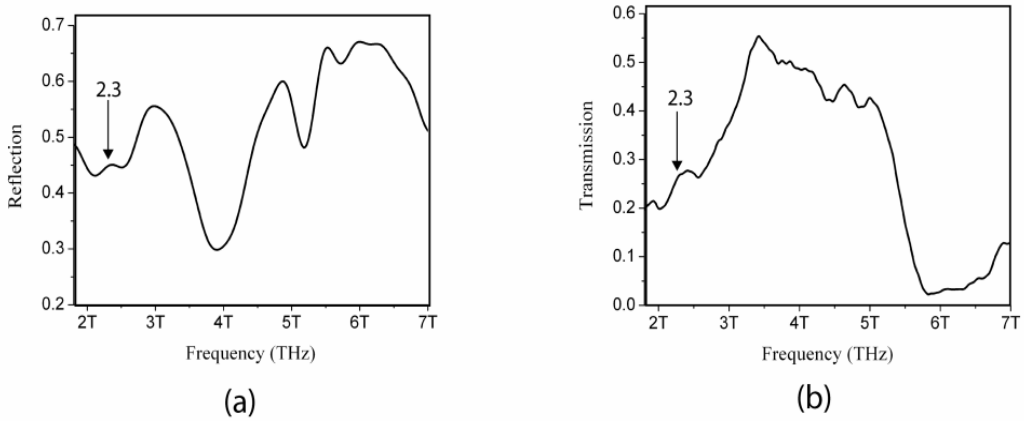

Figure 5.18: (a) Measured reflection spectra of three u.c. slab-pairs metamaterial at close to normal incidence (77°), (b) measured transmission spectra for three u.c. of the metamaterial.

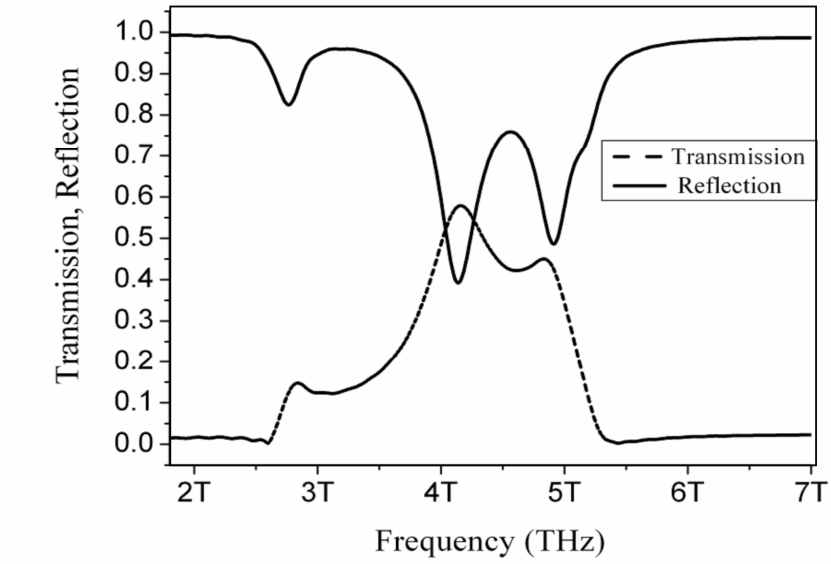

Figure 5.19: Calculated transmission (dashed line) and reflection (solid line) vs. frequency for the three u.c. slab-pairs metamaterial.

Additional investigating simulations show that by reducing the thickness of the high-index dielectric (silicon) of our structure to 0.25 μm or replacing it with a low-index material (polyimide), the negative index behavior disappears. This is due to the fact that reducing the thickness of the high-index silicon leads to a decrease in the strength of the magnetic permeability, thus negative μ is not achieved; On the other hand, replacing Si with polyimide shifts the magnetic resonance to frequencies higher than the plasma frequency of the system, where the left handed behavior can not be observed.

As a conclusion, we have fabricated a μm-scale metamaterial composed of slab-pairs and continuous wires, by means of a photolithography technique. Both one and three layers of metamaterial (u.c. along propagation direction) have been fabricated. Transmission and reflection measurements under normal incidence have given indications that our metamaterial shows negative refractive index behavior at 2.6-3 THz. Simulations of both transmission and reflection as well as inversion of the obtained data for calculating the effective parameters ε, μ and n, confirm the existence of a negative refractive index regime at ~2.4-3 THz. The slab-pair and continuous wires design opens new paths for the realization of negative index materials at optical frequencies.

Chapter 6

Switchable Composite Metamaterials

6.1 Introduction

The left-handed (LH) behaviour of composite metamaterials at microwave and far infrared frequencies were presented so far. In this chapter, the photoconductive switching properties of split ring resonators (SRRs) are investigated.

As it was discussed in the previous chapters, the SRR element consists of metallic rings with gaps that act like a capacitor–inductor (LC) circuit when a magnetic field component is perpendicular to their plane. Due to the resonant circular currents in the rings they exhibit a resonant magnetic response at $\omega_m = 1/(LC)^{1/2}$ associated with these resonant circular currents [6, 30, 50]. Due to this resonance SRR elements generate the negative magnetic permeability (μ) response and they have great importance in LH studies.

A significant challenge in LH materials research is the tuning and switching of such materials. The all-optical switching of the electromagnetic response of SRRs at THz

frequencies by the photoexcitation of carriers in the sample substrate is reported by Padilla et al [25].

In our study, the effect of conductivity variation as a proposed method for the achievement of photoconductive switching properties of split ring resonators (SRRs) is investigated through simulations. Three different systems that are applicable under certain fabrication and/or optical excitation conditions are described and investigated.

6.2 Optically switchable split ring resonators

In our studies, simulations were performed for three different physical configurations (herein after referred to as models) and the finite integration technique employed through Microwave Studio commercial software was used for transmission calculations. These three models are illustrated in Fig. 6.1 a–c. The left panels shown in Fig. 6.1 illustrate the general view of one metamaterial unit cell, whereas the right panels show the gap region in closer detail. In the first model (Fig. 6.1 a), the effect of a photoconductive substrate is investigated by way of increasing the conductivity (σ) of the substrate region to symbolize illumination with higher optical powers.

In comparison, model 2 (Fig. 6.1 b) employs insulating substrates. Split ring resonators are placed atop thin films of deposited or epitaxially grown photoconductive material. It is noteworthy that model 2 is also applicable to photoconductive substrates for which the optical absorption coefficient (α) is so high that the photogeneration of carriers is confined to a thin surface layer. On the other hand, model 1 better suits photoconductive substrates with low α, due to the possibility of photogeneration throughout the entire substrate. The last model includes photoconductive material in a localized area slightly larger than the split ring gap regions beneath the gaps. To realize such a structure, a two step micro-fabrication sequence must be employed: first the photoconductive gap regions must be defined by way of chemical or physical etching, followed by the deposition of the resonator pattern. Even when the entire substrate is illuminated, photogeneration for such a structure is limited to the gap regions only. In addition, model 3 also describes those situations where the photogeneration of carriers is

localized at the gap region by use of a focused laser beam, even if the photoconductive layer or substrate is not patterned. Models 2 and 3 are both appropriate for describing front- and substrate-side optical illumination, whereas model 1 is suited only for front-side illumination because of the thick photoconducting substrate.

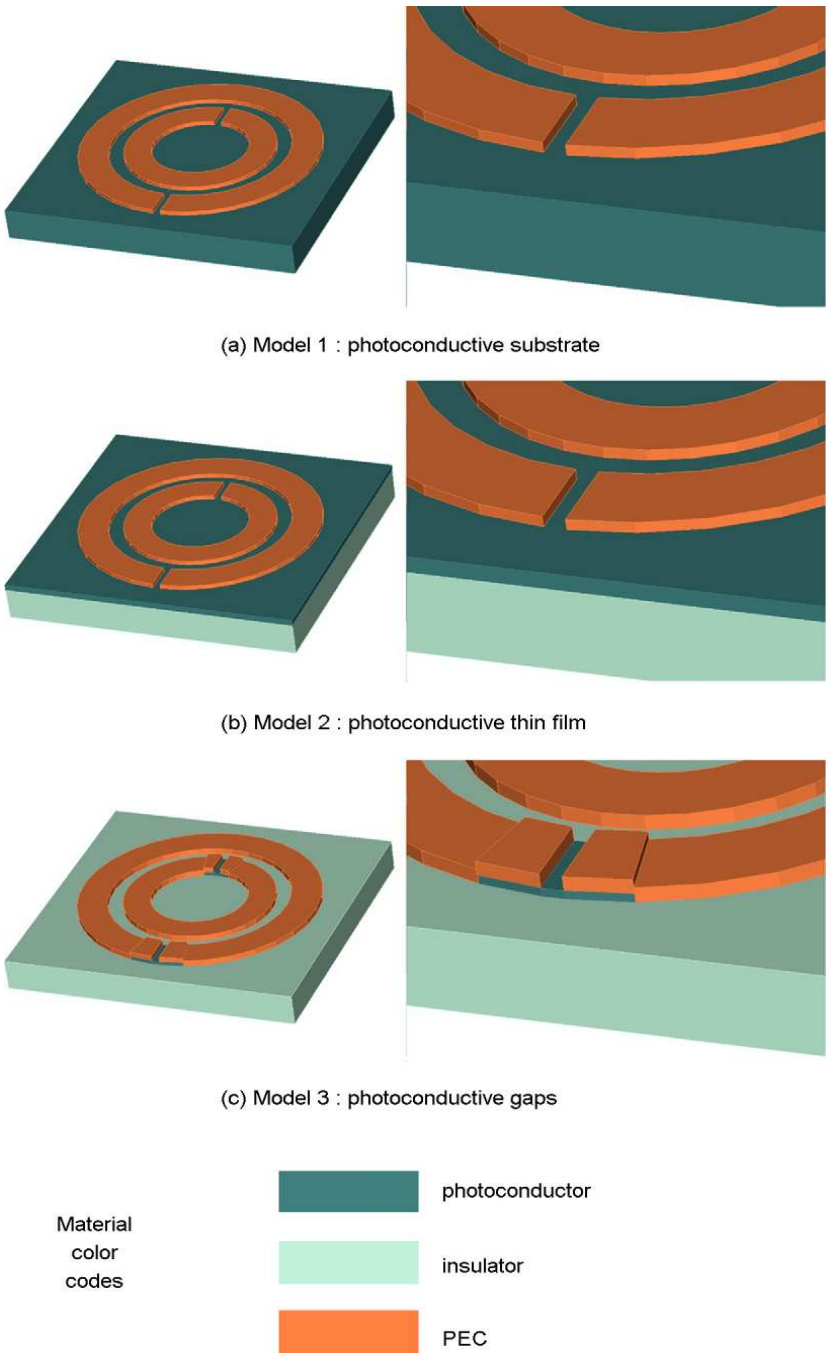

Figure 6.1: Schematic illustration of the three models used in the simulations.

The exact dimensions used in the simulations are listed in Table 6.1. The structure in model 2 and 3 is known to yield a magnetic resonance dip ($\mu < 0$) between 95 and 108 GHz when fabricated on glass substrates ($\varepsilon = 4.82$). For model 1, the structure is rescaled such that the resonance will occur around 90–100 GHz when fabricated on Si substrates ($\varepsilon = 11.9$). In models 2 and 3, the thin photoconductive layer is modeled by a 1 μm thick ZnO ($\varepsilon = 8.5$) film. For all models, the substrate thickness is 150 μm, and the 0.5 μm-thick conductors of the resonators are modeled as perfectly conducting. The schematic SRR unit cell and the relative orientation of the electromagnetic excitation are shown in the inset of Fig. 6.2. The magnetic field is perpendicular to the SRR plane and the directions of electric field and propagation are as shown. For all of the simulations; the number of unit cells employed was chosen as 3 in the propagation direction, while periodic boundary conditions along the other two directions have been used. The calculated transmission spectra for the three SRR models when there is no illumination are shown in Fig. 6.2. A magnetic resonance dip is observed at 88 GHz for model 2, at 90 GHz for model 3, and at 95 GHz for model 1. Although the in-plane geometry of models 2 and 3 are identical, the 2 GHz shift in the resonance frequency is expected due to the presence/absence of the thin photoconductive layer which contributes by a different dielectric constant. The magnetic nature of the resonance dip is verified by closing the SRR gaps by perfect electrical conductor (PEC) in simulations and observing of the disappearance of the dip. For all three models the minimum of the transmission dip is observed around -60 dB.

	Model 1	Model 2	Model 3
Substrate material	Si (ε = 11.9)	Glass (ε = 4.82)	Glass (ε = 4.82)
Substrate thickness	150 μm	150 μm	150 μm
Photoconductive layer	substrate	1 μm-thick ZnO (ε = 8.5)	1 μm-thick ZnO (ε = 8.5) across gaps
Periodicity in SRR plane $a_k = a_E$	164.2 μm	262.7 μm	262.7 μm
PEC thickness	0.5 μm	0.5 μm	0.5 μm
Split ring gap	4.5 μm	7.2 μm	7.2 μm
Inner ring inner radius	26.9 μm	43 μm	43 μm
Inner ring outer radius	42 μm	67.2 μm	67.2 μm
Outer ring inner radius	50.4 μm	80.7 μm	80.7 μm
Outer ring outer radius	67.2 μm	107.5 μm	107.5 μm

Table 6.1. Parameters used in simulations for the three models.

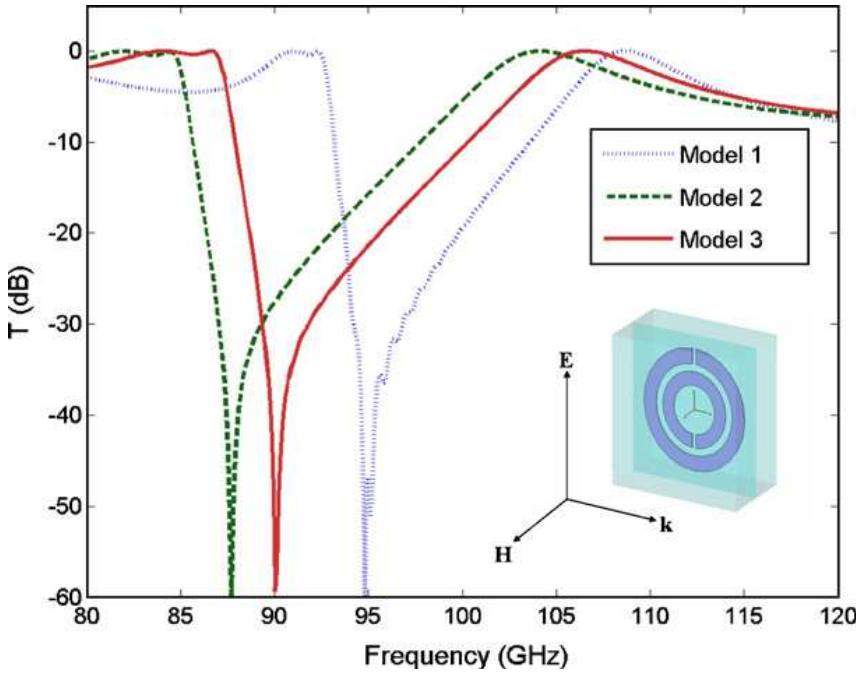

Figure 6.2: Calculated transmission coefficient for the three models shown in fig. 6.1 when no optical excitation is present. The pronounced transmission dips in the spectra are due to the SRRs magnetic resonance. Inset shows the orientation of the E-field, H-field, and wave vector.

Then, the effect of photoexcitation was investigated for the three models by varying the conductivity (σ) of the respective photoconductive layers. Because of the limitations imposed by the simulation toolbox, the conductivity was assumed to be a constant throughout the photoconductive layer. Although this assumption may not model the optical absorption process accurately for some cases, it is a valid approximation for low absorption coefficients and/or thin absorbing films. Fig. 6.3 shows the transmission spectra calculated for model 1 as a function of the substrate conductivity. The two lower σ values (0.1 and 1 S/m) represent the typical conductivity values for commercial Si substrates. It is observed that the transmission dip occurs at -53 dB and -36 dB for $\sigma = 0.1$ S/m and $\sigma = 1$ S/m, respectively. When the conductivity of the substrate is increased gradually (equivalent to a gradual increase of photogeneration throughout the entire substrate), the resonance is observed to disappear gradually. For a sufficiently large

increase in conductivity, the resonance can be completely switched off. For example, an increase from 1 S/m to 30 S/m in σ results in the total disappearance (dotted purple curve) of the resonance. For σ = 30 S/m, the transmission level drops to -15 dB as a result of the increased total loss in the structure.

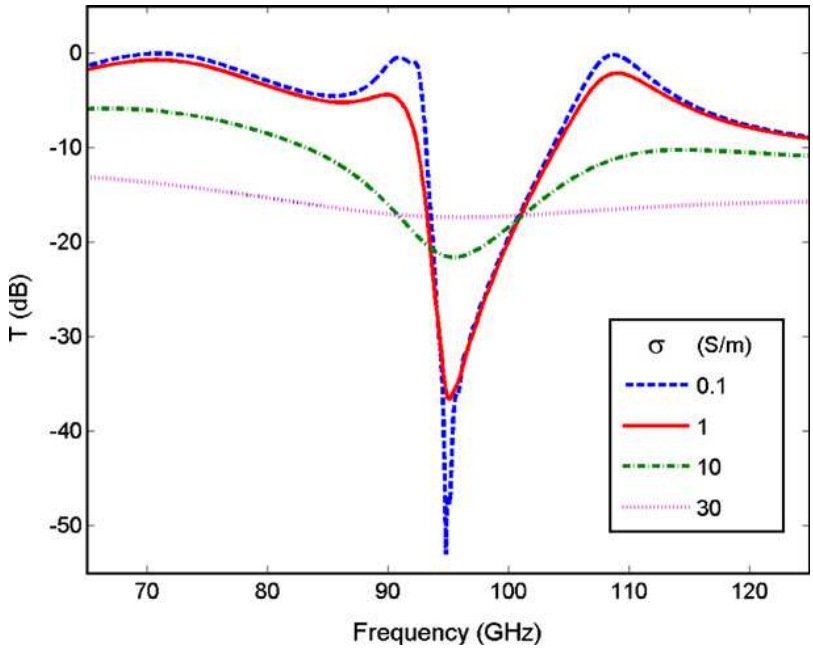

Figure 6.3: Calculated transmission spectra for model 1 of Fig. 6.1 as a function of frequency for various conductivity values of the photoconducting substrate.

Analogous calculations to the one described above were performed also for models 2 and 3, where the effect of a conductivity increase of the thin photoconducting layer was investigated. Fig. 6.4 shows the transmission spectra that were calculated for model 2. The two lower σ values (0.3 S/m and 5 S/m) represent the range of conductivity values when the structure is not illuminated with sufficient optical power. It is observed that the transmission dip approaches -60 dB and -36 dB for s = 0.3 S/m and σ = 5 S/m, respectively. As the conductivity of the thin film photoconductive layer is increased the resonance is observed to disappear gradually. If the photoconductivity is increased as much as 300 S/m (dotted purple line), the resonance dip disappears. Similar to the model 1, the transmission level of the structure drops to -10 dB for this high conductivity value as a result of the loss associated with the thin conducting layer. Fig. 6.5 shows the calculated transmission spectra for model 3. It is observed that the non-illuminated

transmission dip approaches -54 dB and -35 dB for σ = 1 S/m and σ = 10 S/m, respectively. When the conductivity of the photoconductive material across the gaps is increased, the resonance is observed to disappear gradually in similar fashion to the other two models. Finally, a 100-fold increase of conductivity, from the non-illuminated value of 10 S/m (solid red curve) to 1000 S/m (solid purple curve), causes the complete switch off of the resonance. In contrast to the first two models, where the transmission levels away from the magnetic resonance showed a considerable drop by increasing conductivity, here the transmission level remains at around -5 dB even for 1000 S/m conductivity.

Comparing the results of Figs. 6.3–6.5, several observations are made: First, the conductivity value to achieve complete switching is highest for model 3 and lowest for model 1. Similarly, the proportional increase in conductivity required to achieve any fixed amount (in dB) of switching is also highest for model 3 and lowest for model 1. These observations are better displayed in Fig. 6.6, wherein the depth of the respective resonance dips are plotted for the three models as a function of conductivity. It is seen that the resonance depth is highest for model 3 (least switching), and lowest for model 1 (largest switching). This is expected since the volume where the material conductivity is modulated is highest in model 1 and lowest in model 3. However, it has to be noted that model 3 is still the most efficient when required photoconductivity change multiplied by the photo-absorbing volume is considered. This is the proper way of comparison, because the product of the required photoconductivity change and optically absorbing volume is directly proportional to the number of absorbed photons, hence to the required incident power. Fig. 6.7 compares calculated resonance depths for the three models as a function of the product of photoconductivity and optically absorbing volume. It is observed from Fig. 6.7 that model 3 is approximately four and two orders of magnitude more efficient than models 1 and 2, respectively.

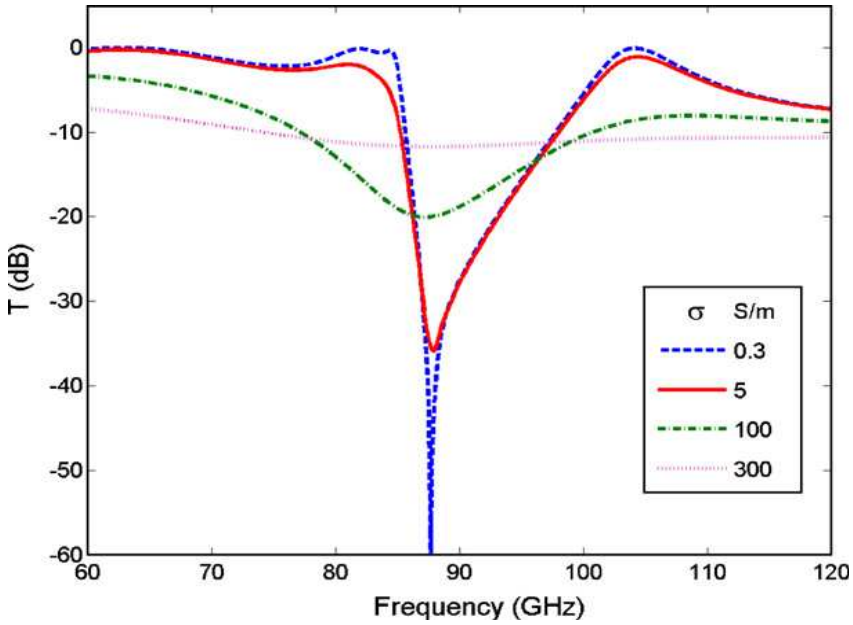

Figure 6.4: Calculated transmission spectra for simulation model 2 of Fig. 6.1 as a function of frequency for various conductivity values of the thin photoconducting film.

After having defined the required designs and conditions to achieve satisfactory switching, the fabrication of those systems and the experimental validation of the results described above are investigated. Here, the fabrication and the non-illumination characterization of the model 1 described above is presented. SRR arrays were fabricated on 450 μm-thick Si substrates with 2 S/m conductivity. First, the model 1 SRR pattern described in Table 1 was defined by photolithography. Then, 100 A° Ti/5000 A° Au metal patterns were deposited by thermal evaporation and subsequent lift-off. Fig. 6.8(a) shows several examples of fabricated samples. The larger samples at the left and bottom of the figure are designed for lower frequency experiments. The stack of planar samples sandwiched between glass spacers is the bulk 100 GHz test sample. A detail of one of the planar samples can be seen in Fig. 6.8(b). The millimeter wave measurements were carried out by using a HP 8510C network analyzer. First, the signal from the network analyzer was converted up in frequency to the 75–115 GHz range by using a multiplier source unit. The signal was transmitted by a horn antenna and the transmission through a stack of samples was measured by a second horn antenna and mixing detector combination. Stacking of approximately 20 samples was necessary in order to cover the entire antenna aperture. Fig. 6.9 shows the measured transmission through 36 consecutive SRRs in the propagation direction. The measurement orientation was same as that is

indicated in Fig. 6.2. A -60 dB resonance dip was observed between 108 GHz and 115 GHz. The spectral shift from simulations is due to deviation from the design during fabrication. The transmission level for non-resonant frequencies was around -20 dB, which is consistent with the increased loss associated with the large number of SRRs in the propagation direction. To test the optical switching, it was necessary to be able to illuminate the sample. However, the stack of samples was too tightly packed and had no optical clearance. We were not able to observe the SRR resonance when the stack was disassembled and a single layer of substrate was tested. This is because a single layer is too thin to cover the antenna aperture. We are currently investigating different stack geometries where we will be able to effectively cover the antenna aperture as well as have enough optical clearance to test switching characteristics.

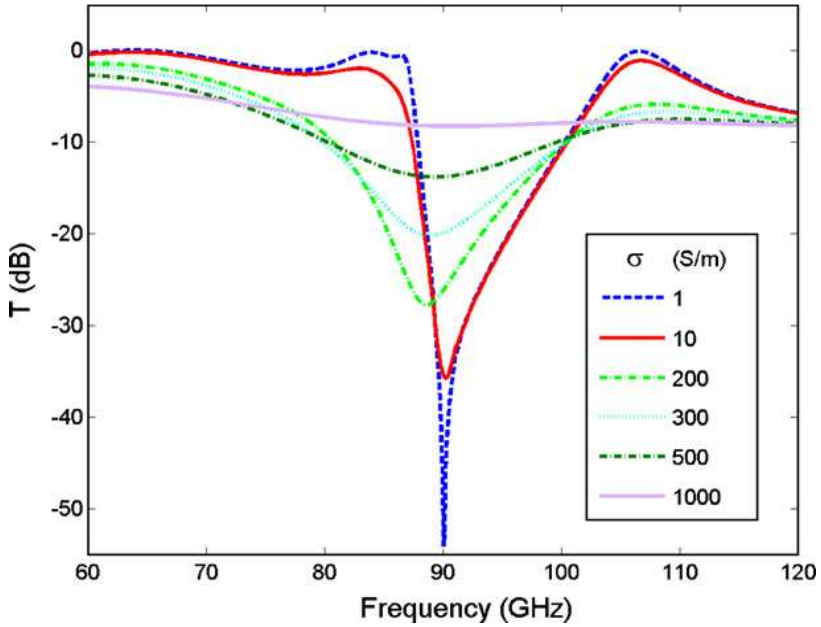

Figure 6.5: Calculated transmission spectra for model 3 of Fig. 6.1 for various values of conductivity of the photoconducting material covering the SRR gaps.

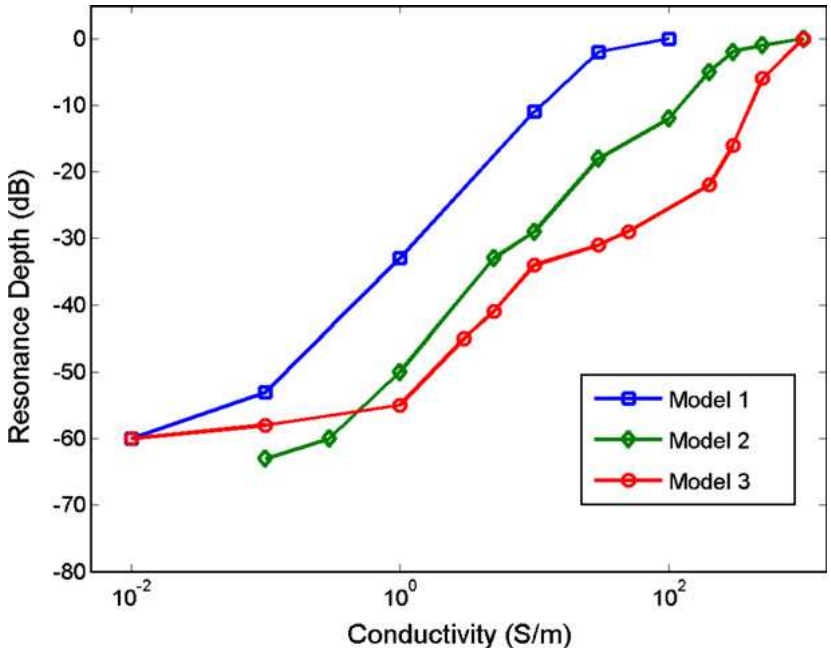

Figure 6.6: Calculated resonance depth (dB) for the three models as a function of conductivity.

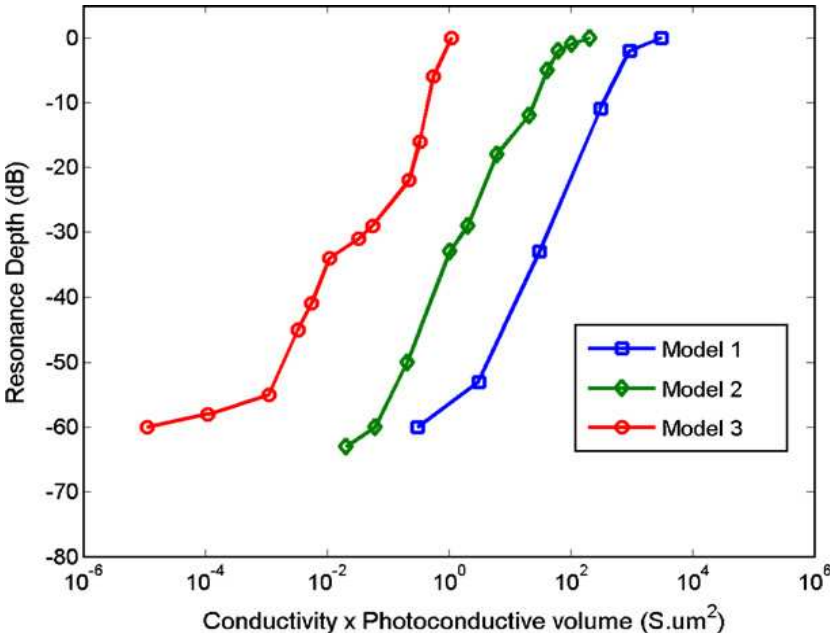

Figure 6.7: Calculated resonance depth (dB) for the three models as a function of the product of optically absorbing volume and photoinduced conductivity (this product is proportional to the absorbed optical power).

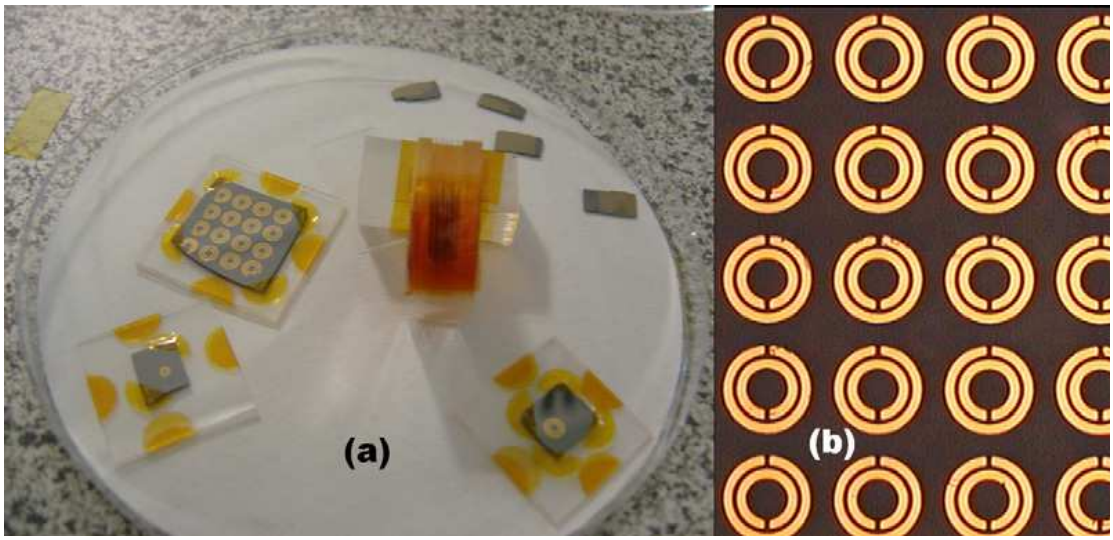

Figure 6.8: Fabricated samples: (a) larger, lower frequency samples, and the stack of planar samples for 100 GHz operation. (b) Photomicrograph of sample.

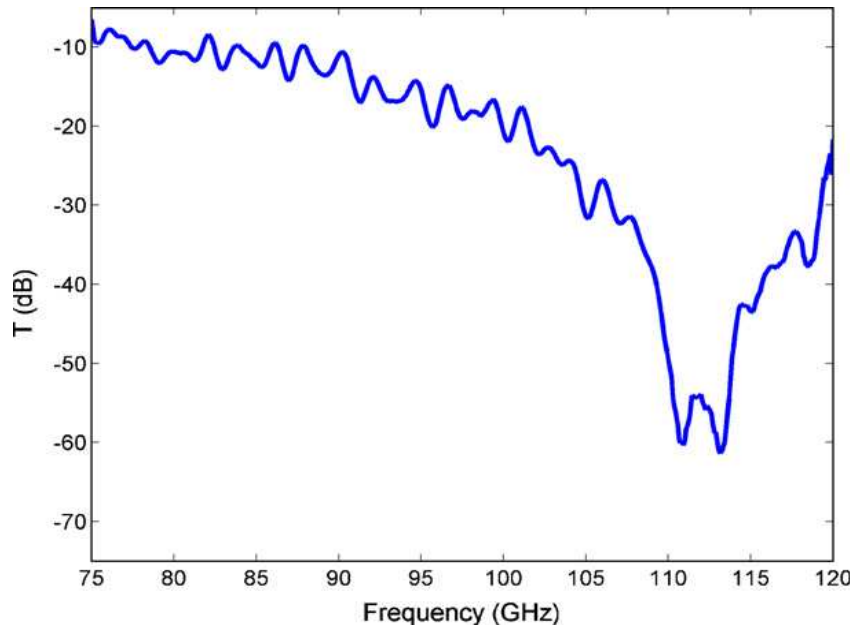

Figure 6.9: Measured transmission spectra of SRRs fabricated on Si substrates according to model 1.

In conclusion, the effect of conductivity variation as a proposed method for the investigation of the photoconductive switching properties of SRRs was simulated. Three different simulation models that are applicable under certain fabrication and/or optical excitation conditions were described. It was calculated that for a large range of dark conductivity values, it is possible to achieve switching by the careful selection of the appropriate model and excitation conditions. SRR structures on Si substrates were fabricated and a -60 dB resonance dip between 108–115 GHz was measured. Next, these structures will be tested under optical excitation.

Chapter 7

Conclusion

The main purpose of this thesis was to develop a better understanding of the physics of metamaterials. During our studies, we focused on the left-handed materials and their applications both in microwave and in THz frequency regimes. Firstly, we investigated the criteria to determine left-handed behaviour in metamaterials while working on structures operating in the GHz frequencies. Later, we investigated the possibility of building metamaterials which operate in the far infrared frequencies. During the course of the study, we used numerical and experimental techniques to characterize metamaterials with negative permittivity, negative permeability and negative index of refraction. The outline of the thesis can be found in Chapter 1.

In Chapter 2 of the thesis, we presented a theoretical background of left-handed materials. The definitions of negative index materials, backward wave propagation, negative refraction at the interface between left-handed and regular media and other basic aspects are described. Artificial building blocks such as the split-ring resonators (SRRs), continuous wires, and slab-pairs and their general response is discussed. Finally, a short historical review of left-handed material research is included.

We discussed the criteria to identify a negative index material in Chapter 3. During this study, we investigated the transmission properties of the SRRs as well as the continuous wires and CMMs consisting of SRRs and wires in the microwave frequency regime. In addition to this, the propagation of EM waves for different orientation of the SRRs has been studied both experimentally and theoretically. We realized that the incident electric field couples to the magnetic resonance of the SRR, provided its direction is such as to break the mirror symmetry of the SRR. This effect (EEMR) has great importance while studying metamaterials operating in higher frequencies since it enables characterization with normal incidence to SRR plane and as little as even a single unit cell in the propagation direction.

In Chapter 4, a detailed parametric study of the SRRs is presented. The dependence of the magnetic and electric resonance frequencies on the SRR's geometrical parameters, shape and configuration for a single-ring SRR in the propagation direction is presented. The effect of background material and SRR orientation relative to incident EM field is studied. It was found that the loss of the dielectric boards greatly affects the LH transmission peak. The CMM configuration with SRRs on one side and wires on the other side of the boards and aligned with SRR gaps was found to be the most robust configuration. Finally, the issue of the electric coupling to the magnetic resonance was investigated and found to be present in all systems that lack symmetry. Some optimum designs, which are highly symmetric and which may constitute components of promising 2D and 3D LH structures were identified.

In Chapter 5, the electromagnetic properties of μm- scale SRR and slab-pair metamaterials were investigated. We managed to fabricate, for what is to our knowledge for the first time, a micrometer-scale metamaterial consisting of five layers of single-ring SRRs which operates around 6 THz. Other than the measurements performed through EEMR effect, we also performed oblique incidence transmission/reflection measurements in order to demonstrate the magnetic response by exciting the SRRs with an external ***H***-field. In addition, multi-gap SRRs were investigated and the elimination of the EEMR effect through mirror symmetry was achieved. Moreover, as it was expected, we observed

that by increasing the number of the gaps in the SRRs the magnetic resonance frequency moves upwards. Besides the SRR and multi-gap SRR structures we fabricated a μm-scale metamaterial composed of slab-pairs and continuous wires and characterized this metamaterial to demonstrate negative refractive index behavior at 2.6-3THz under normal incidence condititons.

Our work on switchable SRRs is presented in Chapter 6. Here, we analyzed numerically the dependence of switching on the relative configuration of photoconductive material and ordinary SRRs. The effect of photoabsorption is simulated through a variation of the conductivity of the photoconductive material. We have found that the configuration where photoconductive material is limited to the immediate proximity of the SRR gaps exhibits the most significant change in resonance. A sample metamaterial was fabricated on photoconductive substrate and the SRR resonance was verified.

Bibliography

1. V. G. Veselago, "The electrodynamics of substances with simultaneously negative values of permittivity and permeability," Sov. Phys. Usp. **10**, 504 (1968).
2. J. B. Pendry, A. J. Holden, D. J. Robbins, and W. J. Stewart, "Low frequency plasmons in thin-wire structures," Journal of Physics-Condensed Matter **10**, 4785-4809 (1998).
3. J. B. Pendry, A. J. Holden, D. J. Robbins, and W. J. Stewart, "Magnetism from conductors and enhanced nonlinear phenomena," Ieee Transactions on Microwave Theory and Techniques **47**, 2075-2084 (1999).
4. J. B. Pendry, A. J. Holden, W. J. Stewart, and I. Youngs, "Extremely low frequency plasmons in metallic mesostructures," Physical Review Letters **76**, 4773-4776 (1996).
5. D. R. Smith, D. C. Vier, W. Padilla, S. C. Nemat-Nasser, and S. Schultz, "Loop-wire medium for investigating plasmons at microwave frequencies," Applied Physics Letters **75**, 1425-1427 (1999).
6. R. A. Shelby, D. R. Smith, S. C. Nemat-Nasser, and S. Schultz, "Microwave transmission through a two-dimensional, isotropic, left-handed metamaterial," Applied Physics Letters **78**, 489-491 (2001).
7. D. R. Smith, W. J. Padilla, D. C. Vier, S. C. Nemat-Nasser, and S. Schultz, "Composite medium with simultaneously negative permeability and permittivity," Physical Review Letters **84**, 4184-4187 (2000).
8. S. Foteinopoulou, E. N. Economou, and C. M. Soukoulis, "Refraction in media with a negative refractive index," Physical Review Letters **90**, - (2003).
9. N. Garcia, and M. Nieto-Vesperinas, "Is there an experimental verification of a negative index of refraction yet?," Optics Letters **27**, 885-887 (2002).
10. N. Garcia, and M. Nieto-Vesperinas, "Left-handed materials do not make a perfect lens," Physical Review Letters **88**, - (2002).
11. A. A. Houck, J. B. Brock, and I. L. Chuang, "Experimental observations of a left-handed material that obeys Snell's law," Physical Review Letters **90**, - (2003).
12. C. G. Parazzoli, R. B. Greegor, K. Li, B. E. C. Koltenbah, and M. Tanielian, "Experimental verification and simulation of negative index of refraction using Snell's law," Physical Review Letters **90**, - (2003).
13. R. A. Shelby, D. R. Smith, and S. Schultz, "Experimental verification of a negative index of refraction," Science **292**, 77-79 (2001).
14. D. R. Smith, and N. Kroll, "Negative refractive index in left-handed materials," Physical Review Letters **85**, 2933-2936 (2000).
15. P. M. Valanju, R. M. Walser, and A. P. Valanju, "Wave refraction in negative-index media: Always positive and very inhomogeneous," Physical Review Letters **88**, - (2002).
16. G. Dolling, C. Enkrich, M. Wegener, C. M. Soukoulis, and S. Linden, "Low-loss negative-index metamaterial at telecommunication wavelengths," Optics Letters **31**, 1800-1802 (2006).

17. G. Dolling, C. Enkrich, M. Wegener, J. F. Zhou, and C. M. Soukoulis, "Cut-wire pairs and plate pairs as magnetic atoms for optical metamaterials," Optics Letters **30**, 3198-3200 (2005).
18. G. Dolling, M. Wegener, C. M. Soukoulis, and S. Linden, "Negative-index metamaterial at 780 nm wavelength," Optics Letters **32**, 53-55 (2007).
19. C. Enkrich, M. Wegener, S. Linden, S. Burger, L. Zschiedrich, F. Schmidt, J. F. Zhou, T. Koschny, and C. M. Soukoulis, "Magnetic metamaterials at telecommunication and visible frequencies," Physical Review Letters **95**, - (2005).
20. M. Gokkavas, K. Guven, I. Bulu, K. Aydin, R. S. Penciu, M. Kafesaki, C. M. Soukoulis, and E. Ozbay, "Experimental demonstration of a left-handed metamaterial operating at 100 GHz," Physical Review B **73**, - (2006).
21. T. F. Gundogdu, I. Tsiapa, A. Kostopoulos, G. Konstantinidis, N. Katsarakis, R. S. Penciu, M. Kafesaki, E. N. Economou, T. Koschny, and C. M. Soukoulis, "Experimental demonstration of negative magnetic permeability in the far-infrared frequency regime," Applied Physics Letters **89**, - (2006).
22. N. Katsarakis, G. Konstantinidis, A. Kostopoulos, R. S. Penciu, T. F. Gundogdu, M. Kafesaki, E. N. Economou, T. Koschny, and C. M. Soukoulis, "Magnetic response of split-ring resonators in the far-infrared frequency regime," Optics Letters **30**, 1348-1350 (2005).
23. M. W. Klein, C. Enkrich, M. Wegener, C. M. Soukoulis, and S. Linden, "Single-slit split-ring resonators at optical frequencies: limits of size scaling," Optics Letters **31**, 1259-1261 (2006).
24. S. Linden, C. Enkrich, M. Wegener, J. F. Zhou, T. Koschny, and C. M. Soukoulis, "Magnetic response of metamaterials at 100 terahertz," Science **306**, 1351-1353 (2004).
25. W. J. Padilla, A. J. Taylor, C. Highstrete, M. Lee, and R. D. Averitt, "Dynamical electric and magnetic metamaterial response at terahertz frequencies," Physical Review Letters **96**, - (2006).
26. J. D. Jackson, *Classical Electrodynamics* (John Wiley, NY, 1999).
27. C. Kittel, *Introduction to Solid State Physics* (John Wiley New York, 1996).
28. N. Katsarakis, T. Koschny, M. Kafesaki, E. N. Economou, and C. M. Soukoulis, "Electric coupling to the magnetic resonance of split ring resonators," Applied Physics Letters **84**, 2943-2945 (2004).
29. T. J. Yen, W. J. Padilla, N. Fang, D. C. Vier, D. R. Smith, J. B. Pendry, D. N. Basov, and X. Zhang, "Terahertz magnetic response from artificial materials," Science **303**, 1494-1496 (2004).
30. K. Aydin, K. Guven, M. Kafesaki, L. Zhang, C. M. Soukoulis, and E. Ozbay, "Experimental observation of true left-handed transmission peaks in metamaterials," Optics Letters **29**, 2623-2625 (2004).
31. M. Bayindir, K. Aydin, E. Ozbay, P. Markos, and C. M. Soukoulis, "Transmission properties of composite metamaterials in free space," Applied Physics Letters **81**, 120-122 (2002).
32. H. S. Chen, L. X. Ran, J. T. Huangfu, X. M. Zhang, K. S. Chen, T. M. Grzegorczyk, and J. A. Kong, "T-junction waveguide experiment to characterize left-handed properties of metamaterials," Journal of Applied Physics **94**, 3712-3716 (2003).
33. R. B. Greegor, C. G. Parazzoli, K. Li, B. E. C. Koltenbah, and M. Tanielian, "Experimental determination and numerical simulation of the properties of negative index of refraction materials," Optics Express **11**, 688-695 (2003).

34. J. T. Huangfu, L. X. Ran, H. S. Chen, X. M. Zhang, K. S. Chen, T. M. Grzegorczyk, and J. A. Kong, "Experimental confirmation of negative refractive index of a metamaterial composed of Omega-like metallic patterns," Applied Physics Letters **84**, 1537-1539 (2004).
35. K. Li, S. J. McLean, R. B. Greegor, C. G. Parazzoli, and M. H. Tanielian, "Free-space focused-beam characterization of left-handed materials," Applied Physics Letters **82**, 2535-2537 (2003).
36. R. Marques, J. Martel, F. Mesa, and F. Medina, "A new 2D isotropic left-handed metamaterial design: Theory and experiment," Microwave and Optical Technology Letters **35**, 405-408 (2002).
37. L. Ran, J. Huangfu, H. Chen, Y. Li, X. Zhang, K. Chen, and J. A. Kong, "Microwave solid-state left-handed material with a broad bandwidth and an ultralow loss," Physical Review B **70**, - (2004).
38. A. F. Starr, P. M. Rye, D. R. Smith, and S. Nemat-Nasser, "Fabrication and characterization of a negative-refractive-index composite metamaterial," Physical Review B **70**, - (2004).
39. K. Aydin, K. Guven, C. M. Soukoulis, and E. Ozbay, "Observation of negative refraction and negative phase velocity in left-handed metamaterials," Appl Phys Lett **86**, - (2005).
40. J. B. Pendry, and D. R. Smith, "Reversing light with negative refraction," Physics Today **57**, 37-43 (2004).
41. C. A. Balanis, "Advance Engineering Electromagnetics," (John Wiley & Sons, 1989).
42. E. M. L. L.D. Landau, and L.P. Pitaevskii, *Electrodynamics of Continuous Media* (Linacre House Jordan Hill, Oxford, UK: Butterworth Heinemann, 1984).
43. T. F. Gundogdu, N. Katsarakis, M. Kafesaki, R. S. Penciu, G. Konstantinidis, A. Kostopoulos, E. N. Economou, and C. M. Soukoulis, "Negative index short-slab pair and continuous wires metamaterials in the far infrared regime," Optics Express **16**, 9173-9180 (2008).
44. K. Guven, A. O. Cakmak, M. D. Caliskan, T. F. Gundogdu, M. Kafesaki, C. M. Soukoulis, and E. Ozbay, "Bilayer metamaterial: analysis of left-handed transmission and retrieval of effective medium parameters," Journal of Optics a-Pure and Applied Optics **9**, S361-S365 (2007).
45. V. M. Shalaev, W. S. Cai, U. K. Chettiar, H. K. Yuan, A. K. Sarychev, V. P. Drachev, and A. V. Kildishev, "Negative index of refraction in optical metamaterials," Optics Letters **30**, 3356-3358 (2005).
46. J. F. Zhou, E. N. Economou, T. Koschny, and C. M. Soukoulis, "Unifying approach to left-handed material design," Optics Letters **31**, 3620-3622 (2006).
47. J. F. Zhou, L. Zhang, G. Tuttle, T. Koschny, and C. M. Soukoulis, "Negative index materials using simple short wire pairs," Physical Review B **73**, - (2006).
48. K. Guven, M. D. Caliskan, and E. Ozbay, "Experimental observation of left-handed transmission in a bilayer metamaterial under normal-to-plane propagation," Optics Express **14**, 8685-8693 (2006).
49. D. R. Smith, S. Schultz, P. Markos, and C. M. Soukoulis, "Determination of effective permittivity and permeability of metamaterials from reflection and transmission coefficients," Physical Review B **65**, - (2002).

50. N. Katsarakis, T. Koschny, M. Kafesaki, E. N. Economou, E. Ozbay, and C. M. Soukoulis, "Left- and right-handed transmission peaks near the magnetic resonance frequency in composite metamaterials," Physical Review B **70**, - (2004).
51. T. Koschny, M. Kafesaki, E. N. Economou, and C. M. Soukoulis, "Effective medium theory of left-handed materials," Physical Review Letters **93**, - (2004).
52. X. D. Chen, T. M. Grzegorczyk, B. I. Wu, J. Pacheco, and J. A. Kong, "Robust method to retrieve the constitutive effective parameters of metamaterials," Physical Review E **70**, - (2004).
53. T. Koschny, P. Markos, D. R. Smith, and C. M. Soukoulis, "Resonant and antiresonant frequency dependence of the effective parameters of metamaterials," Physical Review E **68**, - (2003).
54. P. Markos, and C. M. Soukoulis, "Transmission properties and effective electromagnetic parameters of double negative metamaterials," Optics Express **11**, 649-661 (2003).
55. S. O'Brien, and J. B. Pendry, "Magnetic activity at infrared frequencies in structured metallic photonic crystals," Journal of Physics-Condensed Matter **14**, 6383-6394 (2002).
56. T. Koschny, P. Markos, E. N. Economou, D. R. Smith, D. C. Vier, and C. M. Soukoulis, "Impact of inherent periodic structure on effective medium description of left-handed and related metamaterials," Physical Review B **71**, - (2005).
57. D. R. Smith, D. C. Vier, T. Koschny, and C. M. Soukoulis, "Electromagnetic parameter retrieval from inhomogeneous metamaterials," Physical Review E **71**, - (2005).
58. X. Chen, B. I. Wu, J. A. Kong, and T. M. Grzegorczyk, "Retrieval of the effective constitutive parameters of bianisotropic metamaterials," Physical Review E **71**, - (2005).
59. R. Marques, F. Medina, and R. Rafii-El-Idrissi, "Role of bianisotropy in negative permeability and left-handed metamaterials," Physical Review B **65**, - (2002).
60. G. Dolling, C. Enkrich, M. Wegener, C. M. Soukoulis, and S. Linden, "Simultaneous negative phase and group velocity of light in a metamaterial," Science **312**, 892-894 (2006).
61. S. Zhang, W. J. Fan, N. C. Panoiu, K. J. Malloy, R. M. Osgood, and S. R. J. Brueck, "Experimental demonstration of near-infrared negative-index metamaterials," Physical Review Letters **95**, - (2005).
62. C. M. Soukoulis, J. F. Zhou, T. Koschny, M. Kafesaki, and E. N. Economou, "The science of negative index materials," Journal of Physics-Condensed Matter **20**, - (2008).
63. U. K. Chettiar, A. V. Kildishev, H. K. Yuan, W. S. Cai, S. M. Xiao, V. P. Drachev, and V. M. Shalaev, "Dual-band negative index metamaterial: double negative at 813nm and single negative at 772nm," Optics Letters **32**, 1671-1673 (2007).
64. J. B. Pendry, "Negative refraction makes a perfect lens," Physical Review Letters **85**, 3966-3969 (2000).
65. J. B. Pendry, and D. R. Smith, "The quest for the superlens," Scientific American **295**, 60-67 (2006).
66. T. Weiland, R. Schuhmann, R. B. Greegor, C. G. Parazzoli, A. M. Vetter, D. R. Smith, D. C. Vier, and S. Schultz, "Ab initio numerical simulation of left-handed metamaterials: Comparison of calculations and experiments," Journal of Applied Physics **90**, 5419-5424 (2001).

67. J. Pacheco, T. M. Grzegorczyk, B. I. Wu, Y. Zhang, and J. A. Kong, "Power propagation in homogeneous isotropic frequency-dispersive left-handed media," Physical Review Letters **89**, - (2002).
68. P. Markos, and C. M. Soukoulis, "Absorption losses in periodic arrays of thin metallic wires," Optics Letters **28**, 846-848 (2003).
69. P. Markos, and C. M. Soukoulis, "Numerical studies of left-handed materials and arrays of split ring resonators," Physical Review E **65**, - (2002).
70. P. Markos, I. Rousochatzakis, and C. M. Soukoulis, "Transmission losses in left-handed materials," Physical Review E **66**, - (2002).
71. R. W. Ziolkowski, "Pulsed and CW Gaussian beam interactions with double negative metamaterial slabs," Optics Express **11**, 662-681 (2003).
72. P. Gay-Balmaz, and O. J. F. Martin, "Electromagnetic resonances in individual and coupled split-ring resonators," Journal of Applied Physics **92**, 2929-2936 (2002).
73. H. O. Moser, B. D. F. Casse, O. Wilhelmi, and B. T. Saw, "Terahertz response of a microfabricated rod-split-ring-resonator electromagnetic metamaterial," Physical Review Letters **94**, - (2005).
74. S. O'Brien, D. McPeake, S. A. Ramakrishna, and J. B. Pendry, "Near-infrared photonic band gaps and nonlinear effects in negative magnetic metamaterials," Physical Review B **69**, - (2004).
75. J. F. Zhou, T. Koschny, L. Zhang, G. Tuttle, and C. M. Soukoulis, "Experimental demonstration of negative index of refraction," Applied Physics Letters **88**, - (2006).
76. R. S. Penciu, M. Kafesaki, T. F. Gundogdu, E. N. Economou, and C. M. Soukoulis, "Theoretical study of left-handed behavior of composite metamaterials," Photonics and Nanostructures-Fundamentals and Applications **4**, 12-16 (2006).